ONE-DIMENSIONAL SIMULATION METHODS FOR DISTRIBUTED FEEDBACK SEMICONDUCTOR LASERS

ONE-DIMENSIONAL SIMULATION METHODS FOR DISTRIBUTED FEEDBACK SEMICONDUCTOR LASERS

By

YANPING XI, B.ENG., M.Sc.

A Thesis

Submitted to the School of Graduate Studies

in Partial Fulfilment of the Requirements

for the Degree

Doctor of Philosophy

McMaster University

DOCTOR OF PHILOSOPHY (2009) McMaster University

(Electrical and Computer Engineering) Hamilton, Ontario

TITLE: One-Dimensional Simulation Methods for Distributed Feedback Semiconductor Lasers

AUTHOR: Yanping Xi

B.ENG., M.Sc. (Nanjing University of Sci. & Tech., China)

SUPERVISOR: Dr. Wei-Ping Huang

Professor, Department of Electrical and Computer Engineering

NUMBER OF PAGES: xiii, 162

Abstract

The semiconductor distributed feedback (DFB) laser is mainly characterised by the single-longitudinal-mode operation with a narrow spectral linewidth, which leads to its wide application in fiber-optic communication systems. Several numerical models ranging from physics-based to phenomenological ones have been developed with different level of complexities and for different applications. However, with the continuous improvement in designs of DFB lasers, more efficient simulation methods with sufficient accuracy are highly desirable. In this thesis, I mainly focus on developing new one-dimensional (1D) simulation methods of DFB lasers with improved computational efficiency and physical insight without compromise on accuracy. Further, a new design idea for DFB lasers are explored and investigated by using the simulation techniques developed.

Starting with the well-known 1D time-dependent coupled-wave equations, we have examined two different solution schemes, i.e. the traveling wave model (TWM) and the standing wave model (SWM). The TWM has the merits of straightforward implementation, and being able to simulate a large variety of the structure even if the laser cavity has a small quality factor (Q-factor). Firstly, the existing time-domain solution schemes are reviewed and compared under a unified framework. A high-order split-step traveling wave method is then developed. Its validity and efficiency are examined through the comparison made with the conventional split-step scheme.

For laser structures with large variations of the carrier/photon density, however, the TWM is not computationally economical. The SWM on the other hand has its advantages in dealing with the laser cavity with a relatively large Q-factor. Two different standing wave models are proposed to simulate the index-coupled and gain-coupled DFB lasers, respectively. The complexities of these two numerical models are further reduced through an approximation made on the time-dependent carrier distribution. Finally, the proposed SWMs are reduced to a similar form to the rate equation formulations for establishing the linkage between the 1D model and the rate equation model. More physical insights into the conventional and powerful rate equations will be gained through this linkage.

The final part of the thesis focus on the analysis of a novel design of single-mode operation DFB laser employing the dispersive grating. The design idea is verified by the proposed SWM.

Acknowledgements

I would like to acknowledge a great many people who has been supporting me during this period of my life, both directly and indirectly.

First of all, I would like to thank my supervisor Dr. Wei-Ping Huang for his great vision, for sharing his knowledge and valuable experiences with me, for his continuous guidance and support for all respects in my life during the course of my Ph. D. program.

I would like to thank my committee members. Dr. Xun Li was always available to attend to my questions and provide valuable advices from laser physics to modeling techniques during our numerous discussions. Dr. Shiva Kumar and Dr. Chang-Qing Xu span a wide knowledge base from fiber-optic communication systems to optoelectronics.

I am also very grateful to Dr. Wei Li, Dr. Seyed M. Sadeghi, Dr. Chenglin Xu, and Dr. Ningning Feng for their helpful discussions. Dr. Li Yang was always in my cheer-leading team and much more. All of my co-workers and friends in the CRL and ECE department are thankfully acknowledged. They were my most valuable resource at McMaster and it has been my pleasure working with them in the past couples of years.

I acknowledge the ECE administrative and technical support, Ms. Cheryl Gies, Ms. Helen Jachna, Mr. Terry Greenlay and Mr. Cosmin Coroiu.

I would like to give my special thanks to my husband Hao Wang, for his love and great emotional support when things were smooth and when they were rough. Last but not least, I would like to thank my parents for their love and encouragement throughout the years.

Contents

List of Figures

List of Tables

Chapter 1

Introduction

1.1 Motivations

DFB lasers are one of key photonic devices widely used in fiber-optic communication systems as optical sources with direct or external modulations. Many numerical models for simulating DFB lasers have been developed, ranging from fully physics-based to phenomenological ones, also known as behavior models.

The fully physics-based models [1]-[4] are the most comprehensive models which are able to describe at the microscopic level the details of the physical mechanisms and processes underlying the operation of the laser diodes, such as the different recombinations in the gain media, the carrier transport, the optical confinement and resonance, and the heat generation and diffusion, etc. Such models, though comprehensive and accurate, are normally complicated to formulate mathematically and time-consuming to solve numerically. For sub-system and system applications, some of the details inherent in the physics-based models are not necessary and may be parameterized. For this reason, simplification can be made by proper approximations so that the behavior models can be established and utilized. The behavior models [5]-[9] treat the device as a black box characterized by a set of governing equations and model parameters. The main physical processes such as optical gain, carrier dynamics, optical resonance as well as thermal effects can all be described at the behavior levels in a simplified yet insightful fashion. Aside from its simplicity relative to the physics-based model, significant improvement in computation efficiency allows the behavior model to be widely applied to the system simulation.

In practice, device designers often need to obtain the basic knowledge of the performance of new designs through trial and error. Once a new design is validated, it is then required to be optimized for a specific application purpose. Meanwhile, from system designers' point of view, more accurate simulation tools are still desired in system simulation to reduce development costs and time. All of these call for simulation tools that can provide the satisfying accuracy, but also hold the computational effort at a feasible level. The effective 1D model [10]-[14] is a candidate for this purpose. It accounts for the longitudinal variations of the optical field, carrier, etc. Effective parameters are introduced to include the transverse effects such as transverse optical effects and carrier transport effects [15]-[17]. Within this context, the main objective of this thesis is to develop efficient 1D simulation tools of the DFB laser with the satisfying accuracy from the perspective of both device designers and system designers.

The single-longitudinal-mode operation of the DFB laser is of great importance in fiber-optic communication systems due to its merits in reducing effects of fiber group-velocity dispersion [18] and hence allowing longer reach at higher bit rates in comparison with otherwise multimode Fabry Perot lasers. The uniform-grating index-coupled DFB lasers with AR coated facets have the intrinsic drawback of the two degenerate modes spectrally symmetric with respect to the Bragg frequency [19]. Existing solutions include the introduction of a quarter-wave-shifted ($\lambda/4$-shifted) grating [20] or gain (or loss)-coupled grating [19], [21]. The other objective of this thesis is to examine the alternative design concept of the single-longitudinal-mode DFB laser by using the proposed modeling techniques.

1.2 Background of the Research

Although the lasing action in semiconductor was reported as early as 1962 [22]-[25], the conversion from the laboratory curiosity to practical applications takes place in 1970 when the semiconductor lasers operating continuously at room temperature was demonstrated [26],[27] and the double-heterostructure semiconductor lasers were also introduced at that time to reduce greatly the threshold current density [26], [28]. Since then, the design and development of the semiconductor lasers are proven to be fascinating work, which make the semiconductor lasers become widely used in a variety of applications. One of them is the fiber-optic communications where the semiconductor laser becomes one of key components due to their inherent advantages such as compact size, high efficiency, narrow spectral width of emitted light, and possibility of direct modulation.

The basic understanding of the physics behind a laser is illustrated in Figure 1.1, which shows two key elements to operate a laser: 1) an active material which has the optical gain, i.e. can amplify the electromagnetic radiation inside it and 2) an optical resonator which feeds back light through its reflector. In semiconductor lasers, the semiconductor material acts as the gain medium to generate the spontaneous emission and amplify a fraction of it by the stimulated emission. The optical feedback can be realized by a variety of structures, such as Fabry-Perot cavities, ring cavities, distributed feedback (DFB) and distributed Bragg reflector (DBR) cavities, etc.

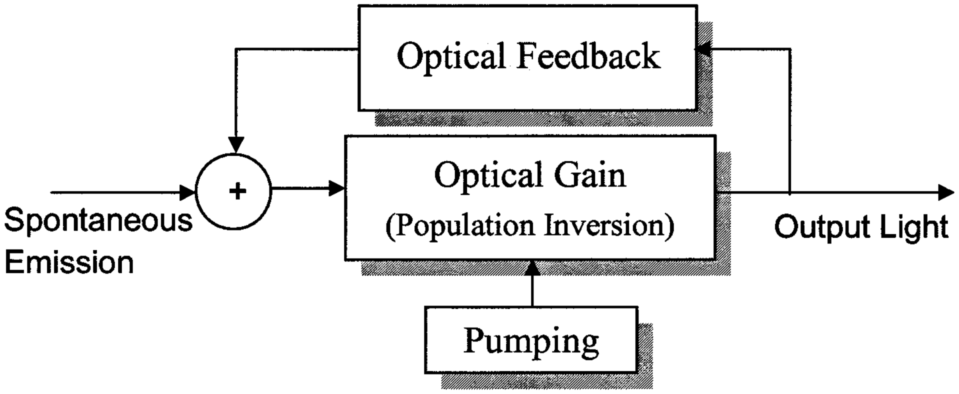

Figure 1.1 Operation principle of a laser

To fully capture the physical processes of a semiconductor laser, the model needs to be able to describe the wave propagation along the optical waveguide, the optical properties of the media in the device, the carrier transport in the device, and the thermal properties of the materials. Due to these complex device physics, predictive modeling with accurate and efficient tools is highly desired for new or optimized device designs. An appropriate tool will help reduce development costs and time greatly for the given design requirement. Many models with different levels of complexity and assumptions have appeared. They may be classified into the following three categories:

Fully physics-based model: It is the most comprehensive numerical model considering both the transverse and longitudinal effects; as such they are three-dimensional (3D) models [1]-[4]. The wave propagation, optical properties of the media, carrier transport and thermal diffusions can all be captured such that the physical processes inside the laser cavity as well as the device performance can be fully described and predicted. These models although rigorous, involve very sophisticated modeling techniques, consequently are extremely time-consuming.

Behavior model: This model is denoted as zero-dimensional (0D) model in this thesis and consists of conventional rate equation description of the carrier-photon interaction. It can produce simple, yet insightful analytical expressions for almost all laser characteristics [5]-[9]. However the spatial variance of the carrier and optical fields are all neglected in this model. Moreover, the input parameters of this model, such as those effective coefficients and phenomenologically induced parameters, have to be extracted from the detailed physics-based model or the experimental results [29], [30], and consequently are normally only valid for the given device.

Effective model: Certain assumptions are made to the fully physics-based model under specific simulation requirement, resulting in various effective models. For example, the models in [31]-[33] take account of the transverse optical field, carrier transport effects and thermal diffusion over the transverse cross-section. These models were developed primarily for FP lasers and therefore do not take the longitudinal effects into account if applied to DFB lasers; whereas, in [34]-[37], those effects mentioned above are accounted for along one dimension of the transverse cross-section, normally in the direction perpendicular to the junction, as well as along the longitudinal dimension. As a result, the former are two-dimensional (2D) models in the sense of XY dimension and the latter are 2D in XZ (or YZ) dimension. Shown in Figure 1.2 is a schematic illustration of the orientation of a semiconductor laser. With further simplifications, the variation of the optical field, the carrier, and the temperature are only accounted for along the longitudinal axis in [10]-[14]. In these 1D models, effective parameters, such as the confinement factor, is introduced to account for the transverse optical effects. The carrier transport in transverse directions can also be included in an approximate manner into a 1D longitudinal laser simulation [15]-[17]. The complexity of effective models is in between fully physics-based ones and behavior ones.

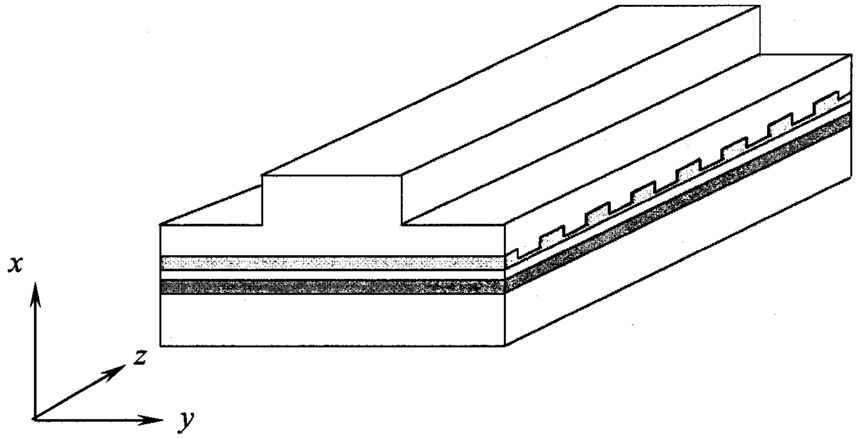

Figure 1.2 Schematic illustration of the orientation of a semiconductor laser

Generally speaking, the comprehensive yet time-consuming fully physics-based model is more often to be adopted for the development of the device design. The detailed physical picture of the device can be fully described to facilitate the accurate prediction of the device performance for given materials and structures under specified operating conditions. On the other hand, the simplicity of behavior model makes it being widely used in the system simulation.

In practice, it is important to have a simulation tool with high efficiency and yet being able to capture the most important physical insights under certain application. In this thesis, we will focus on the 1D model due to its advantage of being a good balance between two seemingly contradictory requirements: accuracy and simplicity. This model takes account of structure details of the DFB laser, such as spatial dependent coupling coefficient, phase shifts and facet conditions. Moreover, important effects, such as the spectral and spatial-hole burnings, are all included. As such, it is accurate enough to describe all the interesting characteristics of the DFB laser. Moreover, the accuracy of the 1D model can be further improved by incorporating secondary physical effects that may play an important role whenever necessary for a specific device, like what has been done in [15]-[17].

1.3 Overview of the Thesis and Contributions of the Research

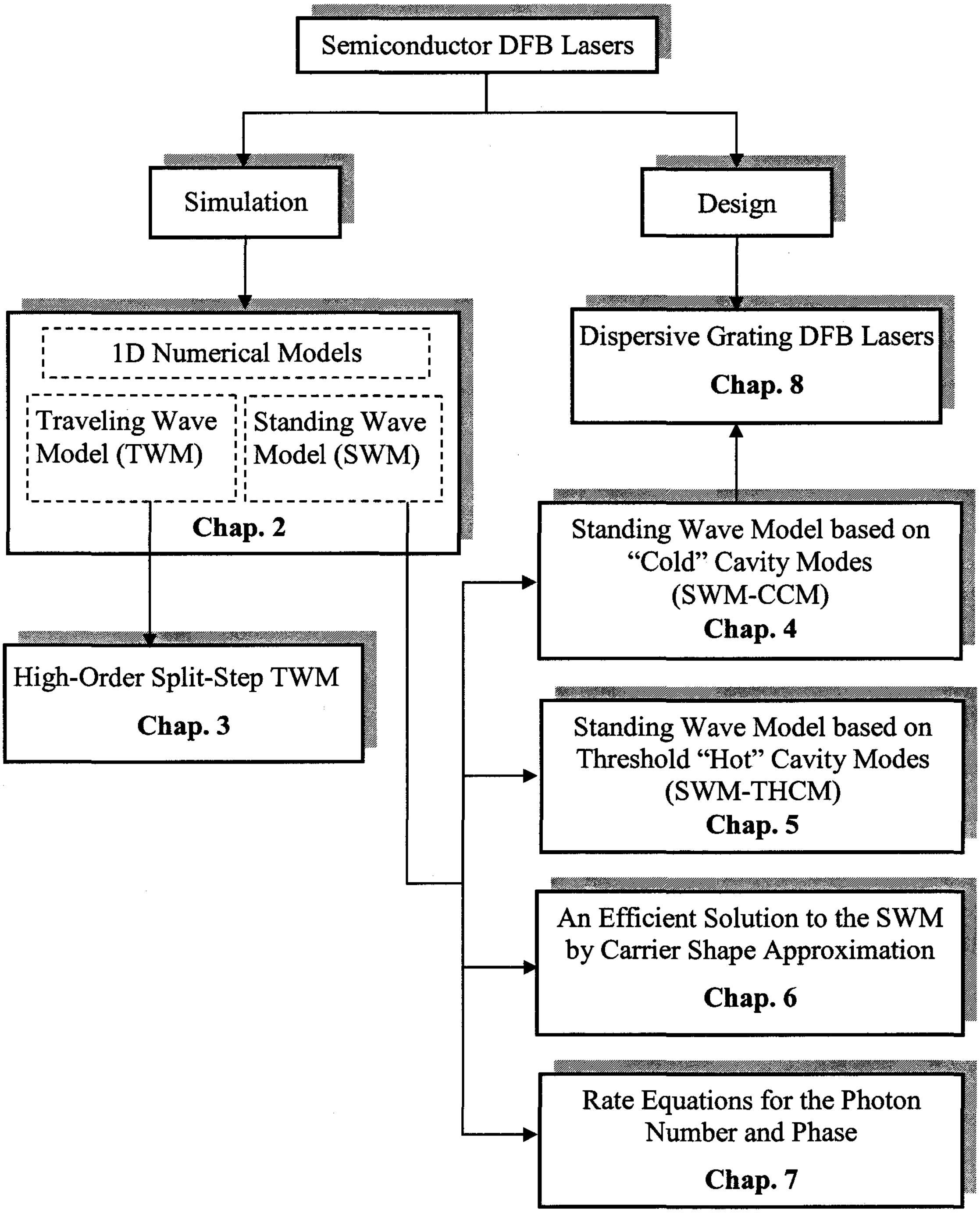

Figure 1.3 Block diagram of the thesis structure

This thesis contains nine chapters in total. The relations between these chapters are presented in the block diagram shown in Figure 1.3, where the first chapter of introductions and last chapter of conclusions are not included. The major contributions of this thesis are corresponding to the research work from chapter 3 to chapter 8. They are presented accordingly as follows.

Chapter 1 starts with the introduction to existing models with different level of complexities for simulating semiconductor lasers. The reason that we choose 1D models as the starting point is also clarified with the emphasis on DFB lasers in the context of circuit or system applications. It is followed by the overview of this thesis where major contributions of the research work are presented.

For 1D numerical modeling of DFB lasers, there mainly exist two types of models: the TWM and the SWM. Their differences and respective limitations are clarified in chapter 2. The TWM is then introduced in detail. Basically it tracks the contra-directional propagating fields along the optical laser cavity explicitly by solving the partial differential equations (PDEs) of time and space. The existing solution schemes are reviewed under a unified framework, among which the split-step scheme shows a superior performance, and therefore is implemented and validated. This scheme will be served as one of benchmarks of the later model development. The detailed description of the standing wave method is left until chapter 4.

Chapter 3 focuses on an improvement of the conventional split-step time-domain traveling wave model. It is found that conventional split-step scheme actually is the first-order approximation to the exponential evolution matrix in the optical equations. A high-order split-step scheme is then constructed by using the Suzuki's fractal decomposition approach. Simulation results confirm its higher efficiency over the conventional split-step scheme for the simulation of DFB lasers.

From chapter 4 to chapter 7, the thesis is devoted to the development of the standing wave model where the optical field is decomposed into a set of optical modes resonating in the laser cavity. Existing SWMs are based on the expansion of instantaneous modes, also known as "hot" cavity modes under floating bias. This means that these eigenmodes are changing with the injection level, therefore is time-dependent. Searching for multiple time-dependent potential lasing modes in the complex domain is by no means an easy task especially when the mode hopping happens, although the number of eigenmodes used in the expansion can be kept to a minimum in this scheme. Chapter 4 and 5 developed two alternative SWMs based on the different selection of eigenmodes. The common feature of them is that eigenmodes are obtained at certain fixed reference point and only need to be searched once as a priori knowledge. This reduces the complexity of the existing model dramatically; however, as a trade-off, the number of eigenmodes has to be increased to make sure the coverage of the potential lasing mode when the bias is changing. For DFB lasers, the number of eigenmodes is expected to be limited due to the good mode-selectivity of the structure. Actually, we may find that the difference between the existing SWM and proposed ones are analogous to the local mode and global mode expansion in modelling passive waveguides, respectively. On the other hand, in comparison with the TWM, the proposed SWMs also exhibit higher efficiency in modelling DFB lasers due to the reason that a larger time step can be adopted in the

SWM. This is attributed to the fact that, in the TWM, the time step is scaled with the spatial mesh which has to be fine enough to catch the variation of optical fields; as such an unnecessarily small time step has to be applied. But this limitation of the time step is not required for the SWM, resulting in a higher efficiency. This has been confirmed by way of examples.

In chapter 4, the optical modes are solved under the "cold" cavity, i.e. the cavity without any current injection. Mathematically these eigenmodes are represented by the eigenvalues and eigenfunctions of the "cold" cavity operator. Then, the optical field is expanded in terms of these eigenmodes. In other words, the space and time dependence of the optical field are separated, consequently resulting in a set of ordinary differential equations (ODEs) governing the time evolution of the modal complex amplitudes. The validity and efficiency of the model are demonstrated through simulation examples. This is then followed by the discussion of the impact of the mode truncation effects on the accuracy of the model. It is worth mentioning that the coupling strength of the grating is assumed to be bias-independent, and hence this model is applicable to simulate the index-coupled DFB lasers.

Chapter 5 presents an alternative standing wave model whose derivation follows a similar procedure as described in chapter 4. The difference is that the eigenmodes are now chosen to be threshold "hot" cavity modes, i.e. they are obtained when the laser is biased at threshold, and also needed to be searched for once. This model is aiming at simulating gain-coupled DFB lasers where the coupling strengths of gratings are dependent on the bias. The reasons we select modes at threshold as expansion basis are 1) the carriers are somewhat clamped above threshold, and hence the coupling strength is mostly determined near threshold condition; 2) the threshold "hot" cavity modes are solely determined by the structure and material parameters, and are independent of the operating condition, which facilitates the root searching process.

The SWMs proposed in chapter 4 and 5 focus on solultion techniques of optical field equations. Chapter 6, on the other hand, develops a more efficient solution to the standing wave model with the approximation of the carrier shape evolution under the moderate power assumption. Basically, the carrier density distribution can be related to the photon density distribution due to their highly correlated patterns. Physically, this can be understood that the carriers are consumed more where the light intensity is strong. Mathematically, the relations between these two distributions are also derived along with the scope of validity for the assumptions. With the approximation of the carrier density distribution, the complexity of the standing wave models discussed previously is then reduced considerably.

In chapter 7 an attempt is made to build the linkage between 0D model and 1D model for simulating DFB lasers. The multimode photon number and phase rate equations are derived from the 1D photon wave equations of the SWM proposed previously. They can be reduced into a similar form of rate equations used in 0D models so that the relations of parameters between these two models can be explicitly established. This should be of practical significance for system designers to understand and predict the various behaviors of the DFB lasers.

Chapter 8 presents a novel design concept of the single-longitudinal-mode DFB laser incorporating the dispersive grating. It is known that the conventional uniform-grating DFB laser has the intrinsic drawback of the dual-mode operation. Several solutions to this problem are first reviewed. Later, the dispersive grating is introduced. The coupling strength of this grating has the wavelength-dependent property so that one more wavelength selection mechanism is realized, leading to the single-mode operation of the conventional uniform-grating DFB laser. The previously proposed modeling technique is successfully applied to evaluate the novel design.

Finally, chapter 9 summarizes the major research achievements in this thesis and lists suggestions for future work.

Chapter 2

1D Numerical Models for DFB Lasers

2.1 Introduction

In fiber-optic communication systems, the optical source with the properties of stable single-mode operation and narrow spectral linewidth are highly desired [38]. The most widely used laser structure is the DFB laser, or less frequently the DBR laser, where an etched diffraction grating is included within the laser cavity, acting as a wavelength selective mechanism. In DFB lasers, the grating is integrated with the active laser along the whole length of the cavity. In contrast, DBR lasers have the passive grating which is separated from the gain region. The schematic diagrams for these two structures are shown in Figure 2.1.

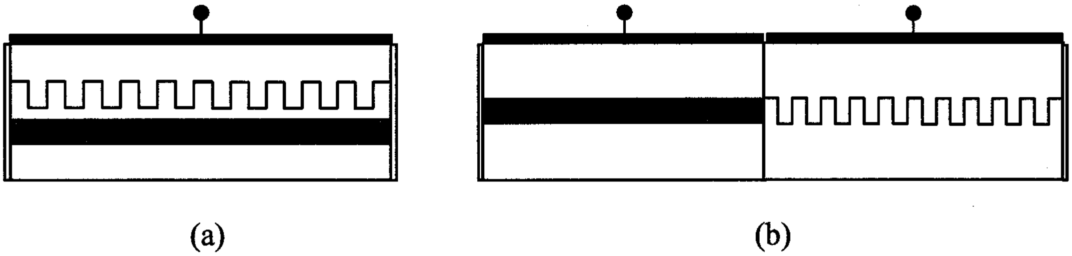

Figure 2.1 Schematic diagram for (a) the DFB laser and (b) the DBR laser

The working principle of a uniform-grating DFB laser with AR-coated facets was first explained by Kogelnik and Shank using the coupled-wave theory [19] where only the threshold analysis are carried out. More complicated designs of DFB lasers such as $\lambda/4$ or $2\times\lambda/8$ phase-shifted devices [39], [40] have called for efficient numerical models for device optimization and development. These models should be able to predict both the static and dynamic performances of the laser diode. The laser dynamics involve the nonlinear interplay between the carriers and photons inside the laser cavity. The optical waves inside a resonator are travelling back and forth, and interacting with the gain medium along the laser cavity. These waves suffer losses, but also experience the optical gain caused by the holes and electrons being stimulated into recombining at a rate which increases with the injected carrier density. Generally speaking, such laser dynamics need to be described by three equations, one for the field, one for the carrier and one for the polarization. In a semiconductor laser, the decay time of the polarization is normally smaller than the decay time of the optical field. This means that the polarization can respond to the field instantaneously, as such the polarization can be adiabatically eliminated. However, this is not true for the carrier which has a decay time much longer than that of the field. As a result, two sets of equations will be necessary to describe the dynamic characteristics of the semiconductor lasers: the hyperbolic partial differential equations governing the complex amplitude of the optical field (in fact, its slow varying envelope) nonlinearly coupled with a set of ordinary differential equations governing the carrier density within the active region of the laser cavity. These two subsystems are solved in a self-consistent manner.

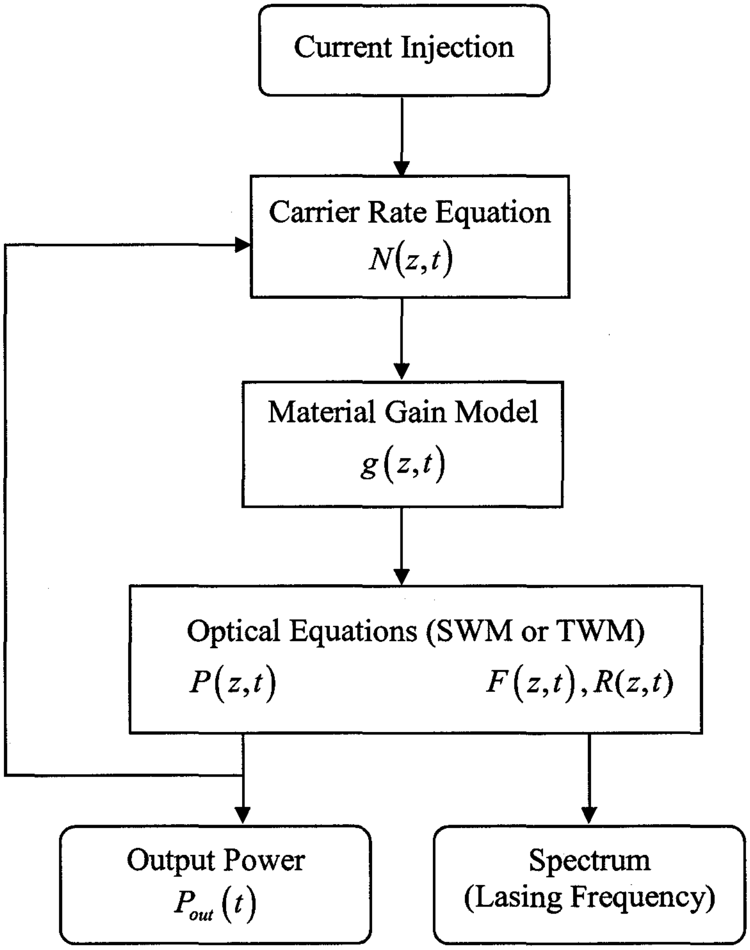

Figure 2.2 Simulation process of 1D model used in this thesis

Shown in Figure 2.2 is the diagram of the basic simulation process adopted in this thesis. It is worth mentioning that temperature-induced variations in the performance of semiconductor lasers are not considered here. This effect can be readily included by adding the heat transfer equation as described in [41], [42], if necessary. This 1D model is able to carry out the following analysis:

- Threshold Analysis
- Steady state analysis
- Small-signal analysis
- Large-signal analysis
- Spectrum analysis*
- Noise analysis*

* Although the gain dispersion effect can be neglected for DFB Lasers in most cases, accurate spectrum analysis is achieved if the gain dispersion is included. The noise analysis can also be carried out by adding a Langevin noise term to the carrier rate equation, which is not included in this thesis.

The governing equations for each function block in Figure 2.2 will be introduced in Sec. 2.2. Two different 1D simulation methods for DFB lasers, namely the traveling wave model and the standing wave model will be described in Sec. 2.3 and Sec. 2.4, respectively.

2.2 Governing Equations

2.2.1 Optical Field Equations

From the well-known Maxwell's equations, the time-dependant coupled-wave equations which govern the slowly varying envelopes $F(z,t)$ and $R(z,t)$ of the forward and backward traveling optical fields in active/passive devices can be written as [43]

$$\frac{1}{\upsilon_g}\frac{\partial F(z,t)}{\partial t}+\frac{\partial F(z,t)}{\partial z}=\left(\frac{\Gamma g}{2}-\frac{\alpha_i}{2}-j\delta\right)F(z,t)+j\kappa_f R(z,t)+\tilde{s}_f(z,t), \tag{2.1}$$

$$\frac{1}{\upsilon_g}\frac{\partial R(z,t)}{\partial t}-\frac{\partial R(z,t)}{\partial z}=\left(\frac{\Gamma g}{2}-\frac{\alpha_i}{2}-j\delta\right)R(z,t)+j\kappa_r F(z,t)+\tilde{s}_r(z,t) \tag{2.2}$$

where υ_g is the group velocity, α_i is the internal loss and Γ is the optical confinement factor describing the proportion of the optical power that travels within the active region. κ_f (κ_r) is the coupling coefficient that couples the backward (forward) into the forward (backward) wave due to the grating. Their general form can be written as [44], [45]

$$\begin{aligned}\kappa_f &= \left(\kappa_i + j\kappa_g\right)e^{j\theta(z)}\\ k_r &= \left(\kappa_i + j\kappa_g\right)e^{-j\theta(z)}\end{aligned} \tag{2.3}$$

where κ_i and κ_g are real numbers denoting the coupling coefficient of the index and gain grating, respectively. Equation (2.3) assumes that the phase difference between the gain and index grating is either π $\left(\kappa_i\kappa_g < 0\right)$ or $0\left(\kappa_i\kappa_g > 0\right)$. This assumption is valid due to the reason that, from the experimental point of view, κ_i and κ_g are most likely caused by the "same" geometric grating. Theoretically, these two cases are also shown to be most advantageous [46]. $\theta(z)$ defines the initial phase of the grating and its z-dependency takes the phase-shifted grating into account if the multi-section structure is considered. For the single-section uniform DFB grating with zero initial phase, we have

1) $\kappa_f = \kappa_r = \kappa_i$ for a pure index grating, i.e. $\kappa_f = \kappa_r^*$ ($\kappa_g = 0$)

2) $\kappa_f = \kappa_r = j\kappa_g$ for a pure gain grating, i.e. $\kappa_f = -\kappa_r^*$ ($\kappa_i = 0$)

3) $\kappa_f = \kappa_r = \begin{cases} \kappa_i + j\kappa_g \text{ with } \kappa_i\kappa_g > 0 & \text{for an in-phase complex grating} \\ \kappa_i + j\kappa_g \text{ with } \kappa_i\kappa_g < 0 & \text{for an anti-phase complex grating} \end{cases}$

As a result, we may define that

$$\kappa_f = \kappa_r \equiv \kappa \tag{2.4}$$

where κ can be real, imaginary or complex, depending on the detailed structure of the grating.

The parameters g is the material gain given by

$$g = \frac{g_N (N - N_0)}{1 + \varepsilon P}. \tag{2.5}$$

where g_N is the differential gain coefficient, N_0 is the carrier density at transparency, ε is the nonlinear gain saturation coefficient and P is the photon density given by $|F|^2 + |R|^2$. This empirical model is generally used for describing the semiconductor laser and proven to be very successful [5], [47]. The parameters in the above gain model can be determined either through fitting from numerically calculated gain or from experimental data [48], [49]. It is worth mentioning that Eq. (2.5) is valid for bulk active region. The logarithmic gain model is a better approximation to the peak gain for quantum well active region although Eq. (2.5) can still be used in a limited range [50].

The detuning factor δ in Eq. (2.1) and (2.2) denotes the deviation in propagation constant from Bragg condition,

$$\delta = \frac{2\pi}{\lambda_0}\left(n_{eff}^0 + \Delta n\right) - \frac{\pi}{\Lambda} . \tag{2.6}$$

where λ_0 is the reference wavelength, n_{eff}^0 is the effective refractive index without injection, and Λ is the grating period. In semiconductor lasers, a change in gain Δg will be accompanied by a change in refractive index Δn via the Kramers-Kronig (K-K) relations [51]. The linewidth enhancement factor α_m, also known as Henry's factor, defines the ratio of these two changes as [42]

$$\alpha_m = -\frac{dn/dN}{dg/dN} \cdot \frac{4\pi}{\lambda_0} . \tag{2.7}$$

By the definition of Eq. (2.7), α_m is a positive dimensionless number. Using Eq. (2.7) and choosing $\lambda_0 = 2n_{eff}^0\Lambda$, Eq. (2.6) becomes

$$\delta = -\frac{1}{2}\alpha_m \Gamma g . \tag{2.8}$$

Equations (2.1) and (2.2) can then be written as

$$\frac{1}{\upsilon_g}\frac{\partial F(z,t)}{\partial t} + \frac{\partial F(z,t)}{\partial z} = \left[\frac{\Gamma g}{2}\left(1 + j\alpha_m\right) - \frac{\alpha_i}{2}\right] F(z,t) + j\kappa R(z,t) + \tilde{s}_f(z,t) \tag{2.9}$$

$$\frac{1}{\upsilon_g}\frac{\partial R(z,t)}{\partial t} - \frac{\partial R(z,t)}{\partial z} = \left[\frac{\Gamma g}{2}\left(1 + j\alpha_m\right) - \frac{\alpha_i}{2}\right] R(z,t) + j\kappa F(z,t) + \tilde{s}_r(z,t) . \tag{2.10}$$

Finally, $\tilde{s}_f$ and $\tilde{s}_r$ denote the spontaneous emission noises which can be approximated as Gaussian random processes with zero mean [5] and satisfying the following correlation relation

$$\left\langle \tilde{s}_{f,r}(z,t)\tilde{s}_{f,r}^{*}(z',t')\right\rangle = K_{tr}\Gamma\beta R_{sp}L\delta(z-z')\delta(t-t')/\upsilon_g^2 \tag{2.11}$$

where L is the length of the laser cavity, K_{tr} is the transverse Petermann factor, β is the spontaneous coupling factor, δ denotes the Dirac delta function and R_{sp} is the spontaneous recombination rate which will be discussed in the next section.

With a laser cavity of length L extending from $z=0$ to $z=L$, the boundary conditions at the terminating facets are given by

$$F(0,t)=r_1R(0,t),\ R(L,t)=r_2F(L,t) \tag{2.12}$$

where r_1 and r_2 are the field reflectivity of the left and right facet, respectively. Through this boundary condition of the longitudinal equation, the mirror losses enter the formalism in a very natural way.

The output power from the left or right facet can be obtained from the photon density at $z=0$ or $z=L$, respectively [43], [52]

$$P_{out}^{L}(t)=\frac{dw}{\Gamma}\upsilon_g\frac{hc}{\lambda_0}\left(1-r_1^2\right)\left(\left|F(0,t)\right|^2+\left|R(0,t)\right|^2\right) \tag{2.13}$$

$$P_{out}^{R}(t)=\frac{dw}{\Gamma}\upsilon_g\frac{hc}{\lambda_0}\left(1-r_2^2\right)\left(\left|F(L,t)\right|^2+\left|R(L,t)\right|^2\right) \tag{2.14}$$

with h being the Planck's constant, w and d the width and the thickness of the active layer respectively.

2.2.2 Carrier Rate Equation

The change of the carrier density N inside the active region is governed by a rate equation describing the generation and recombination of carriers from the viewpoint of particle balance

$$\frac{dN}{dt} = R_{gen} - R_{rec} \tag{2.15}$$

The first term on the right-hand side R_{gen} is the rate of injected carrier due to the external pumping given by

$$R_{gen} = \frac{\eta_i I}{eV_a} \tag{2.16}$$

where I is the injected current, e the electron charge, η_i the injection efficiency and V_a is the volume of the active region of the laser diode ($V_a = wdL$).

The second term on the right-hand side R_{rec} is the recombination rate of carriers including four physical processes as follows

$$R_{rec} = R_{sp} + R_{nr} + R_l + R_{st} \tag{2.17}$$

where R_{sp} is the spontaneous radiative recombination rate with $R_{sp} \sim BN^2$; R_{nr} is the nonradiative recombination rate with $R_{nr} \sim AN + CN^3$; R_{st} is the net stimulated recombination rate with $R_{st} \sim \upsilon_g gP$ which leads to the emission of the coherent light. The coefficient A, B and C are the linear recombination coefficient, the bimolecular recombination coefficient and the Auger recombination coefficient, respectively. The term R_l is a carrier leakage rate due to lateral/transverse diffusion which is often negligible, consequently will not be included here. Thus, the carrier density rate equation (2.15) may be written as [42], [53], [54]

$$\frac{dN}{dt} = \frac{\eta_i I}{eV_a} - AN - BN^2 - CN^3 - \upsilon_g gP. \tag{2.18}$$

It is important to note that there is no Γ in the stimulated emission term of Eq. (2.18) while it appears in the carrier number rate equations. This is due to the fact that the carrier density is defined with respect to the active-region volume V_a, but the photon density is to the mode volume V_p. It is known that the photon will have a distribution extending beyond the active region with $V_p = V_a / \Gamma$. The density version will be used through out this thesis.

Also, it is worth mentioning, the carrier density *N* is a function of position *z* and time *t* in 1D models, although we didn't explicitly write this dependency in this section.

2.3 Traveling Wave Model

The traveling wave model is composed of a hyperbolic system of PDEs, i.e. the time-dependent coupled-wave equations (2.9) and (2.10), nonlinearly coupled with a system of ODEs, i.e., carrier density rate equations (2.18) at different positions. They are solved self-consistently through tracing explicitly the evolution of envelopes of the field amplitudes for the forward and backward propagating modes in the temporal and spatial domain. In general, the structure is discretized along the waveguide axis into a number of subsections so that tractable solutions can be derived for the subsections and cascaded for the entire structure. Consider a laser cavity of length L which is divided into M subsections, we may setup a mesh as shown in Figure 2.3.

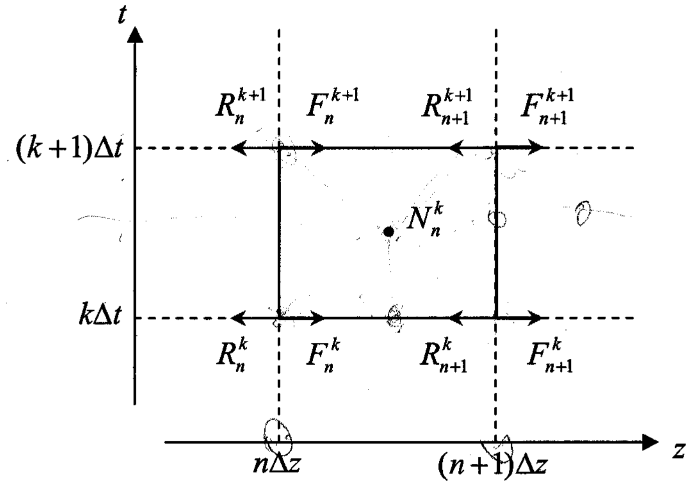

Figure 2.3 Discretization of the spatial-temporal domain

The spatial sampling interval is $\Delta z = L/M$ and the time sampling interval is Δt. The complex fields sampled at the boundary are denoted as

$$F(n\Delta z, k\Delta t) \equiv F_n^k \text{ and } R(n\Delta z, k\Delta t) \equiv R_n^k \tag{2.19}$$

where the superscript $k(=1, 2, \cdots, \infty)$ denotes the time step and the subscript $n(=1, 2, \cdots, M)$ denotes the space step.

The carrier rate equation (2.18) can be easily solved by the standard Euler methods as

$$N_n^{k+1} = N_n^k + \Delta t \left[\frac{\eta_i I_n^k}{eV_a} - AN_n^k - B\left(N_n^k\right)^2 - C\left(N_n^k\right)^3 - \upsilon_g g_n^k P_n^k \right] \tag{2.20}$$

Meanwhile, for optical field equations, several large signal dynamic models with different level of details and assumptions [55]-[61] have been developed for solving the time-dependent coupled-wave equations. In this section, they are introduced and compared under a unified framework.

2.3.1 Unified Framework of Existing Time-Domain Solution Schemes

Generally, there are two strategies to construct an algorithm for solving Eqs. (2.9) and (2.10). The most straightforward approach is to directly discretize the derivative with respect to time and space. The other is to approximate the formally exact solution by the approximation evolution matrix. We will discuss both of these two strategies, then review and compare existing solution schemes in their respective category as follows.

A. Finite-Difference (FD) Based Methods

The FD method is a well-known class of solution schemes to Eqs. (2.9) and (2.10) which can be written as

$$(\frac{1}{\upsilon_g}\frac{\partial}{\partial t}\pm\frac{\partial}{\partial z})\boldsymbol{\psi}=\mathbf{H}'\boldsymbol{\psi}+\tilde{\mathbf{s}} \tag{2.21}$$

where the column vector $\boldsymbol{\psi}=\begin{bmatrix} F(z,t) \\ R(z,t) \end{bmatrix}$, $\tilde{\mathbf{s}}=\begin{bmatrix} \tilde{s}_f(z,t) \\ \tilde{s}_r(z,t) \end{bmatrix}$ and

$$\mathbf{H}'=\begin{bmatrix} Q & j\kappa \\ j\kappa & Q \end{bmatrix} \tag{2.22}$$

with

$$Q=\frac{1}{2}\Gamma g\left(1+j\alpha_m\right)-\frac{\alpha_i}{2}. \tag{2.23}$$

Equation (2.21) can then be transformed into a matrix equation by approximating the derivatives with a FD formula. A first-order finite difference approximation to the partial derivatives in Eq. (2.21) reads

$$\begin{aligned} \frac{\partial F}{\partial t}&=\frac{F_{n+1}^{k+1}-F_{n+1}^{k}}{\Delta t} & \frac{\partial F}{\partial z}&=\frac{F_{n+1}^{k}-F_{n}^{k}}{\Delta z} \\ \frac{\partial R}{\partial t}&=\frac{R_{n-1}^{k+1}-R_{n-1}^{k}}{\Delta t} & \frac{\partial R}{\partial z}&=\frac{R_{n}^{k}-R_{n-1}^{k}}{\Delta z} \end{aligned} \tag{2.24}$$

Plug Eq. (2.24) into (2.21), the final marching scheme can be derived as

$$\begin{bmatrix} F_{n+1}^{k+1} \\ R_{n-1}^{k+1} \end{bmatrix}=(1-\eta_r)\begin{bmatrix} F_{n+1}^{k} \\ R_{n-1}^{k} \end{bmatrix}+\eta_r\left(\mathbf{I}+\mathbf{H}'\Delta z\right)_{n,k}\begin{bmatrix} F_{n}^{k} \\ R_{n}^{k} \end{bmatrix}+\eta_r\Delta z\begin{bmatrix} \tilde{s}_{fn}^{k} \\ s_{rn}^{k} \end{bmatrix} \tag{2.25}$$

where $\eta_r=\upsilon_g\Delta t/\Delta z$, $\mathbf{I}$ denotes the unitary matrix and the parameters Q and κ in $\mathbf{H}'$ are assumed to be constants within each subsection.

We may notice that the FD scheme in Eq. (2.24) is actually the forward-time backward-space (FTBS) scheme. The consistency of this scheme is proved in Appendix A. The stability of this scheme can be studied by using the well-known Von Neumann Analysis [62] which is also presented in Appendix A where the stability condition is derived to be $\eta_r\le 1$. The condition $\eta_r=1$, i.e. $\Delta t=\Delta z/\upsilon_g$, is usually adopted to bring the maximum computation efficiency, leading to the marching scheme in [55], [56].

$$\begin{bmatrix} F_{n+1}^{k+1} \\ R_{n-1}^{k+1} \end{bmatrix}=\left(1+Q\Delta z\right)_{n,k}\begin{bmatrix} F_{n}^{k} \\ R_{n}^{k} \end{bmatrix}+j\kappa\Delta z\begin{bmatrix} R_{n}^{k} \\ F_{n}^{k} \end{bmatrix}+\Delta z\begin{bmatrix} \tilde{s}_{fn}^{k} \\ s_{rn}^{k} \end{bmatrix} \tag{2.26}$$

There are three other first-order FD schemes, namely the forward-time forward-space (FTFS) scheme, the backward-time forward-space (BTFS) scheme and the backward-time backward-space (BTBS) scheme. Through a similar method shown in Appendix A, it can be proved that

1) FTFS scheme is consistent, but not stable;

2) BTFS is consistent and stable for $\eta_r > 1$;

3) BTBS scheme is consistent and unconditionally stable.

The BTFS and BTBS scheme are implicit schemes, consequently involving considerable extra computation burden. It is also found that the second order FD schemes such as the Crank-Nicholson scheme and box scheme can achieve a higher accuracy with the properties of unconditionally stable. However they are also implicit [63]. As a result, the explicit first-order FTBS FD approximation is still preferred in most cases compared with the implicit schemes and its resulting solution scheme allows for easy implementations and the fast computational speed.

B. Methods Based on Approximations to the Formal Solution

The optical field equations (2.9) and (2.10) can be reformatted into the following matrix form:

$$\frac{\partial \psi}{\partial z} = \mathbf{H}_{\mathbf{z}}\psi + \tilde{\mathbf{s}} \tag{2.27}$$

where the matrix operator $\mathbf{H}_{\mathbf{z}}$ is defined as

$$\mathbf{H}_\mathbf{z} = \begin{bmatrix} Q - \upsilon_g^{-1}(\partial/\partial t) & j\kappa \\ -j\kappa & -Q + \upsilon_g^{-1}(\partial/\partial t) \end{bmatrix}. \tag{2.28}$$

The formal solution of Eq. (2.27) takes the following form

$$\begin{aligned} \psi(z+\Delta z) &= e^{\Delta z \mathbf{H}_z}\psi(z) + \int_z^{z+\Delta z} e^{(z+\Delta z-u)\mathbf{H}_z}\tilde{\mathbf{s}}(u,t)du \\ &\doteq e^{\Delta z \mathbf{H}_z}\left[\psi(z) + \tilde{\mathbf{s}}(z,t)\Delta z\right] \end{aligned}. \tag{2.29}$$

The other class of solution schemes is based on the approximation to the evolution matrix operator $e^{\Delta z \mathbf{H}_z}$. They are introduced as follows:

1) *Weak Coupling Approximation (WCA) Method* [57], [58]

The off-diagonal terms of the operator $\mathbf{H}_\mathbf{z}$ in Eq. (2.28) represent the cross-coupling between contra-propagating waves inside the laser cavity and they are normally much smaller than the self-coupling terms, i.e. the diagonal terms of $\mathbf{H}_\mathbf{z}$. Under this assumption, the cross-coupling effects can be viewed as a perturbation to the self-coupling ones. Firstly, by neglecting cross-coupling terms, the evolution matrix operator can be approximated by

$$e^{\Delta z \mathbf{H}_z} \approx \begin{bmatrix} e^{Q\cdot\Delta z} e^{-\frac{\Delta z}{\upsilon_g}\frac{\partial}{\partial t}} & 0 \\ 0 & e^{-Q\cdot\Delta z} e^{\frac{\Delta z}{\upsilon_g}\frac{\partial}{\partial t}} \end{bmatrix}, \tag{2.30}$$

such that

$$\begin{bmatrix} F_{n+1}^k \\ R_{n+1}^k \end{bmatrix} = \begin{bmatrix} e^{Q\Delta z} e^{-\frac{\Delta z}{\upsilon_g}\frac{\partial}{\partial t}} & 0 \\ 0 & e^{-Q\Delta z} e^{\frac{\Delta z}{\upsilon_g}\frac{\partial}{\partial t}} \end{bmatrix}_{n,k} \begin{bmatrix} F_n^k \\ R_n^k \end{bmatrix}. \tag{2.31}$$

It is known that the forward propagating wave F travels from n to n+1 in space, but the backward propagating wave R travels from n+1 to n. After reordering Eq. (2.31), we have

$$e^{\frac{\Delta z}{\upsilon_g}\frac{\partial}{\partial t}}\begin{bmatrix} F_{n+1}^k \\ R_n^k \end{bmatrix} = \begin{bmatrix} e^{Q\cdot\Delta z} & 0 \\ 0 & e^{Q\cdot\Delta z} \end{bmatrix}_{n,k} \begin{bmatrix} F_n^k \\ R_{n+1}^k \end{bmatrix}. \tag{2.32}$$

The final marching scheme is obtained after adding back the perturbative cross-coupling terms and the noise,

$$\begin{bmatrix} F_{n+1}^{k+1} \\ R_n^{k+1} \end{bmatrix} = e^{Q\Delta z}\begin{bmatrix} F_n^k \\ R_{n+1}^k \end{bmatrix} + j\kappa\Delta z\begin{bmatrix} R_{n+1}^k \\ F_n^k \end{bmatrix} + \Delta z\begin{bmatrix} \tilde{s}_{fn}^k \\ s_{rn}^k \end{bmatrix} \tag{2.33}$$

where $\Delta t = \Delta z/\upsilon_g$ and the following relation have been used

$$e^{\Delta t\frac{\partial}{\partial t}} f_n^k = \left[1 + \frac{\partial}{\partial t}\Delta t + \frac{1}{2!}\frac{\partial^2}{\partial t^2}(\Delta t)^2 + \cdots\right] f_n^k = f_n^{k+1} \tag{2.34}$$

with f can be either F or R. Comparing Eq. (2.33) with the FD scheme Eq. (2.26), we found that the linear term in Eq. (2.26) is actually the first-order approximation of the exponential term in Eq. (2.33).

2) *Instantaneous Complex Frequency (ICF) Method* [59]

If the assumption is made that the fields vary in time as

$$\frac{1}{v_g}\frac{\partial}{\partial t}\begin{bmatrix} F(z,t) \\ R(z,t) \end{bmatrix} \approx \Omega(z,t)\begin{bmatrix} F(z,t) \\ R(z,t) \end{bmatrix}, \tag{2.35}$$

the evolution matrix operator in Eq. (2.29) becomes

$$e^{\Delta z\cdot\mathbf{H}_z} \approx e^{\mathbf{H}_z'} \tag{2.36}$$

with

$$\mathbf{H}_z' = \begin{bmatrix} (Q-\Omega)\Delta z & jk\Delta z \\ -jk\Delta z & (-Q+\Omega)\Delta z \end{bmatrix} \tag{2.37}$$

The matrix in Eq. (2.37) can be diagonalized by finding its eigenvalues, taking its exponential and transforming it into the proper order. Finally, Eq. (2.29) gives:

$$\begin{bmatrix} F_{n+1}^{k+1} \\ R_n^{k+1} \end{bmatrix} = \frac{e^{\Omega \cdot \Delta z}}{\gamma \cosh(\gamma\Delta z) - (Q-\Omega)\sinh(\gamma\Delta z)} \begin{bmatrix} \gamma & j\kappa \sinh(\gamma\Delta z) \\ j\kappa \sinh(\gamma\Delta z) & \gamma \end{bmatrix} \begin{bmatrix} F_n^k \\ R_{n+1}^k \end{bmatrix} + \Delta z \begin{bmatrix} \tilde{s}_{fn}^k \\ s_{rn}^k \end{bmatrix} \tag{2.38}$$

where $\gamma^2 = (Q-\Omega)^2 + \kappa^2$ and Ω can be estimated from the previous time step as

$$\Omega = \left[\ln\left(F_n^k / F_n^{k-1}\right)/\Delta z + \ln\left(R_n^k / R_n^{k-1}\right)/\Delta z\right]/2 \tag{2.39}$$

where $\Delta t = \Delta z / \upsilon_g$ is also applied.

3) *The Split-Step (SS) Method* [60], [61]

Another popular method for solving the time-dependent coupled-wave equations is called the split-step time-domain model (SS-TDM). As the name itself implies, this method is based on the operator split, i.e. the operator $\mathbf{H}_z$ in Eq. (2.28) can be split into a field propagation operator $\mathbf{H}_1$ and coupling operator $\mathbf{H}_2$ as follows

$$\mathbf{H}_1 = \begin{bmatrix} Q - \upsilon_g^{-1}(\partial/\partial t) & 0 \\ 0 & -Q + \upsilon_g^{-1}(\partial/\partial t) \end{bmatrix}, \tag{2.40}$$

$$\mathbf{H}_2 = \begin{bmatrix} 0 & j\kappa \\ -j\kappa & 0 \end{bmatrix}. \tag{2.41}$$

In this algorithm, the evolution matrix operator in Eq. (2.29) becomes

$$e^{\Delta z \mathbf{H}_z} \approx e^{\Delta z \mathbf{H}_1} e^{\Delta z \mathbf{H}_2} \tag{2.42}$$

The solution can be obtained by solving the two exponential operators in Eq. (2.42) sequentially within each subsection. The final marching scheme is derived to be

Step 1:
$$\begin{bmatrix} F_{n+1}^{k+1} \\ R_{n}^{k+1} \end{bmatrix} = \begin{bmatrix} e^{Q\cdot\Delta z} & 0 \\ 0 & e^{Q\cdot\Delta z} \end{bmatrix} \begin{bmatrix} F_{n}^{k} \\ R_{n+1}^{k} \end{bmatrix} + \Delta z \begin{bmatrix} \tilde{s}_{fn}^{k} \\ s_{rn}^{k} \end{bmatrix} \tag{2.43}$$

Step 2:
$$\begin{bmatrix} F_{n+1}^{k} \\ R_{n}^{k} \end{bmatrix} = \begin{bmatrix} \operatorname{sech}(\kappa\Delta z) & j\tanh(\kappa\Delta z) \\ j\tanh(\kappa\Delta z) & \operatorname{sech}(\kappa\Delta z) \end{bmatrix} \begin{bmatrix} F_{n}^{k} \\ R_{n+1}^{k} \end{bmatrix} \tag{2.44}$$

During the derivation, the relation $\Delta t = \Delta z / \upsilon_g$ and Eq. (2.34) are also used. This scheme also assumes that all parameters within each subsection are all constants.

C. Scheme Comparisons

The FD based methods, although have the advantages of simplification and fast speed, require very fine mesh in order to achieve high-degree of accuracy, especially when the variation of the field is large along the waveguide. It is shown that a very fine mesh of $\Delta z \leq 10\mu m$ is necessary in order to obtain a satisfying accuracy [55].

The week coupling approximation method use an exponential term to express the incremental change of the amplitude and phase of the optical field during the self-coupling process. Eq. (2.33) reduces to the exact solution for the FP laser in the absence of gratings. As such, it is concluded that this scheme is more accurate than the FD scheme of Eq. (2.26). However the improvement is limited due to the restriction to the coupling coefficient.

In the instantaneous complex frequency method, $\Omega(z,t)$ is estimated from the previous calculated results and assumed to be a constant within each time step such that the exact solution to the spatial variation of the field can be obtained, consequently is shown to be more accurate than the previous two methods. However, it requires that the complex fields can not change drastically over a single time step. The inherent instability of the algorithms becomes more serious when large detuning factors and coupling coefficients are involved in the structures due to the inaccurate estimation of the instantaneous complex frequency. Moreover, the assumption that optical fields follow the harmonic time dependence puts a more stringent condition to the problem it can apply.

The split-step method is a more general scheme than the instantaneous complex frequency method. The error of this scheme comes from the non-commutative property of the divided operators in the approximation of Eq. (2.42). This error can be reduced by using a relatively small discretization Δz especially when the coupling strength is very strong. In comparison with all the previously introduced schemes, the split-step method is shown to be a more efficient algorithm under the required accuracy [61].

The above comparisons are summarized in Table 2.1.

	FD	WCA	ICF	SS
Efficiency	not efficient	efficient	very efficient	very efficient
Scope of applications	general	general	not general	general

Table 2.1 Scheme comparisons

2.3.2 Implementations

Due to the superior performance of the SS-TDM in modeling the DFB laser, its simulation results are chosen as one of benchmarks used for comparisons in the later study and development of the 1D model. The numerical implementations of this model will be verified in this section through comparing with published results in terms of the static and dynamic characteristics of the DFB laser. The laser parameters are chosen to be same as those used in the literature being compared with.

A. Static Performances

1) Light-Current (LI) Curve

The change of the output power at the facet against injection current is described by the so-called LI curve, which is obtained by allowing the turn-on transient to settle for each injection level, then averaging the output power over certain time span to reduce the effects of the intensity noise [64]. The LI curve gives a typical DC response of a laser diode, where we can also estimate the threshold current I_{th}, defined as the current required to create a threshold gain to start lasing, and the differential quantum efficiency η_d, defined as the number of photons out per electron in. One example of LI curve is calculated by the SS-TDM in Figure 2.4 with the result from reference [65] shown for comparison. It is seen that I_{th} is around 33mA and η_d is estimated to be ⊔ 42.2% from

$$\eta_d = 2\left(\frac{q}{hf}\right)\frac{dP_{out}}{dI} \tag{2.45}$$

where the factor 2 accounts for the total output power from both facets for the symmetrical structure under investigation in [65].

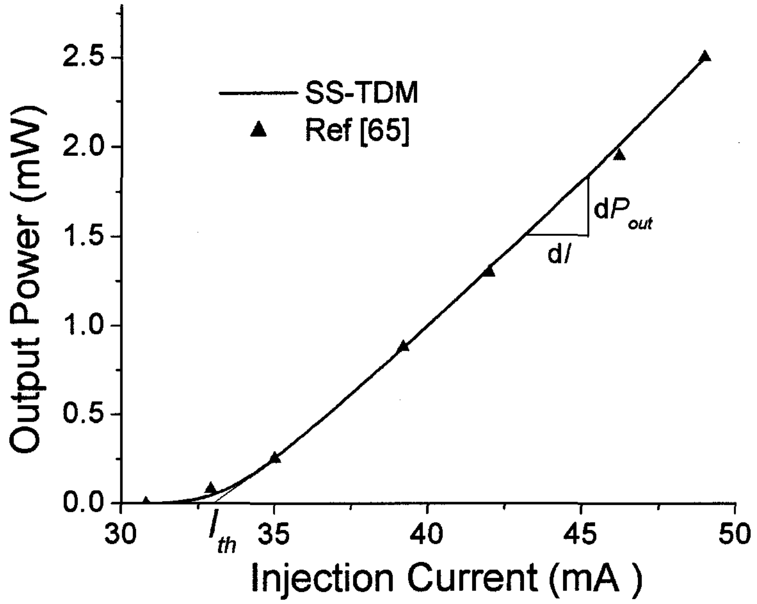

Figure 2.4 Light-current curves for the $\lambda/4$ -shifted DFB laser with $\kappa L = 2$

2) Longitudinal Carrier Density Distribution

Figure 2.5 shows the CW carrier density distribution along the longitudinal axis of the laser cavity for a quarter-wave-shifted ($\lambda/4$ -shifted) DFB laser with $\kappa L = 2$. This figure indicates the longitudinal non-uniformity of the carrier density, known as the longitudinal spatial hole burning (LSHB) effect which is prominent for the $\lambda/4$ -shifted DFB laser with $\kappa L > 1.25$ [39].

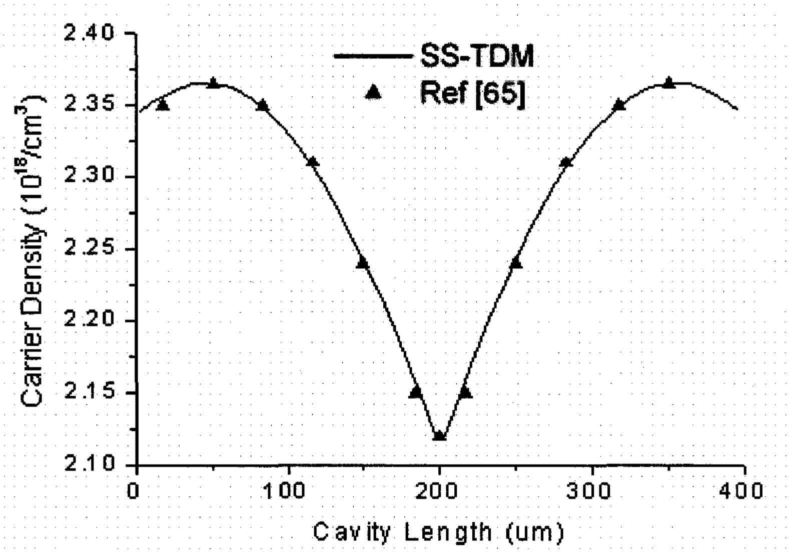

Figure 2.5 Longitudinal carrier distributions for $\lambda/4$-shifted DFB laser with $\kappa L = 2$

B. Dynamic Performances

The transient response is all important to the large signal modulation characteristics where the laser is initially biased near threshold and modulated with a current step function. Due to the mismatch between the photon life time and carrier life time, a damped oscillation of the transient response is expected to show up. Figure 2.6 shows a simulation example, where two different nonlinear gain saturation coefficients ε are applied. The relaxation oscillation frequency is ~ 2.5GHz, and the response reaches to its static state in ~ 3.5ns for $\varepsilon = 10^{-17}$. This decay time is shown to be greatly reduced with a larger nonlinear gain saturation coefficient $\varepsilon = 10^{-16}$.

Figure 2.7 calculates another example described in [57] where the optical pulses are generated by the cascade of two gain-coupled DFB sections with detuned Bragg wavelength. It is seen that SS-TDM can successfully capture the beating of two lasing modes with the beating period being approximately 1.6ps. Again this result is consistent with that in [57].

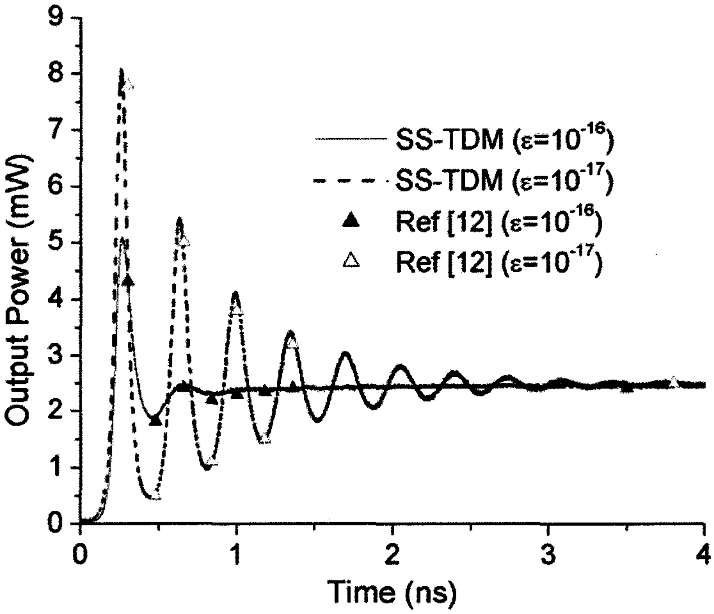

Figure 2.6 Transient responses for the $\lambda/4$-shifted DFB laser with $\kappa L = 2$

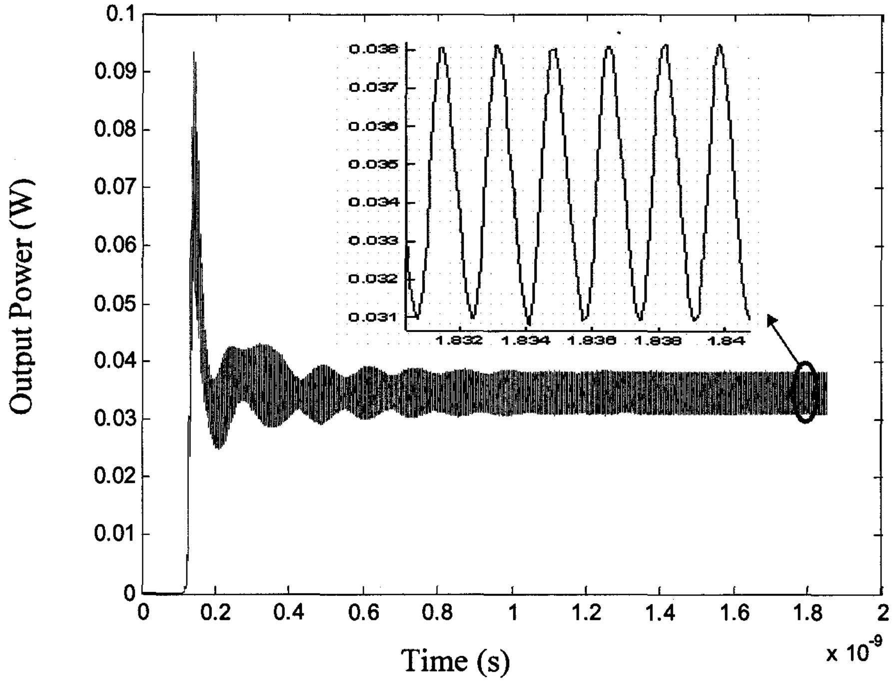

Figure 2.7 Mode beating in the two-section DFB laser

2.4 Standing Wave Model

For resonating laser structures with large variation of the carrier/photon density, the traveling wave approach is not computationally economical and also lacks the intuitive appeal. The standing wave approach [41], [66]-[68], on the other hand, assumes there exist a set of resonating spatial modes in the laser cavity and expands the optical field in terms of these modes. As such, it concerns only with the temporal evolution of the amplitudes of these modes and reduces the traveling-wave partial differential equations to a set of ordinary differential equations.

As a result, the standing wave model is composed of a system of ODEs governing the interaction between the optical field (their slow-varying envelopes) and the carrier. More details of the standing wave model will be introduced and reviewed in chapter 4.

2.5 Summary

In this chapter, the numerical 1D model and pertinent governing equations for simulating the DFB laser are first described. There are normally two numerical models, namely the TWM and the SWM, corresponding to different solution techniques. Several major existing large signal time-domain TWMs are reviewed and compared under a unified framework. The TWM by using the split-step scheme is shown to be an algorithm with higher accuracy and efficiency, consequently is implemented and verified by way of examples, with the intension of serving as one of benchmarks for the later model development. The SWM, on the other hand is briefly introduced. More details will be discussed in chapter 4.

Chapter 3

High-Order Split-Step Traveling Wave Model

3.1 Introduction

In conventional SS-TDM, the exponential operator was split into a field propagation and coupling operator as shown in Eq. (2.42). Closed-form analytical solutions are derived for both operators and overall solutions are obtained by solving the split operators consecutively along the waveguide axis in the time-domain. The main source of error of the SS-TDM comes from the non-commutative property of the divided operators. Thus far, however, only the lowest-order operator splitting has been utilized for this method.

High-order decomposition of exponential operators has been utilized and examined in different areas [69]-[77] such as quantum mechanics, statistical physics, pulse propagation in nonlinear fibers, etc. In this chapter, the high-order split-step scheme is applied to further reduce the error of the existing SS-TDM in simulating grating-based optical devices such as DFB lasers. The accuracy and efficiency of the proposed higher-order scheme are validated and assessed by way of comparisons with the conventional split-step solutions for several typical examples.

3.2 Suzuki's Construction and Symmetry Theorems for the Exponential Operator

In this section, we will first introduce two theorems related to the exponential operator approximation on which the proposed high-order split-step approach based.

Construction Theorem [72]:

For the exponential operator $\exp[\Delta z(\mathbf{H}_1 + \mathbf{H}_2 + \cdots \mathbf{H}_q)]$, if we have the following $(m\text{-}1)$th approximant:

$$\exp\left(\Delta z \sum_{j=1}^{q} \mathbf{H}_j\right) = S_{m-1}(\Delta z) + o(\Delta z^m) \ , \tag{3.1}$$

the mth approximant $S_m(x)$ is constructed as follows:

$$S_m(\Delta z) = \prod_{j=1}^{r} S_{m-1}(p_{m,j}\Delta z), \tag{3.2}$$

for $r \geq 2$, where the parameters $\{p_{m,j}\}$ are the solutions of the following decomposition condition that

$$\sum_{j=1}^{r} p_{m,j}^{m} = 0, \text{ with } \sum_{j=1}^{r} p_{m,j} = 1. \tag{3.3}$$

It is noticed that, in Eq. (3.3), the superscript "m" denotes the mth power of p and the subscript indicates the index of p. This theorem presents a general scheme to find a systematic series of approximants to the exponential operator by using a recursion method and its proof can be found in [72].

Symmetry Theorem [70], [72]:

If the original operator $F(x)$ with a parameter x is symmetric in the sense that

$$F(x)F(-x) = 1; \quad F(0) = 1, \tag{3.4}$$

and for it we construct a symmetric (2m-1)th order approximant $S_{2m-1}(x)$, namely,

$$F(x) = S_{2m-1}\left(x\right) + o(x^{2m}), \tag{3.5}$$

where

$$S_{2m-1}(x)S_{2m-1}(-x) = 1, \tag{3.6}$$

then, $S_{2m-1}(x)$ and $S_{2m}(x)$ are both x^{2m} order accurate, namely

$$S_{2m-1}(x) = S_{2m}(x). \tag{3.7}$$

This symmetry property of decomposition was presented in [70] and proved in [72].

3.3 High-Order Split-Step Scheme

A systematic approach to construct approximations to the matrix exponential in the formal solution Eq. (2.29) is to make use of the Lie-Trotter-Suzuki product-formula [69] which states

$$S(\Delta z) = e^{\Delta z \mathbf{H}} = e^{\Delta z(\mathbf{H}_1 + \cdots + \mathbf{H}_p)} = \lim_{m \to \infty}\left(\prod_{i=1}^{p} e^{\Delta z \mathbf{H}_i / m}\right)^m. \tag{3.8}$$

Equation (3.8) suggests that

$$S_1(\Delta z) = e^{\Delta z \mathbf{H}_1} \ldots e^{\Delta z \mathbf{H}_p}. \tag{3.9}$$

It can be shown that [70]

$$\|S(\Delta z)-S_1(\Delta z)\| \le \frac{(\Delta z)^2}{2}\sum_{j>k}\left\|\left[\mathbf{H}_j,\mathbf{H}_k\right]\right\|\exp\left(\Delta z\sum_{j=1}^{p}\left\|\mathbf{H}_j\right\|\right) \tag{3.10}$$

where

$$[\mathbf{H}_j,\mathbf{H}_k]=\mathbf{H}_j\mathbf{H}_k-\mathbf{H}_k\mathbf{H}_j. \tag{3.11}$$

From Eq. (3.10) it follows that if $\mathbf{H}_j$ and $\mathbf{H}_k$ $(j \ne k)$ are non-commuting operators, $S_1(\Delta z)$ might be a good approximation to the evolution matrix $S(\Delta z)$ provided Δz is sufficiently small. In general, the Taylor series of $S(\Delta z)$ and $S_1(\Delta z)$ are identical up to first order in Δz. As a result, $S_1(\Delta z)$ is the first-order approximation to $S(\Delta z)$. The conventional split-step solution method proposed in [61] falls into this category, where the exponential operator in Eq. (2.29) is approximated by $e^{\Delta z\mathbf{H}_z} \approx e^{\Delta z\mathbf{H}_1}e^{\Delta z\mathbf{H}_2}$, with $\mathbf{H}_1$ and $\mathbf{H}_2$ defined in Eq. (2.40) and (2.41), respectively.

The simplest second-order approximant $S_2(\Delta z)$ is given by the following symmetric product [69], [72]

$$S_2(\Delta z)=S_1(\Delta z/2)S_1'(\Delta z/2)=e^{(\Delta z/2)\mathbf{H}_1}e^{(\Delta z)\mathbf{H}_2}e^{(\Delta z/2)\mathbf{H}_1}, \tag{3.12}$$

where $S_1(\Delta z/2)=e^{(\Delta z/2)\mathbf{H}_1}e^{(\Delta z/2)\mathbf{H}_2}$, $S_1'(\Delta z/2)$ is the reverse-order product of $S_1(\Delta z/2)$, i.e. $S_1'(\Delta z/2)=e^{(\Delta z/2)\mathbf{H}_2}e^{(\Delta z/2)\mathbf{H}_1}$.

By applying the Construction Theorem, the third-order symmetric approximant $S_3(\Delta z)$ can then be constructed by

$$S_3(\Delta z)=S_2(a\Delta z)S_2((1-2a)\Delta z)S_2(a\Delta z). \tag{3.13}$$

$r = 3$ in Eq. (3.3) is chosen in the construction. The reason is that for the symmetric decomposition, $r \geq 3$ should be satisfied. As a result, $r = 3$ can lead to the real symmetric decomposition with a minimum number of exponential operators. It is noted that we may carry real decomposition or complex decomposition. The real decomposition is not a requirement by Eq. (3.3). However, it is claimed that the complex coefficient decomposition is not stable and not suggested to be used for splitting the exponential operator [78]. On the other hand, one recent literature [79] claims the complex decomposition is stable for a sufficiently small step size. From our previous experience on numerical modeling, the unphysical complex number in the exponential function may cause the divergence of the program. We hence prefer to choose the real solution if the real roots can be found from Eq. (3.3) in our case. The parameter a, according to Eq. (3.3), is thus calculated to be $\left(2-\sqrt[3]{2}\right)^{-1}$, which is the real solution of the equation

$$2a^3 + (1-2a)^3 = 0. \tag{3.14}$$

We may further notice that, according to the Symmetry Theorem, the third-order symmetric approximant $S_3\left(\Delta z\right)$ is correct up to the order of x^4, i.e.

$$e^{\Delta z(\mathbf{H}_1+\mathbf{H}_2)} = S_3(\Delta z) + o(\Delta z^5) \tag{3.15}$$

By using the same construction rule recursively, the general form of high-order real symmetric decomposition reads

$$\begin{aligned} S_{2m}(\Delta z) &= S_{2m-1}(\Delta z) \\ &= S_{2m-2}(a_m \Delta z) S_{2m-2}((1-2a_m)\Delta z) S_{2m-2}(a_m \Delta z) \end{aligned}, \tag{3.16}$$

where

$$a_m = \left(2 - 2^{\frac{1}{2m-1}}\right)^{-1} . \tag{3.17}$$

Once the high-order recursion scheme is established, the numerical implementation of the high-order split-step scheme by using the conventional first-order split-step algorithm is straightforward.

In our simulation, the second-order and third-order symmetric decomposition were both implemented. It was found that the third-order scheme can bring us more salient improvement in terms of the accuracy of the simulation result. It is worth mentioning that to carry the decomposition to a very high order will not offer much in terms of the accuracy, yet add significantly in computational effort. It is found that increasing from 3rd order to 5th order, the number of exponential operators required to be calculated more than double. As a result, the third-order SS-TDM will be adopted and compared with the conventional SS-TDM in the next section.

As such, the formal solution of Eq. (2.29) is approximated by the third-order approximant as follows

$$\begin{aligned} \psi(z+\Delta z,t) &= e^{\Delta z \mathbf{H}_z}\left[\psi(z,t) + \Delta z \cdot \tilde{\mathbf{s}}(z,t)\right] \\ &\approx S_3(\Delta z)\left[\psi(z,t) + \Delta z \cdot \tilde{\mathbf{s}}(z,t)\right] \end{aligned} . \tag{3.18}$$

3.4 Model Validation and Applications

A. Distributed Bragg Reflectors (DBR)

The reflection property of the corrugated waveguide is investigated as the first example to examine the high-order split-step scheme. We calculate the reflection spectrum of the distributed Bragg reflector with $\kappa L = 6$ (the product of coupling coefficient and length). Simulation results of the third-order scheme and the conventional first-order scheme are both shown in Figure 3.1 where the exact analytical solution [80] (solid line) is presented as the benchmark.

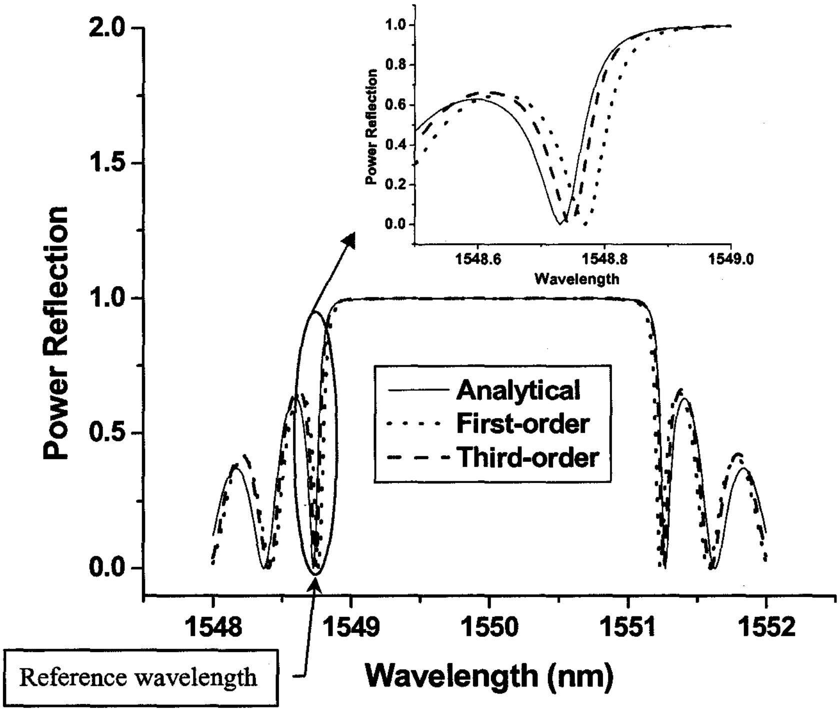

Figure 3.1 Comparison of the power reflectivity among the exact analytical solution, the 1st-order SS-TDM and the 3rd-order SS-TDM

It is observed from Figure 3.1 that, although all three methods appear to yield the same results for the power reflectivity in the stop-band, noticeable difference among the different methods is observed for the edges of the stop-band as well as for the side lobes. To illustrate this point, we investigated the zero-reflection wavelengths in the reflection spectrum shown in Figure 3.1 as a function of number of subsections. The wavelength deviation versus the number of total subsections is plotted in Figure 3.2. It is observed that the locus of the zero-reflection indicated by the arrow is converged to the analytical solution at different number of subsections *M* for the different method. For instance, convergence is realized at *M*=120 for the first-order SS-TDM and *M*=60 for the third-order SS-TDM, respectively. Hence, only half of the number of subsections is needed to achieve the same level of accuracy by the high-order scheme in comparison with the first-order one.

Further, we calculate the percentage error of the power reflection and show the results in Figure 3.3. The percentage error of the power reflection is defined as $\left(\sqrt{\sum_{\lambda_i}\left|\hat{\mathbf{R}}(\lambda_i)-\tilde{\mathbf{R}}(\lambda_i)\right|^2}\Big/\sqrt{\sum_{\lambda_i}\left|\tilde{\mathbf{R}}(\lambda_i)\right|^2}\right)\times 100\%$, where $\lambda_i \in (1548, 1552)nm$, $\hat{\mathbf{R}}(\lambda_i)$ denotes the power reflection of the distributed Bragg reflector at different wavelength calculated by the numerical solution whereas $\tilde{\mathbf{R}}(\lambda_i)$ denotes the power reflection obtained by the analytical formula in [80].

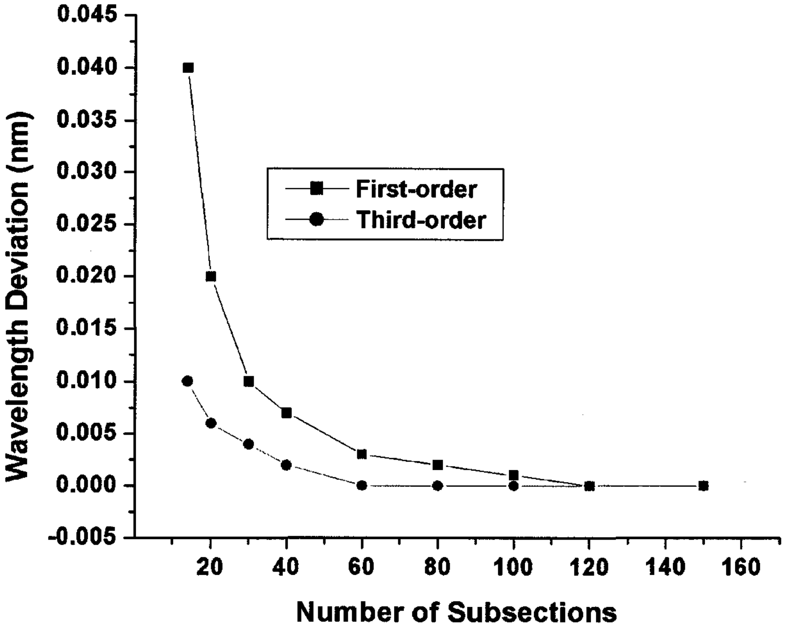

Figure 3.2 Wavelength deviation from the analytical solution for the locus of the zero-reflection wavelength indicated in Figure 3.1

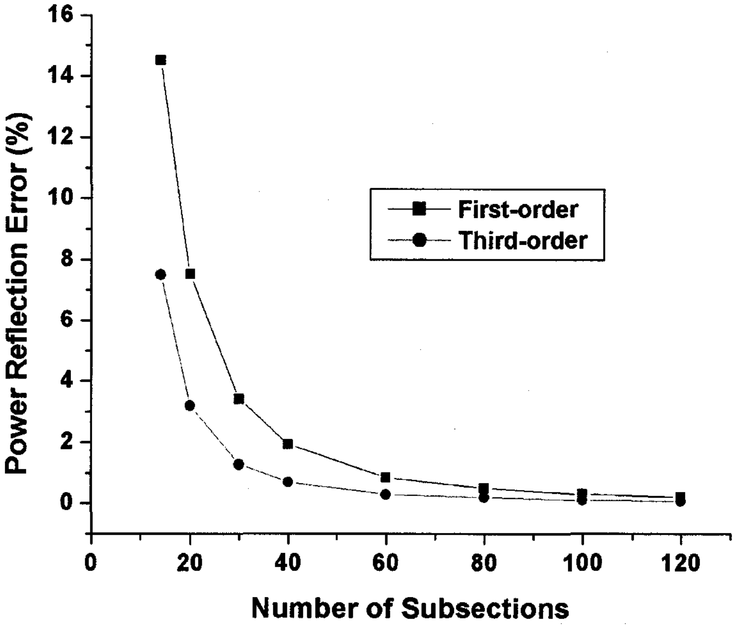

Figure 3.3 The error of the power reflectivity as a function of the number of subsections for the 1st-order and 3rd-order SS-TDM

B. Distributed Feedback (DFB) Lasers

In this section, the index-coupled, in-phase and anti-phase complex-coupled DFB lasers are examined to demonstrate the accuracy and efficiency of the high-order split-step scheme. The basic parameters used in our simulation are listed in Table 3.1. The injection current is 100mA. Both of the facets are AR-coated.

Parameters	**values**
Grating period Λ (nm)	244
Bragg order	1
Active region width w (μm)	1.5
Active layer thickness d (μm)	0.2
Laser length L (μm)	500
Confinement factor Γ	0.1
Effective index without injection n_{eff0}	3.2
Group index n_g	4
Internal loss α (cm^{-1})	20
Differential gain g_N (10^{-16} cm^2)	7
Transparent carrier density N_0 (10^{18} cm^{-3})	1.8
Nonlinear gain saturation coefficient ε (10^{-17} cm^3)	0
Carrier dependence of index dn/dN (10^{-20} cm^3)	-4.371
Linear recombination coefficient A (10^9 s^{-1})	1
Bimolecular radiation coefficient B (10^{-10} cm^3 s^{-1})	1
Auger coefficient C (10^{-29} cm^6 s^{-1})	0
Spontaneous emission coefficient β	10^{-4}
Petermann factor (K)	1

Table 3.1 DFB laser parameters used in the simulation

Figure 3.4 shows the normalized output power versus the number of subsections for the index-coupled DFB laser with $|\kappa L| = 3$. The output power calculated from the case where the subsection number is 1000 is taken as the benchmark solution. It is observed that, the third-order scheme converges faster to the benchmark solution than the conventional first-order scheme.

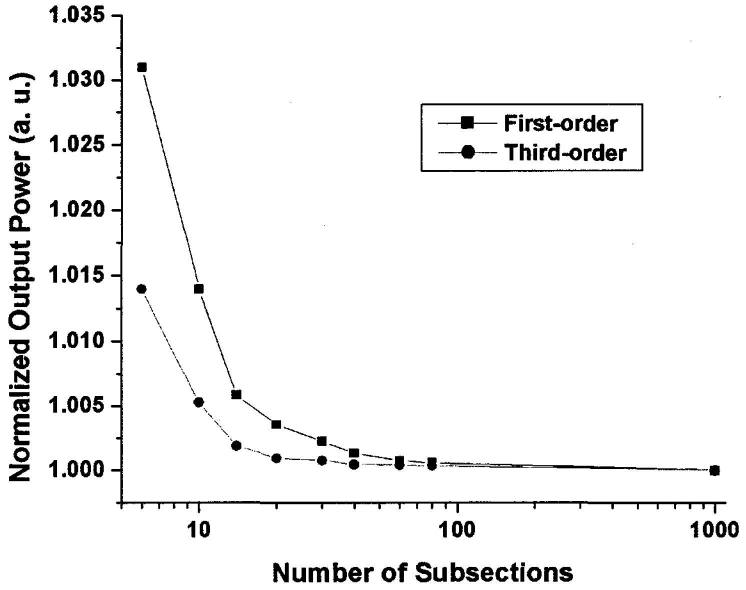

Figure 3.4 Comparison of the normalized output power under different number of subsections for the index-coupled DFB laser

We have also simulated the in-phase and the anti-phase complex-coupled DFB lasers with $|\kappa L| = 4$ and shown the results in Figure 3.5(a), (b), respectively. The gain coupling ratio is approximately 23%. The change of the photon distribution along the laser cavity with the increase of the total number of subsections is also plotted in Figure 3.6 for the anti-phase complex-coupled DFB laser. It can be seen that the photon distribution only deviates from its actual value slightly for the third-order scheme even at a very small number of subsections.

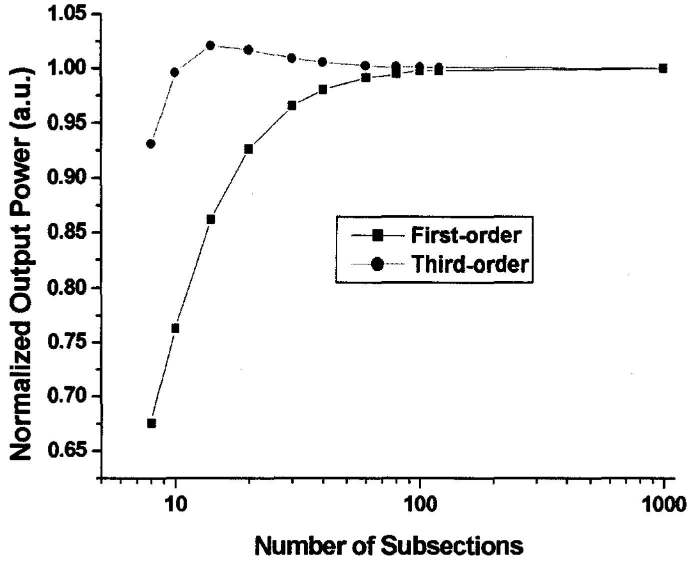

(a)

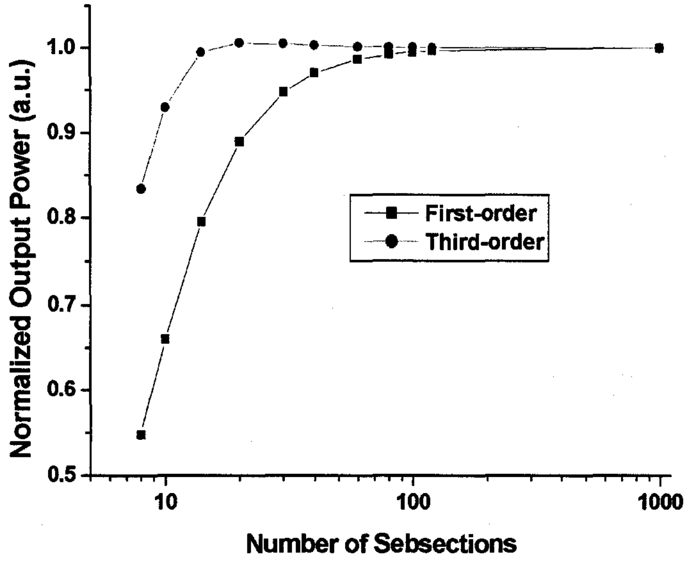

(b)

Figure 3.5 Comparison of the optical output powers between the 1st-order and 3rd-order SS-TDM for (a) in-phase complex-coupled DFB lasers (b) anti-phase complex-coupled DFB lasers

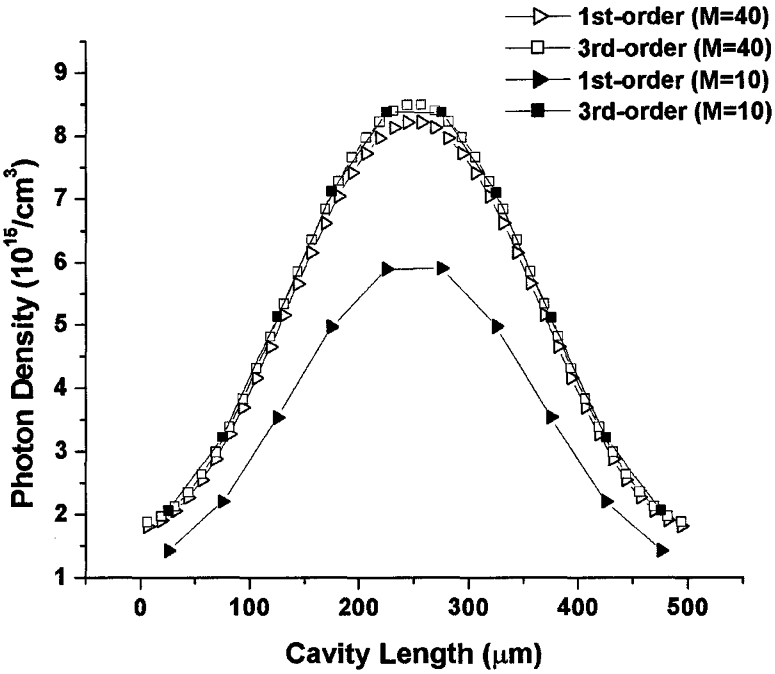

Figure 3.6 Photon density distributions along the laser cavity calculated by different schemes with different number of subsections *M*

From simulation results, we can draw such a conclusion that, in terms of convergence, the third order scheme has a better performance than the conventional SS-TDM. This is attributed to the fact that less error is introduced when splitting the exponential operator.

3.5 Comparison of the Computation Efficiency

In the last section, we have demonstrated the superiority of the high-order split-step scheme over the conventional scheme in terms of its faster convergence to benchmark results with the change of the space discretization size along the laser cavity. We will then examine their computation efficiencies in this section.

For the optical field to propagate one space/time step forward, the computation time taken by the high-order scheme is obviously longer than that of the conventional one, due to the reason that more divided operators have to be calculated for high-order scheme within each step. This is illustrated in Figure 3.7, where we compared the computation time taken by these two schemes with the given spatial mesh size. The computation time is obtained as that required for simulating the anti-phase complex-coupled DFB laser during a 5ns real time frame.

However, despite the fact that the computation time required for the third-order SS-TDM is more than that of the first-order scheme, it is found that the same level of accuracy can be achieved by the third-order SS-TDM with much smaller number of subsections. In this sense, the efficiency of the third-order scheme is in fact higher than the conventional scheme. Shown in Figure 3.8 is an example where the normalized output power and the computation time are plotted in the same figure for comparison. It can be seen that only 40 subsections are required for the third-order scheme (indicated as point A), while 80 for the conventional first-order scheme (indicated as point B) to achieve the output power within the error of about 0.5%. Obviously, the computation time for the third-order split-step scheme is less than 1/3 needed for the conventional split-step scheme. This can be seen more clearly in Figure 3.9 where the change of the computation time for different schemes with the error of output power is shown. The amount of time which can be saved by using the high-order scheme varies with the different device structures and also with the errors the users can accommodate.

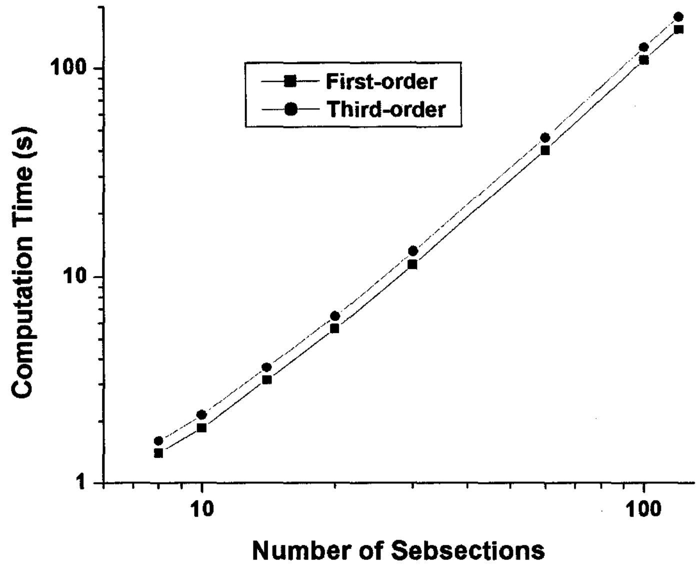

Figure 3.7 Comparison of the computation time between the 1st-order and 3rd-order SS-TDM for the anti-phase complex-coupled DFB laser

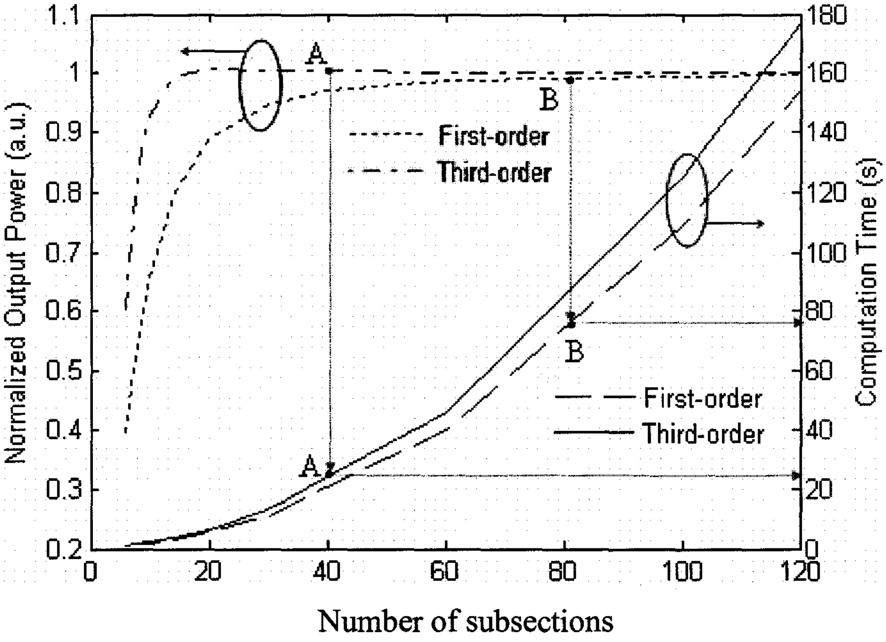

Figure 3.8 Comparison of the output power and the computation time between the 1st-order and 3rd-order SS-TDM for the anti-phase complex-coupled DFB laser

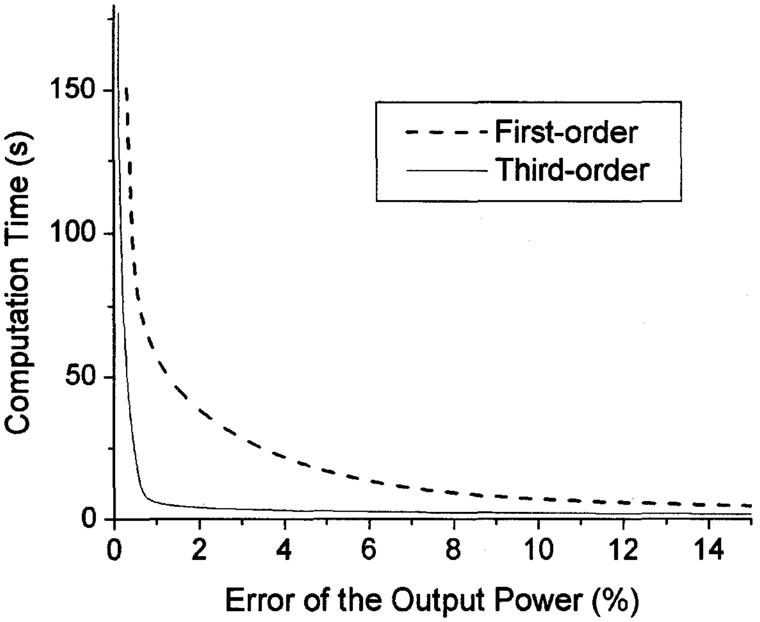

Figure 3.9 Computation time versus error of the output power for the 1st-order and 3rd-order SS-TDM

3.6 Summary

In this chapter, a high-order split-step algorithm is developed to solve the time-dependent coupled-wave equations for the optical field in a variety of grating-based optical devices such as DFB lasers. Simulation results show that the proposed high-order scheme converges faster to benchmark results with the increase of the number of subsections than the conventional split-step method, which implies that a larger spatial mesh size can be used to achieve the same accuracy as that of the conventional SS-TDM. Significant improvement on the computation efficiency of the conventional split-step scheme has been observed. As a result, it will find its promising applications on system modeling and optimization where computation time is of concern.

Chapter 4

Standing Wave Model based on "Cold" Cavity Modes

4.1 Introduction

The traveling wave model solves the time-dependent coupled-wave equations directly without making any assumption about the resonance conditions and therefore is valid even if the laser cavity has a small Q-factor. For resonating laser structures with large variations of the carrier/photon density, however, the traveling-wave approach is not computationally economical. This is because that LSHB effects force us to use very fine mesh in space to catch large non-uniformity of the carrier/photon distribution, therefore unnecessary small time step has to be applied to ensure the stability of the algorithm. The standing wave model, on the other hand, assumes there exist a set of resonating spatial modes in the laser cavity, which in general represent all possible natural oscillations of the optical field in a resonator. The optical field is then decomposed into these modes. As such, it concerns only with the temporal evolution of the amplitudes of these modes and reduces the traveling-wave partial differential equations to a set of ordinary differential equations.

The existing standing wave models are all based on resonance modes of the cavity under different bias (i.e., modes under "floating" bias) [66]-[68], which means that, if the injection current is time-dependent, all the resonance modes have to be solved for multiple times accordingly. This is not computational efficient. Moreover, in practice, the calculation of these bias-dependent "hot" cavity modes is by no means an easy task as it frequently involves searching for multiple potential lasing modes in the complex domain. Missing the potential lasing mode might happen when mode hopping happens.

In this chapter, a time-domain standing-wave model based on "cold" cavity modes expansion (SWM-CCM), i.e. modes of the laser cavity without any injection, is proposed and developed. These "cold" cavity modes are able to capture the structural features of the laser cavities (e.g., the grating profiles, phase shifts, facet conditions, etc.) and are computed only once, independent of pumping conditions. The optical fields are then expanded in terms of these modes. Two types of widely used DFB lasers, uniform-grating DFB lasers and $\lambda/4$-shifted DFB lasers are simulated by using the presented approach. The simulation results are compared with the well-established traveling wave model.

4.2 Eigen-Solutions of the "Cold" Cavity Modes

By using the matrix notation, the time-dependent coupled wave equations (2.9) and (2.10) can be rearranged as

$$\frac{\partial \psi}{\partial t} = \mathbf{H}_t \psi + \tilde{\mathbf{s}}_t \tag{4.1}$$

with $\tilde{\mathbf{s}}_t = \upsilon_g \tilde{\mathbf{s}}$ and the matrix operator

$$\mathbf{H}_t = \upsilon_g \begin{bmatrix} \Gamma g(1+j\alpha_m)/2 - \alpha_i/2 - \partial/\partial z & j\kappa \\ j\kappa & \Gamma g(1+j\alpha_m)/2 - \alpha_i/2 + \partial/\partial z \end{bmatrix}. \tag{4.2}$$

The operator $\mathbf{H}_t$ in (4.2) can always be split into two parts with one corresponding to "cold" cavity, the other the bias current, i.e.

$$\mathbf{H}_t = \mathbf{H}^0 + \mathbf{H}^I \tag{4.3}$$

where the superscript "0" denotes the value associated with cold cavity and the superscript "**I**" denotes the value which is injection current dependent. For instance, the two operators in Eq. (4.3) will take the form of

$$\mathbf{H}^0 = \upsilon_g \begin{bmatrix} -\alpha_i/2 - \partial/\partial z & j\kappa \\ j\kappa & -\alpha_i/2 + \partial/\partial z \end{bmatrix}, \tag{4.4}$$

$$\mathbf{H}^I = \upsilon_g \begin{bmatrix} \Gamma g(1+j\alpha_m)/2 & 0 \\ 0 & \Gamma g(1+j\alpha_m)/2 \end{bmatrix}. \tag{4.5}$$

Mathematically speaking, the "cold" cavity modes are actually the eigenfunctions and eigenvalues of the evolution operator $\mathbf{H}^0$. Consider the eigenvalue problem as follows

$$\mathbf{H}^0 \mathbf{\Phi}_n^0 = \xi_n^0 \mathbf{\Phi}_n^0 \tag{4.6}$$

where $\mathbf{\Phi}_n^0 = \begin{bmatrix} \phi_f^0(z) \\ \phi_r^0(z) \end{bmatrix}_n$ are eigenfunctions of the operator $\mathbf{H}^0$ with eigenvalues ξ_n^0.

Generally, the eigenvalues ξ_n^0 are complex numbers with the real part characterizing the mode decaying rate and the imaginary part presenting the shift of the resonance frequency from the reference frequency. The eigenfunctions give the characteristic field patterns that the cavity structure can support. Under the facet conditions of

$$\phi_f^0(0) = r_1\phi_r^0(0),\ \ \phi_r^0(L) = r_2\phi_f^0(L), \tag{4.7}$$

the eigenvalues ξ_n^0 and eigenfunctions $\mathbf{\Phi}_n^0$ of the cold cavity operator $\mathbf{H}^0$ can be calculated by using the transfer matrix method (TMM) [81], [82] as follows:

Considering a most general scenario that all the parameters in the evolution matrix are z-dependent, Eq. (4.6) can be written as

$$\frac{d}{dz}\begin{bmatrix}\phi_f^0(z)\\ \phi_r^0(z)\end{bmatrix}_n = \begin{bmatrix}X_n(z) & j\kappa(z)\\ -j\kappa(z) & -X_n(z)\end{bmatrix}\begin{bmatrix}\phi_f^0(z)\\ \phi_r^0(z)\end{bmatrix}_n. \tag{4.8}$$

with $X_n = -\xi_n^0/\upsilon_g - \alpha_i/2$. The continuous functions $\phi_{f,r}^0(z)$ are approximated by their discrete analogue on the section-wise uniform spatial meshes. The numerical solution to Eq. (4.8) for each subsection is given by

$$\begin{aligned}\begin{bmatrix}\phi_f^0(z_m+\Delta z)\\ \phi_r^0(z_m+\Delta z)\end{bmatrix}_n &= \begin{bmatrix}\cosh\gamma_n\Delta z + \frac{X_n}{\gamma_n}\sinh\gamma_n\Delta z & \frac{j\kappa}{\gamma_n}\sinh\gamma_n\Delta z\\ -\frac{j\kappa}{\gamma_n}\sinh\gamma_n\Delta z & \cosh\gamma_n\Delta z - \frac{X_n}{\gamma_n}\sinh\gamma_n\Delta z\end{bmatrix}\begin{bmatrix}\phi_f^0(z_m)\\ \phi_r^0(z_m)\end{bmatrix}_n \\ &\triangleq \mathbf{T}_m\big|_n \cdot \begin{bmatrix}\phi_f^0(z)\\ \phi_r^0(z)\end{bmatrix}_n\end{aligned} \tag{4.9}$$

with $\gamma_n^2 = X_n^2 + \kappa^2$. Notice that the subscript n is the index of the eigenmode and m denotes the mth subsection along the cavity.

1) Eigenvalues

Assume that the device is divided into M *sub*sections. The fields at the two ends of the device can then be linked through cascading the transfer matrix **T** as

$$\begin{aligned}\begin{bmatrix}\phi_f^0(L)\\ \phi_r^0(L)\end{bmatrix}_n &= \prod_{m=M}^{1}\mathbf{T}_m\Big|_n\begin{bmatrix}\phi_f^0(0)\\ \phi_r^0(0)\end{bmatrix}_n \\ &\triangleq \begin{bmatrix}T_{11} & T_{12}\\ T_{21} & T_{22}\end{bmatrix}_n\begin{bmatrix}\phi_f^0(0)\\ \phi_r^0(0)\end{bmatrix}_n\end{aligned} \qquad (4.10)$$

By applying the boundary conditions of Eq. (4.7), the characteristic equation where the eigenvalues are embedded is obtained by

$$r_1r_2T_{11} + r_2T_{12} - r_1T_{12} - T_{22} = 0. \qquad (4.11)$$

For the uniform-grating DFB laser, the coupling coefficient is uniform along z, we may readily derive that the complex eigenvalues ξ_n^0 are the solution of the following transcendental equation

$$\gamma_n(r_1r_2-1)\cosh\gamma_nL - \left[(r_1r_2+1)\left(\xi_n^0/\upsilon_g+\alpha_i/2\right) - j(r_1+r_2)\kappa\right]\sinh\gamma_nL = 0 \qquad (4.12)$$

For the $\lambda/4$-shifted DFB laser, the laser cavity can be viewed as the cascade of two uniform DFB lasers with two coupling coefficients of opposite phase, i.e. the grating has a phase change of π at the center of the cavity length ($\theta = \pi$ in Eq. (2.3)), which is illustrated in Figure 4.1. The complex eigenvalues ξ_n^0 are the solution of the transcendental equation

$$\begin{aligned}&\frac{(r_1r_2-1)\left(\xi_n^0/v_g+\alpha_i/2\right)^2 - j\kappa\left(\xi_n^0/v_g+\alpha_i/2\right)(r_2-r_1)}{\gamma_n^2}\cosh\gamma_nL - \frac{(r_1r_2+1)\left(\xi_n^0/v_g+\alpha_i/2\right)}{\gamma_n}\sinh\gamma_nL\\ &+\frac{(r_1r_2-1)\kappa^2 + j\kappa\left(\xi_n^0/v_g+\alpha_i/2\right)(r_2-r_1)}{\gamma_n^2} = 0\end{aligned} \qquad (4.13)$$

In searching the complex eigenvalues of the characteristic equations, a complex variable root searching routine is used.

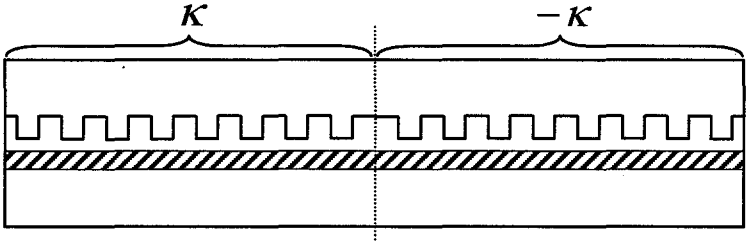

Figure 4.1 Schematic view of $\lambda/4$ -shifted DFB lasers

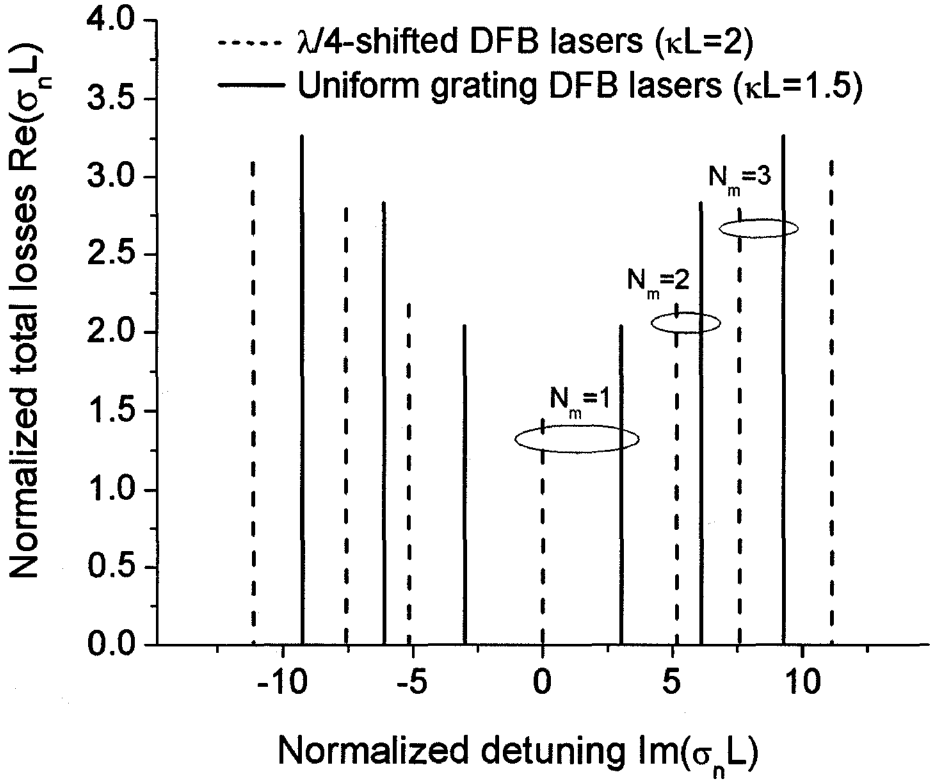

Figure 4.2 Mode spectrum for the uniform-grating and $\lambda/4$ -shifted DFB lasers with AR-coated facets

As discussed earlier the real part of the eigenvalue of the "cold" cavity operator, i.e. $\mathrm{Re}\left(\xi_n^0\right)$, is the decay rate of each cavity mode and the imaginary part $\mathrm{Im}\left(\xi_n^0\right)$ is the associated frequency of the decay. In other words, if we define

$$\sigma_n = -\xi_n^0 / \upsilon_g , \tag{4.14}$$

it is straightforward to show that $\mathrm{Re}\left(\sigma_n\right)$ actually bears the physical meaning of the total optical field losses for the *n*th longitudinal cavity mode and $\mathrm{Im}\left(\sigma_n\right)$ represents the detuning of the propagation constant from the Bragg condition for the associated mode. Figure 4.2 shows the mode spectrum with the normalized characteristic total losses for the uniform-grating and the $\lambda/4$-shifted DFB laser with AR-coated facets, respectively.

We may notice that the total optical field losses $\mathrm{Re}\left(\sigma_{\mathrm{n}}\right)$ can be defined as

$$\mathrm{Re}\left(\sigma_{\mathrm{n}}\right) = \frac{1}{2}\left(\alpha_i + \alpha_{cav,n}\right) \tag{4.15}$$

where the internal optical power loss α_i represents the optical scattering and absorptions; the cavity loss of the *n*th mode $\alpha_{cav,n}$ accounts for the power leaving the DFB laser cavity which solely depends on the cavity structure such as cavity length, coupling coefficient and facet reflectivity. It is known that the cavity loss of a Fabry-Perot-type laser has the analytical solution given by $\frac{1}{L}\ln\left(\frac{1}{r_1 r_2}\right)$, which is also known as the mirror loss. However for the DFB laser, $\alpha_{cav,n}$ may have to be obtained from numerical calculations. As a result, it is practically meaningful to study the dependence of the cavity loss on the structure parameters. A comprehensive study on this topic can be found in [83], [84].

2) Eigenfunctions

Once the eigenvalues are obtained, the eigenfunction can be constructed through the transfer matrix from the left facet z=0 to arbitrary position $z \in [0, L]$ with incorporating of the boundary condition, i.e.

$$\begin{bmatrix} \phi_f^0(z_m) \\ \phi_r^0(z_m) \end{bmatrix}_n = \prod_{x=m}^{1} \mathbf{T}_x\Big|_n \begin{bmatrix} r_1 \\ 1 \end{bmatrix}_n \tag{4.16}$$

Again, for the uniform DFB laser, the analytical solution of the eigenfunctions of the operator $\mathbf{H}^0$ can be derived as

$$\begin{bmatrix} \phi_f^0(z) \\ \phi_r^0(z) \end{bmatrix}_n = \begin{bmatrix} r_1 \cosh\gamma_n z + \dfrac{r_1 X_n + j\kappa}{\gamma_n} \sinh\gamma_n z \\ \cosh\gamma_n z + \dfrac{-j\kappa r_1 - X_n}{\gamma_n} \sinh\gamma_n z \end{bmatrix} \tag{4.17}$$

and the eigenfunctions for the $\lambda/4$ -shifted DFB laser take the form of

$$\mathbf{\Phi}_n^0 = \begin{bmatrix} \phi_f^0 \\ \phi_r^0 \end{bmatrix}_n =$$

$$\begin{cases} \begin{bmatrix} r_1 \cosh\gamma_n z + \dfrac{r_1 X_n + j\kappa}{\gamma_n} \sinh\gamma_n z \\ \cosh\gamma_n z - \dfrac{j\kappa r_1 + X_n}{\gamma_n} \sinh\gamma_n z \end{bmatrix} & 0 \le z < L/2 \\ \begin{bmatrix} \dfrac{X_n(r_1 X_n + j\kappa)}{\gamma_n^2} \cosh\gamma_n z + \dfrac{\kappa(r_1\kappa - jX_n)}{\gamma_n^2} \cosh\gamma_n(L-z) + \dfrac{r_1 X_n}{\gamma_n} \sinh\gamma_n z + \dfrac{j\kappa}{\gamma_n} \sinh\gamma_n(L-z) \\ \dfrac{X_n(X_n + j\kappa r_1)}{\gamma_n^2} \cosh\gamma_n z + \dfrac{\kappa(\kappa - jr_1 X_n)}{\gamma_n^2} \cosh\gamma_n(L-z) - \dfrac{X_n}{\gamma_n} \sinh\gamma_n z - \dfrac{j\kappa r_1}{\gamma_n} \sinh\gamma_n(L-z) \end{bmatrix} & L/2 \le z \le L \end{cases} \tag{4.18}$$

Shown in Figure 4.3 (a), (b) are illustrations of spatial intensity distributions of the first three modes for the uniform-grating DFB laser, and the $\lambda/4$ -shifted DFB laser, respectively.

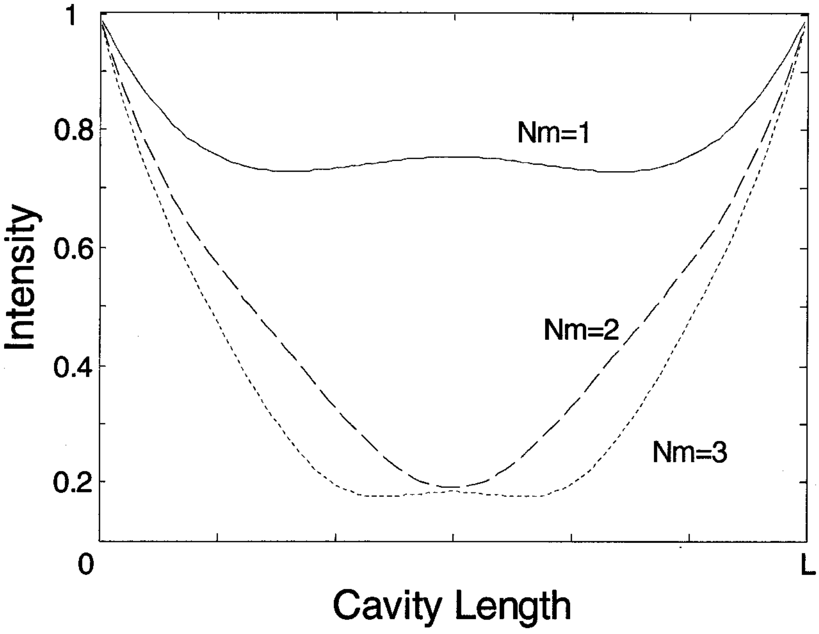

(a)

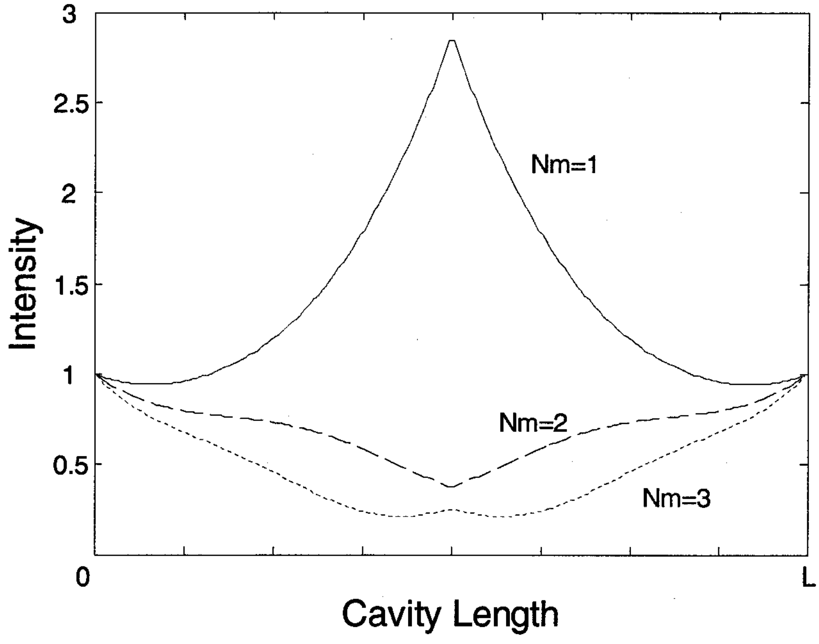

(b)

Figure 4.3 Spatial intensity distributions of the first three modes for the (a) uniform-grating DFB laser $\kappa L = 1.5$ and (b) $\lambda/4$-shifted DFB laser with $\kappa L = 2$

4.3 Bi-Orthogonality of the Longitudinal Eigenmodes of a Laser

An important issue for the mode expansion method is the orthogonality relationship among the eigenmodes. Siegman [85] discussed this issue for the transverse eigenmodes of an open laser resonator and pointed out that the eigenmodes in the open cavity laser system are in general not self-adjoint and hence not power-orthogonal. His work was then extended in [86] to the longitudinal eigenmodes of a laser, which are also not power-orthogonal. This is caused by the non-Hermitian nature of the problem: energy is not conserved in the laser cavity with lossy mirrors. However, this problem can be solved by introducing a set of adjoint eigenmodes $\mathbf{w}_m(z)$ which are the eigenmodes of the adjoint system. Physically, the fields in the adjoint system are propagating in the reverse direction along the original system although these two systems share the same eigenvalues [85].

The schematic representation of the original laser system and its adjoint system is shown in Figure 4.4. The solid line denotes the wave propagating in the original system; the dashed line represents the wave in the adjoint system; and the arrow indicates the direction of the propagation. In reality, the wave is propagating back and forth inside the laser cavity. However, we may actually continuously "unfold" the laser so that the wave is equivalently propagating uni-directionally along the z axis as shown in step I. It is seen that the waveform has a period of $2L$ due to the oscillation condition of the laser cavity, i.e. the round trip gain is unity. As such, we may study one period of the structure as shown in step II, where the counter traveling wave of the same system is depicted. This left propagating wave actually is the wave in the adjoint system. Finally, the structure in step II is folded back to the real laser cavity so that the original system and adjoint system can be established as shown in step III.

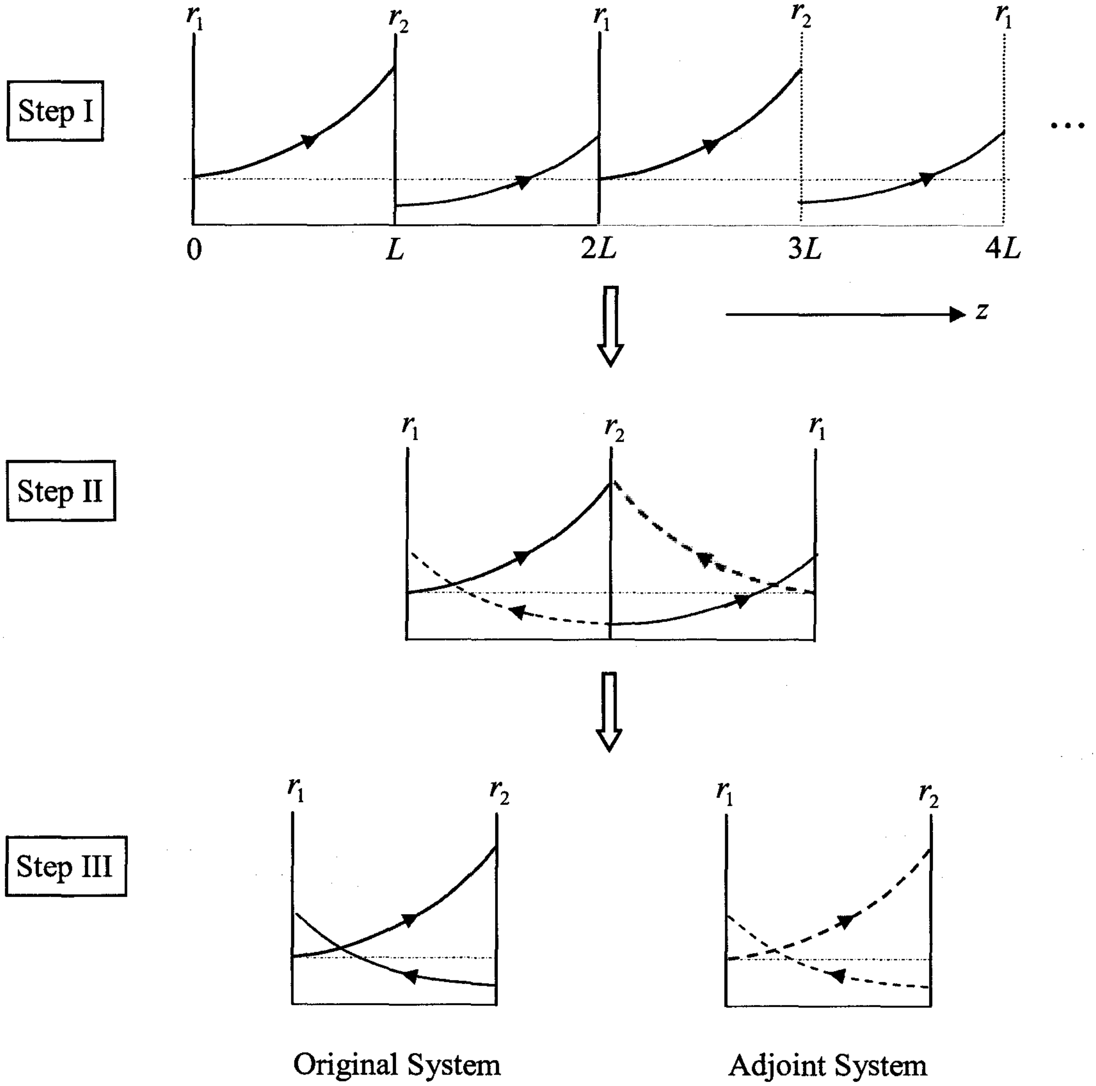

Figure 4.4 Schematic representation of the original laser system and its adjoint system

As a result, by exchanging the two components of the vector $\mathbf{\Phi}_n^0$, a set of adjoint eigenmodes $\mathbf{w}_m(z)$ can be obtained. It can be verified that these adjoint eigenmodes are biorthogonal to the original eigenmodes $\bar{\mathbf{\Phi}}_n^0(z)$ such that

$$\int_0^L \bar{\mathbf{\Phi}}_n^0(z)\cdot\mathbf{w}_m(z)dz=\delta_{nm} \tag{4.19}$$

where

$$\mathbf{w}_m=c'_m\begin{bmatrix}\phi_r^0\\ \phi_f^0\end{bmatrix}_m, \tag{4.20}$$

and the normalized "cold" cavity modes $\bar{\mathbf{\Phi}}_n^0(z)$ is defined as

$$\bar{\mathbf{\Phi}}_n^0(z)=c_n\mathbf{\Phi}_n^0(z) \tag{4.21}$$

with the normalization constant c_n described by

$$|c_n|^2=\frac{1}{\int_0^L\left|\mathbf{\Phi}_n^0(z)\right|^2dz}. \tag{4.22}$$

As a last remark, we notice that the gain medium has a finite bandwidth so that the number of modes that the medium can interact with is finite. It is found that the set $\{\mathbf{\Phi}_n^0\}$ is complete for a finite-dimensional state space [87].

4.4 Multimode Photon Wave Equations Based on "Cold" Cavity Modes

After obtaining the eigenfunctions and eigenvalues of the "cold" cavity operator, the total field ψ can then be expanded in terms of $\bar{\mathbf{\Phi}}_n^0(z)$ in the form of

$$\psi = \sum_{n=1}^{K} A_n(t)\bar{\mathbf{\Phi}}_n^0(z) \tag{4.23}$$

where $A_n(t)$ is the complex amplitude for each cavity mode and K is the number of modes used in the expansion.

If we substitute Eq. (4.23) into Eq. (4.1), multiply both sides by any adjoint eigenmodes $\mathbf{w}_m(z)$ and integrate over the cavity length, the original equation separates into a set of equations for the complex amplitude of each longitudinal mode in the form of

$$\frac{dA_m(t)}{dt} = p_{mm}A_m(t) + \sum_{n=1(n\neq m)}^{K} p_{mn}A_n(t) + \tilde{\eta}_m(t) \tag{4.24}$$

with

$$p_{mm} = \xi_m^0 + \int_0^L \mathbf{w}_m(z)\cdot\mathbf{H}^{\mathrm{I}}\bar{\mathbf{\Phi}}_m^0(z)dz\,, \tag{4.25}$$

$$p_{mn} = \int_0^L \mathbf{w}_m(z)\cdot\mathbf{H}^{\mathrm{I}}\bar{\mathbf{\Phi}}_n^0(z)dz \tag{4.26}$$

and the Langevin noise term that drives the amplitude of each mode is given by

$$\tilde{\eta}_m(t) = \int_0^L \tilde{\mathbf{s}}_t(z,t)\cdot\mathbf{w}_m(z)dz\,. \tag{4.27}$$

Since the original noise term $\tilde{s}_{f,r}(z,t)$ in Eq. (2.11) is a Dirac delta function correlated both in time and space coordinates, we can perform the longitudinal integrations and approximate the noise $\tilde{\eta}_m$ as Gaussian random processes with zero mean and satisfying following correlation relation

$$\left\langle \tilde{\eta}_m(t)\tilde{\eta}_m^*(t')\right\rangle = \Gamma\beta K_{tr}K_{mz}R_{sp}L\delta(t-t') \tag{4.28}$$

where K_{mz} is the longitudinal Petermann's factor or the longitudinal excess-noise factor for mth longitudinal mode given by [86]

$$K_{mz} = \int_0^L \mathbf{w}_m^*(z)\mathbf{w}_m(z)dz \tag{4.29}$$

Finally, the original PDEs are reduced to a set of coupled ODEs in the form of Eq. (4.24). The eigen equation (4.6) with boundary conditions for a given laser structure determine the eigenmodes of the cold cavity, whereas a set of temporal equations describe explicitly time-dependent amplitudes of these eigenmodes.

The carrier rate equation (2.18) and the mode amplitude equation (4.24) are solved in a self-consistent manner in the time-domain under a given time-dependent bias, whereas Eq. (4.6) only needs to be solved for once under the facet conditions prior to the time marching process.

4.5 Model Validation and Applications

In this section the SWM-CCM is validated and applied to simulate two typical DFB lasers, i.e. the uniform-grating DFB laser and the $\lambda/4$-shifted DFB laser. The static and dynamic properties are investigated and compared with the well-established traveling wave method. The solid line in all of the figures represents results calculated by the TWM (the SS-TDM implemented in Chapter 2), while others by the SWM-CCM.

4.5.1 Uniform-Grating Index-Coupled DFB lasers

The uniform-grating DFB laser with $\kappa L = 1.5$ is firstly investigated for model validation. The modeling parameters are listed in Table 4.1 [59]. For this device, good agreement between the SWM-CCM and the TWM has been achieved by only using two eigenmodes in the field expansion in the proposed SWM-CCM.

Parameters	**values**
Grating period Λ (nm)	244.5
Bragg order	1
Active region volume V_a (μm^3)	90
Facet reflectivities r_1, r_2	0
Laser length L (μm)	300
Confinement factor Γ	0.3
Effective index without injection n_{eff0}	3.2
Group index n_g	3.6
Internal loss α (cm^{-1})	50
Differential gain g_N (10^{-16} cm^2)	2.5
Transparent carrier density N_0 (10^{18} cm^{-3})	1.0
Nonlinear gain saturation coefficient ε (10^{-17} cm^3)	6.0
Linewidth enhancement factor α_m	4
Linear recombination coefficient A (10^9 s^{-1})	0.1
Bimolecular radiation coefficient B (10^{-10} cm^3 s^{-1})	1
Auger coefficient C (10^{-29} cm^6 s^{-1})	7.5
Spontaneous emission coefficient β	5×10^{-5}
Transverse Petermann factor (K_{tr})	1

Table 4.1 Uniform-grating DFB laser parameters

1) Threshold Analysis

From the oscillation condition in the sense of "threshold gain=losses", we may readily obtain the threshold modal gain from the mode with the lowest loss $\mathrm{Re}(\sigma_{\min})$ by

$$\frac{\Gamma g_{th}}{2} = \mathrm{Re}(\sigma_{\min}). \tag{4.30}$$

As $g_{th} = g_N (N_{th} - N_0)$, we arrive at

$$N_{th} = \frac{2\,\mathrm{Re}(\sigma_{\min})}{\Gamma g_N} + N_0\ . \tag{4.31}$$

The required threshold current may be estimated from the Eq. (2.18) as

$$I^{th} = eV(AN_{th} + BN_{th}^2 + CN_{th}^3) \qquad (4.32)$$

From Eq. (4.31), (4.32) and Figure 4.2, the threshold current is estimated to be around 40mA in this example.

2) Static Characteristics

The static solutions are obtained by allowing the dynamic response of the laser to reach its steady state for a given bias current and then averaging the output power over a 0.5ns time interval. Figure 4.5 shows the light-current (LI) curve for this uniform DFB laser. Since the thermal effects are not considered in this model, the output power has an almost linear dependency on the injection current.

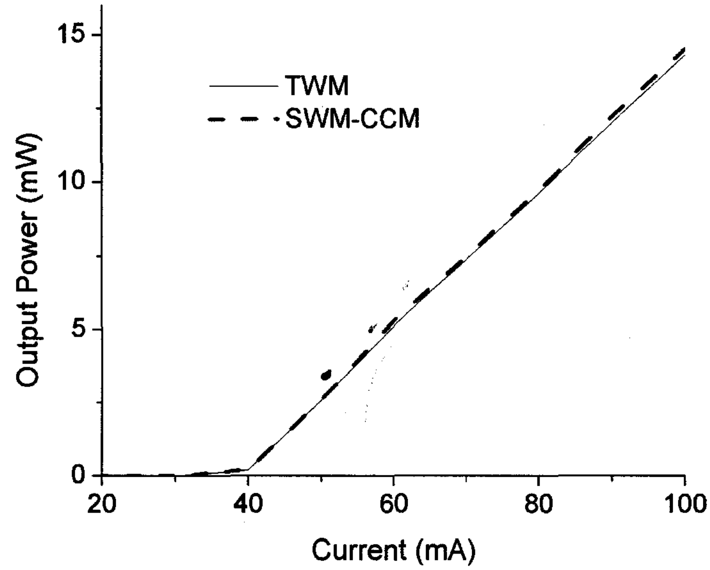

Figure 4.5 Comparison of LI characteristics for the uniform DFB laser with $\kappa L = 1.5$

Figure 4.6 (a) and (b) show the CW spatial distributions of the carrier and photon densities along the laser cavity, respectively.

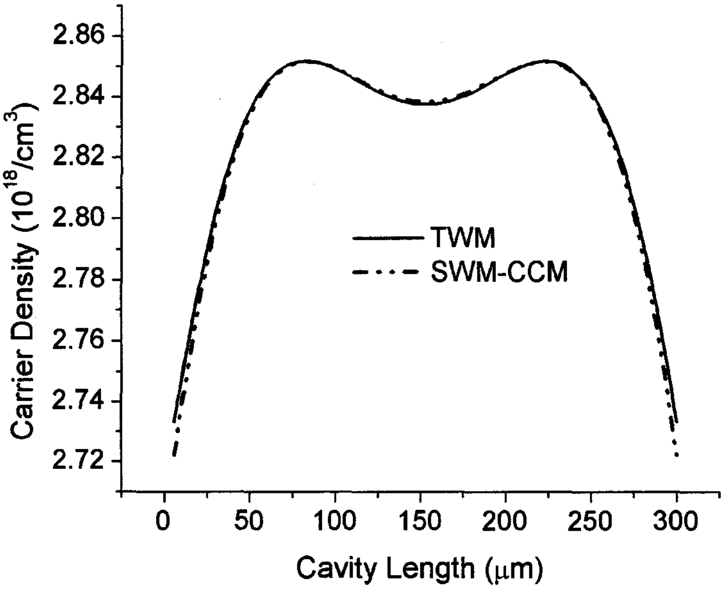

(a)

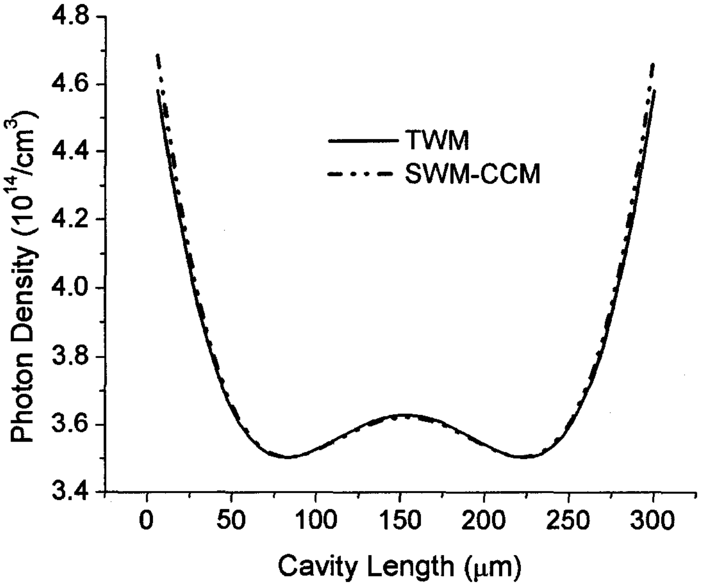

(b)

Figure 4.6 Comparison of the longitudinal distributions of (a) Carrier density; (b) Photon density

3) Small Signal Modulation

The amplitude modulation (AM) response has been calculated and shown in Figure 4.7 as a function of the frequency over a range of 10 GHz. The bias current is 80 mA, and the modulation depth is 5%.

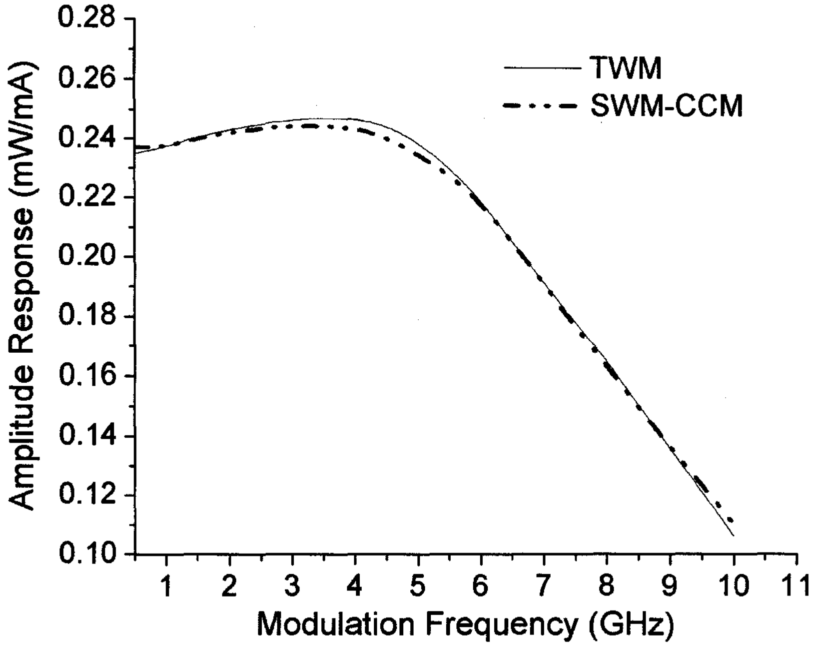

Figure 4.7 Comparison of the AM response of the laser under investigation

4) Large Signal Modulation

To examine the ability for the proposed model to simulate the large signal dynamics, we first let both models run for sufficiently long time under a 50 mA bias current to reach their respective steady state. And then the laser is modulated by a 0.5GHz square wave with the modulation magnitude equal to 20mA. Figure 4.8 shows the variation of the output power during the large signal modulation.

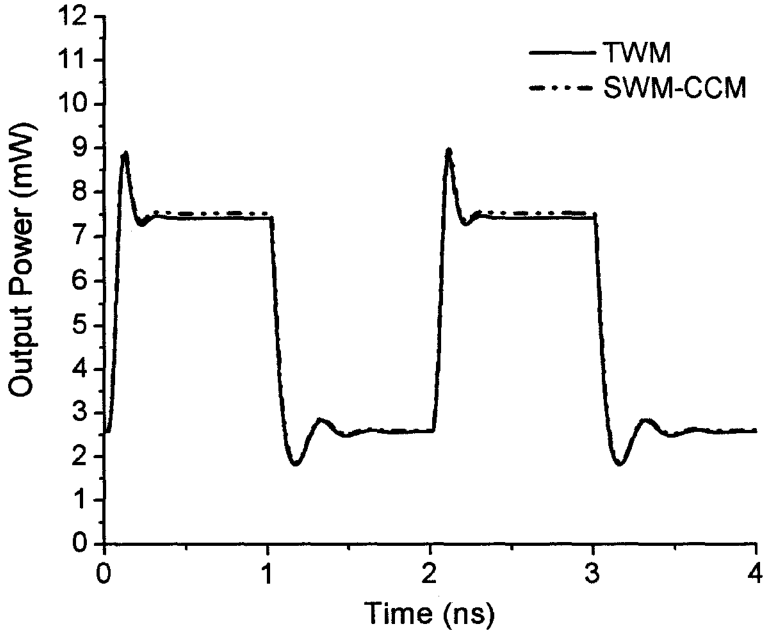

Figure 4.8 Comparison of the output power during the large signal modulation

4.5.2 Quarter-Wave-Shifted DFB Lasers

In this section, the device under investigation is a typical DFB laser with the λ/4-shifted grating. The modeling parameters are listed in Table 4.2 [88]. In this example, it is found that nine eigenmodes are needed in the field expansion for the SWM-CCM to achieve good agreement with results from the TWM within the entire range (0~200mA) of the injection level. The reason for the increasing number of expansion mode will be discussed in detail in next section.

Parameters	Values
Grating period Λ (nm)	244.5
Bragg order	1
Active region volume V (μm^3)	90
Facet reflectivities r_1, r_2	0
Laser length L (μm)	300
Confinement factor Γ	0.3
Effective index without injection n_{eff0}	3.4
Group index n_g	3.6
Internal loss α (cm^{-1})	50
Differential gain g_N (10^{-16} cm^2)	2.5
Transparent carrier density N_0 (10^{18} cm^{-3})	1.0
Carrier dependence of index dn/dN (10^{-20} cm^3)	-1.5
Linear recombination coefficient A (10^9 s^{-1})	0.1
Bimolecular radiation coefficient B (10^{-10} cm^3 s^{-1})	1
Auger coefficient C (10^{-29} cm^6 s^{-1})	7.5
Transverse Petermann factor (K_{tr})	1

Table 4.2 λ/4-shifted DFB laser parameters

Figure 4.9 shows the LI curve calculated by the SWM-CCM taking different number of eigenmodes in the field expansion of Eq. (4.23) and their comparisons with results from the TWM. Also shown is the published result from the COST240 group [88]. It is observed from Figure 4.9 that the proposed model can predict the laser performance very well even with one expansion mode if the injection level is low (less than 60mA in this example). However nine expansion modes are necessary if the injection level is further increasing, as is also seen from the comparisons of CW carrier and photon distributions along the laser cavity shown in Figure 4.10 (a), (b).

Figure 4.11 shows the laser response to the large signal modulation with the modulation magnitude of 30mA and modulation frequency of 2.5GHz. It is observed that the result of the SWM-CCM with nine expansion modes is fully overlapped with that of the TWM.

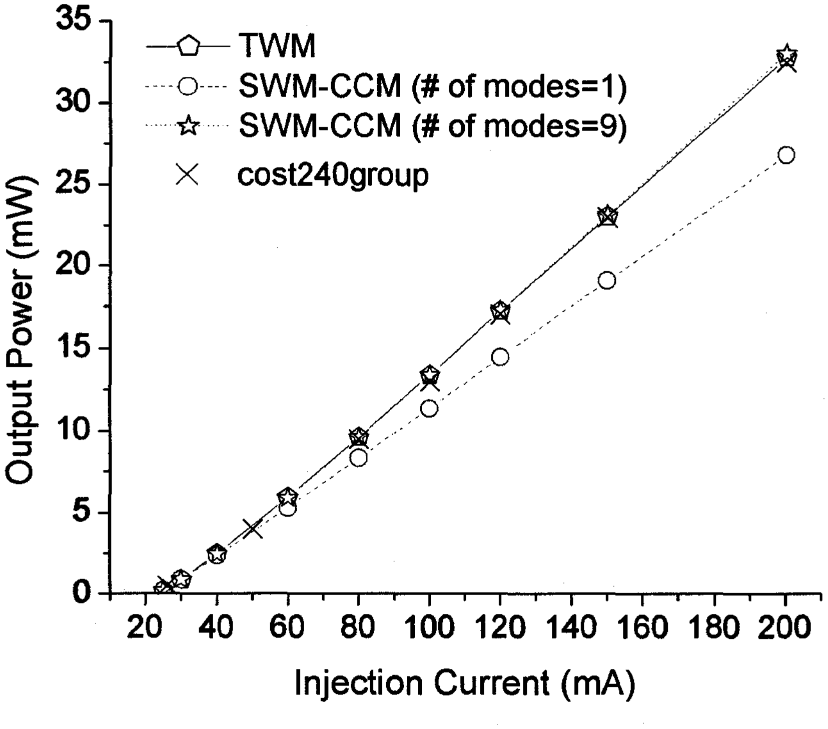

Figure 4.9 Comparison of LI characteristics for λ/4-shifted DFB lasers with $\kappa L = 2$

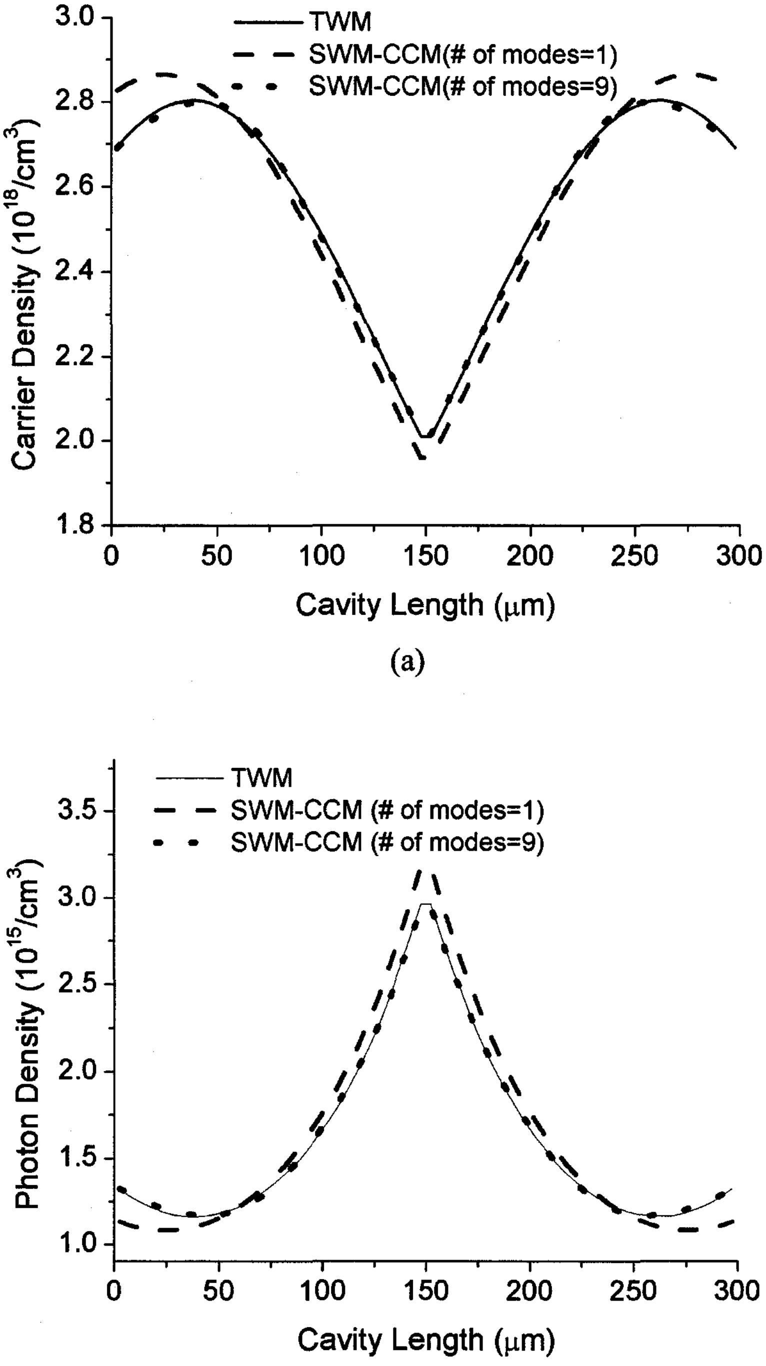

(a)

(b)

Figure 4.10 Comparison of (a) carrier density distribution (b) photon density distribution for the λ/4-shifted DFB laser with $\kappa L = 2$

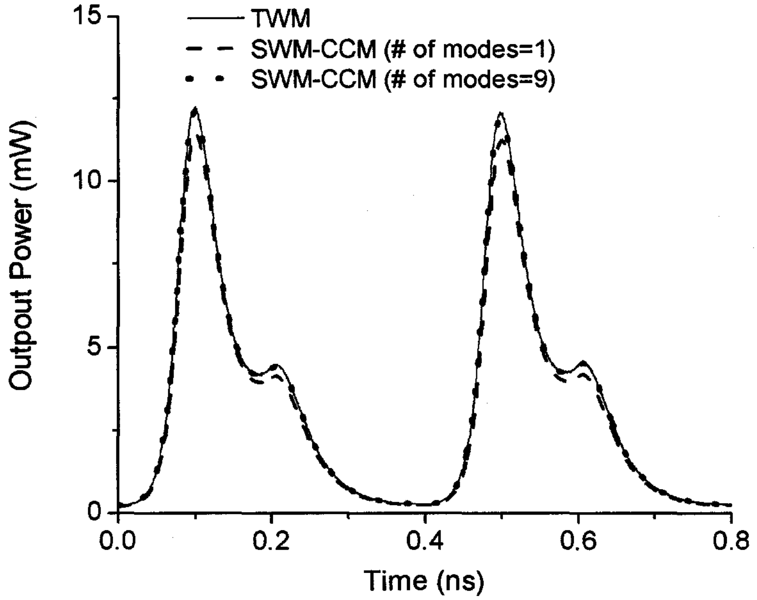

Figure 4.11 Large signal modulation response for the λ/4-shifted DFB laser with $\kappa L = 2$

4.6 Discussions

In this section, the impact of the expansion mode truncation on the model accuracy with varying DFB structure parameters is investigated. The computation efficiency of the proposed method is then discussed.

4.6.1 Effect of the Expansion Mode Truncation

Two uniform-grating DFB lasers with different κL are further investigated to study the truncation effect in the field expansion. The LI curves are calculated by using the SWM-CCM taking different number of eigenmodes in the field expansion and the TWM results are also plotted for comparison purpose.

Shown in Figure 4.12 is the LI curve of a weak coupling structure with $\kappa L = 0.9$. It is found that an increasing number of the expansion modes would be necessary to achieve the same accuracy. This is attributed to the weak mode selectivity due to the low coupling strength. We therefore have no priori knowledge on which candidate "cold" cavity mode will eventually be selected as the lasing mode along with the bias evolves. Taking the extreme case in which the coupling coefficient is zero so that the optical feedback comes only from the facet reflection and multiple FP modes appear to lase. We would certainly need a large number of eigenmodes in the expansion, to cover these multiple lasing FP modes at least. Once the facet reflectivity is further set to zero, i.e. the device becomes a light emitting diode, the proposed model becomes infeasible as we wouldn't be able to truncate Eq. (4.23) at all.

For a strong coupling structure with $\kappa L = 2.4$, the LI curve is shown in Figure 4.13. It is observed that this laser becomes unstable at high power level that a pitchfork bifurcation occurs at around 70 mA. A similar instability has been found by Schatz [89]. It is seen from Figure 4.13 that the SWM-CCM with two expansion modes fails to predict such instability, whereas the simulation based on four expansion modes does predict the instability, but at the wrong bias. Satisfactory accuracy is only resumed with at least six expansion modes. Actually, although DFB structure with stronger coupling coefficient generally bears higher model gain differences, hence shows stronger mode selectivity, it is only true when the bias is low. As the bias grows, longitudinal spatial hole burning kicks on so that the lasing mode and the carrier (hence the gain) distributions become increasingly non-uniform with their changes in the opposite direction. As a result, weighed by the mode distribution, the modal gain of the lasing mode would decrease due to the reduced overlap between the mode and gain distributions, despite the average gain growth with the bias. LSHB, however, has little effect on the modal gains of the non-lasing modes simply due to the much weakened correlation between the non-lasing mode and the gain distributions. Therefore, the modal gain differences appear to reduce in high bias region once the LSHB is strong enough, which apparently leads to a reduction on the mode selectivity. Due to the correspondence between the coupling coefficient and the LSHB (i.e., structure with higher κL has stronger LSHB), we again need more modes in the expansion in order to capture any possible mode hopping and instability induced by the reduced mode selection mechanism in strongly coupled DFB structures.

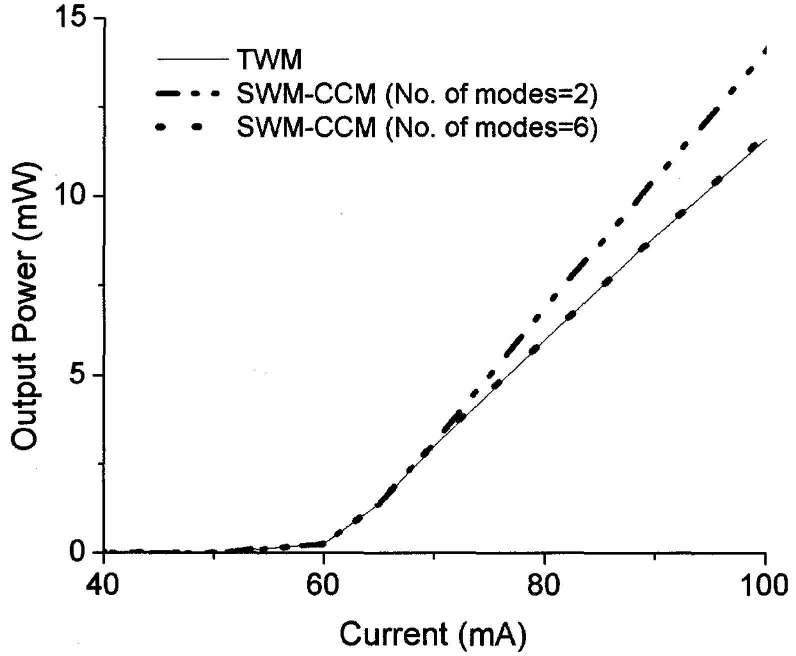

Figure 4.12 Comparison of LI characteristics of the uniform DFB laser with $\kappa L = 0.9$

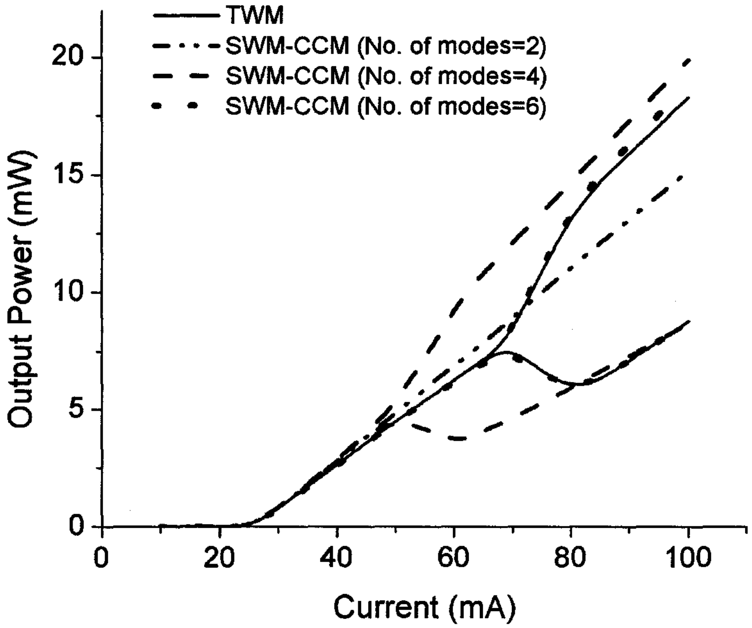

Figure 4.13 Comparison of LI characteristics of the uniform DFB laser with $\kappa L = 2.4$

Generally, this model becomes more accurate if more eigenmodes are taken in the expansion. However, this improvement on the accuracy is at the expense of the computation time which will be discussed later in this section. Therefore, the number of eigenmodes taken in the expansion needs to be carefully examined for a given laser structure and operation condition. In general, more modes would be required due to the deterioration of the mode selectivity for both weak and strong coupling strength.

4.6.2 Computation Efficiency

Last but not least, the computation efficiency of the proposed method is examined in this section. In the TWM, the laser cavity is discretized into a number of small subsections with equal length of Δz. The temporal step Δt is limited by $\Delta t = \Delta z / v_g$. It is therefore time consuming for the TWM if a dense spatial discretization has to be performed to correctly model the relatively large longitudinal variations of the carrier/photon distributions. That will force us to unnecessary small Δt and hence an increase in the computation time. Whereas, the SWM-CCM can adopt larger time step since Δt is no longer subjected to the above mentioned limitation. Table 4.3 lists the comparison of the computation time and the percentage error of the output power between these two methods for the uniform DFB laser with $\kappa L = 2.4$. The percentage error is defined as the error of the output power of the SWM-CCM with respect to the output power of the TWM. The normalized computation time is obtained as the overall time required for simulating the DFB laser during a time frame of 16ns normalized by the computation time needed for the TWM. It is seen that the higher computation efficiency can be achieved by applying the SWM-CCM in this example. Specifically, more than ¾ of the computation time can be saved even with 6 expansion modes with the error of the output power less than 2%. It is worth mentioning that the amount of the computation time that can be saved by using the SWM-CCM is problem-dependent.

	TWM	SWM-CCM (mode # = 2)	SWM-CCM (mode # = 4)	SWM-CCM (mode # = 6)
Errors of Output Power	0%	12%	5.8%	1.8%
Normalized Computation Time	1	~ 1/6	~ 2/11	~ 11/50

Table 4.3 Comparison of the computation time between the SWM-CCM and the TWM

4.7 Summary

A standing wave model based on the expansion in terms of resonant modes of the "cold" cavity is developed and validated as an efficient numerical tool for modeling of DFB laser diodes. In the proposed model, the "cold" cavity modes only need to be calculated once as a priori with little computation efforts, yet the structural details of the laser cavity are accounted for. The temporal evolution of amplitudes of these modes is obtained by solving a set of ordinary differential equations in stead of partial differential equations for the traveling wave model. Although the application examples are on uniform-grating and $\lambda/4$ -shifted DFB structures, the presented approach is widely applicable to a variety of structures such as those with multiple phase shifts or multiple sections.

Chapter 5

Standing Wave Model Based on Threshold "Hot" Cavity Modes

5.1 Introduction

In the last chapter, a standing wave model based on "cold" cavity modes expansion is presented where the coupling coefficient κ plays a rather important role. It describes the power transfer between the two contra-directional waves propagating inside the laser cavity, i.e. it is a major feedback mechanism for DFB lasers. This distributed feedback property, along with the facet reflections if there are any, forms the eigenmodes of the "cold" cavity. However, we may notice that the coupling coefficient is only contained within the "cold" cavity operator in that model. This implies that κ is bias-independent. This assumption is generally valid for the index-coupled DFB laser, where the change of the carrier density has a negligible impact on the coupling coefficient. However, this might not be true for gain-coupled DFB lasers, another type of DFB laser having advantages of higher single-mode yields [46] and less dependence on facet reflectivities [90], etc., compared with index-coupled DFB lasers.

Basically, there exist two possible mechanisms for realizing a gain grating: 1) periodic variation of the gain; 2) periodic variation of the loss. The former has a gain coupling coefficient κ_{gain} dependent on the carrier density, hence on the injection level, but the latter usually does not. The carrier dependent coupling coefficient κ will cause a variation of the threshold gain and the lasing frequency and have a big impact on the dynamic behavior of gain-coupled DFB lasers. In order to take these effects into account, we proposed an alternative standing wave model where optical fields are expanded in terms of the "hot" cavity modes obtained near the threshold current. The major reason we choose this threshold reference point is that the carrier density is known to be almost clamped for the current above threshold, especially when the LSHB effect is not very severe. Consequently, the coupling coefficient is thus mostly determined at threshold. As such, we may divide the original operator in Eq. (4.1) into two parts: one is fixed near threshold and the other is allowed to vary with time, catching the parameter change from the threshold condition. In this model, the eigenmodes under the bias near threshold also only need to be calculated once as a priori knowledge.

5.2 Eigen-Solutions of the Threshold "Hot" Cavity Modes

The operator $\mathbf{H}_t$ in Eq. (4.1) can be split into two parts

$$\mathbf{H}_t = \mathbf{H}^{th} + \mathbf{H}^{a} \tag{5.1}$$

where the superscript "*th*" denotes the value near threshold and the superscript "*a*" denotes the value deviated from the threshold. For instance, the two operators in Eq. (5.1) will take the form of

$$\mathbf{H}^{th}=\upsilon_g\begin{bmatrix} Q^{th}-\partial/\partial z & j\kappa^{th} \\ j\kappa^{th} & Q^{th}+\partial/\partial z \end{bmatrix} \tag{5.2}$$

$$\mathbf{H}^{a}=\upsilon_g\begin{bmatrix} Q^{a} & j\kappa^{a} \\ j\kappa^{a} & Q^{a} \end{bmatrix} \tag{5.3}$$

where

$$Q^{th}=\frac{\Gamma g_N\left(N_{th}-N_0\right)}{2}(1+j\alpha_m)-\frac{\alpha_i}{2} \tag{5.4}$$

$$Q^{a}=\frac{\Gamma g_N\left(N-N_{th}\right)}{2(1+\varepsilon P)}\left(1+j\alpha_m\right) \tag{5.5}$$

and the expressions for κ^{th}, κ^{a} will be given for the different gain gratings in Sec. 5.3. The nonlinear gain saturation effect is negligible small near threshold, consequently not included in Eq. (5.4) .

Again, consider the eigenvalue problem as follows

$$\mathbf{H}^{th}\mathbf{\Phi}_n^{th}=\xi_n^{th}\mathbf{\Phi}_n^{th} \tag{5.6}$$

where $\mathbf{\Phi}_n^{th}=\begin{bmatrix}\phi_f^{th}(z)\\ \phi_r^{th}(z)\end{bmatrix}_n$ are eigenfunctions of the operator $\mathbf{H}^{th}$ with eigenvalues ξ_n^{th}.

Similarly, $\mathbf{\Phi}_n^{th}$ and ξ_n^{th} can be obtained by using the TMM methods introduced in Sec. 4.2 under the facet conditions. The eigenvalues ξ_n^{th} are complex numbers with the real part characterizing the mode decaying rate and the imaginary part presenting the shift of resonance frequency from the reference frequency when the laser is biased near threshold. The eigenfunctions $\mathbf{\Phi}_n^{th}$ give the characteristic field patterns within the laser cavity near threshold. For a uniform-grating DFB laser, we may readily derive that the eigenfunctions of the operator $\mathbf{H}^{th}$ takes the form of

$$\begin{bmatrix} \phi_f^{th}(z) \\ \phi_r^{th}(z) \end{bmatrix}_n = \begin{bmatrix} r_1 \cosh \gamma_n z + \dfrac{\left(Q^{th} - \xi_n^{th}/v_g\right) r_1 + j\kappa^{th}}{\gamma_n} \sinh \gamma_n z \\ \cosh \gamma_n z + \dfrac{-j\kappa^{th} r_1 + \xi_n^{th}/v_g - Q^{th}}{\gamma_n} \sinh \gamma_n z \end{bmatrix} \tag{5.7}$$

where $\gamma_n = \sqrt{\left(Q^{th} - \xi_n^{th}/v_g\right)^2 + \left(\kappa^{th}\right)^2}$ and the complex eigenvalues ξ_n^{th} are the solution of the transcendental eigenvalue equation

$$\gamma_n (r_1 r_2 - 1) \cosh \gamma_n L + \left[(r_1 r_2 + 1)\left(Q^{th} - \xi_n^{th}/v_g\right) + j(r_1 + r_2)\kappa^{th} \right] \sinh \gamma_n L = 0 \tag{5.8}$$

5.3 Multimode Photon Wave Equations Based on Threshold "Hot" Cavity Modes

Similar to the method in the last chapter, the total field ψ can then be expanded in terms of these eigenmodes $\bar{\mathbf{\Phi}}_n^{th}(z)$ in the form of

$$\psi = \sum_{n=1}^{K} A_n(t) \bar{\mathbf{\Phi}}_n^{th}(z) \tag{5.9}$$

where $A_n(t)$ is the complex amplitude for each cavity mode. By exchanging the two components of the vector defined by Eq. (5.7), a set of adjoint eigenmodes $\mathbf{w}_m^{th}(z)$ can be obtained. It can also be verified that these adjoint modes are biorthogonal to the original eigenmodes $\bar{\mathbf{\Phi}}_n^{th}\left(z\right)$ such that

$$\int_0^L \bar{\mathbf{\Phi}}_n^{th}(z)\cdot\mathbf{w}_m^{th}(z)dz=\delta_{nm} \tag{5.10}$$

Substitute Eq. (5.9) into Eq. (4.1), multiply both sides by any adjoint eigenmodes $\mathbf{w}_m^{th}\left(z\right)$ and integrate over the cavity length, we obtain the complex amplitude of each longitudinal mode in the form of

$$\frac{dA_m(t)}{dt}=p'_{mm}A_m(t)+\sum_{n=1(n\neq m)}^{K}p'_{mn}A_n(t)+\tilde{\eta}'_m(t) \tag{5.11}$$

with

$$p'_{mm}=\xi_m^{th}+\int_0^L\mathbf{w}_m^{th}(z)\cdot\mathbf{H}^a\bar{\mathbf{\Phi}}_m^{th}(z)dz\,, \tag{5.12}$$

$$p'_{mn}=\int_0^L\mathbf{w}_m^{th}(z)\cdot\mathbf{H}^a\bar{\mathbf{\Phi}}_n^{th}(z)dz \tag{5.13}$$

and the Langevin noise term that drives the amplitude of each mode is given by

$$\tilde{\eta}'_m(t)=\int_0^L\tilde{\mathbf{s}}_t\left(z,t\right)\cdot\mathbf{w}_m^{th}(z)dz\,. \tag{5.14}$$

5.4 Model Validation and Applications

The model in this chapter is developed with the emphasis on dealing with DFB lasers with carrier-dependent coupling coefficient. As a result, it is applied to simulate two types of gain-coupled DFB lasers: purely gain-coupled DFB lasers and partly gain-coupled DFB lasers.

5.4.1 Purely Gain-Coupled DFB lasers

We will first consider the purely gain-coupled DFB laser with AR-coated facets. In this type of the device, the coupling coefficient is an imaginary number, i.e. $\kappa = j\kappa_{gain}$ with κ_{gain} given by [91]

$$\kappa_{gain} = \frac{1}{2}\int_{\text{gain grating}} \varepsilon(x)\Delta g E^2(x)\,dx \tag{5.15}$$

where $\varepsilon(x)$ is the Fourier component of the grating along the longitudinal direction and is taken as $1/\pi$ for a rectangular grating with a duty cycle of 50%. $E(x)$ is the normalized transverse optical field. Δg is the material gain. Then, Eq. (5.15) becomes

$$\kappa_{gain} = \frac{1}{2\pi}\frac{\Gamma_g g_N (N-N_0)}{1+\varepsilon P} \tag{5.16}$$

with Γ_g being the confinement factor of the gain grating. By this definition, κ^{th} and κ^{a} in Eq. (5.2) and (5.3) become

$$\kappa^{th} = \frac{\Gamma_g g_N (N_{th}-N_0)}{2\pi} \tag{5.17}$$

$$\kappa^{a} = \frac{\Gamma_g g_N (N-N_{th})}{2\pi(1+\varepsilon P)} \tag{5.18}$$

The nonlinear gain saturation effect is only pronounced for high optical power, therefore is neglected in Eq. (5.17) due to the small amount of power near threshold. One thing we need to point out is that changes in the carrier density will also give rise to an index variation due to the linewidth enhancement factor. In reality, this index variation could be approximately cancelled by a simultaneous thickness variation of a passive wave guiding layer leaving substantially a periodic gain only.

We may also notice the fact that the threshold modal gain is dependent on the coupling strength near threshold, which now in turn is a function of the threshold carrier density through Eq. (5.17). As a result, an iteration process is carried out to obtain the self-consistent solution of the threshold carrier density N_{th}, hence the threshold coupling coefficient κ^{th}.

The laser parameters of the device under investigation are chosen to be the same as those in [92] for the purpose of comparison which are listed in Table 5.1.

Parameters	**Values**
Reference wavelength λ_0 (μm)	1.55
Confinement factor Γ_g	0.35
Effective index without injection n_{eff0}	3.283
Group index n_g	3.7
Internal loss α (cm^{-1})	40
Differential gain g_N (10^{-16} cm^2)	3
Transparent carrier density N_0 (10^{18} cm^{-3})	1.5
Linewidth enhancement factor α_m	4.86
Linear recombination coefficient A (10^9 s^{-1})	0
Bimolecular radiation coefficient B (10^{-10} cm^3 s^{-1})	1
Auger coefficient C (10^{-29} cm^6 s^{-1})	3

Table 5.1 Purely gain-coupled DFB laser parameters

The static characteristics such as the LI curve, longitudinal variations of the carrier density and photon density under 5000 A/cm^2 injection density are obtained after the laser reaches its steady state and shown in Figure 5.1 and Figure 5.2, respectively. The results denoted by triangular symbol are from literature [92]. The inset in Figure 5.2 (a) shows the spatial variation of the gain coupling coefficient. A minimum κ_{gain} of $16.4\,\text{cm}^{-1}$ at the edge and a maximum of $20.9\,\text{cm}^{-1}$ at the center are obtained, which is consistent with results in [92] where $\kappa_{gain} \in [17.2, 20.8]\,\text{cm}^{-1}$. It is again found that five eigenmodes are necessary in the field expansion for this example. Figure 5.3 shows the large signal transient response of the laser when the bias is a step input from near threshold to $5000\,\text{A/cm}^2$.

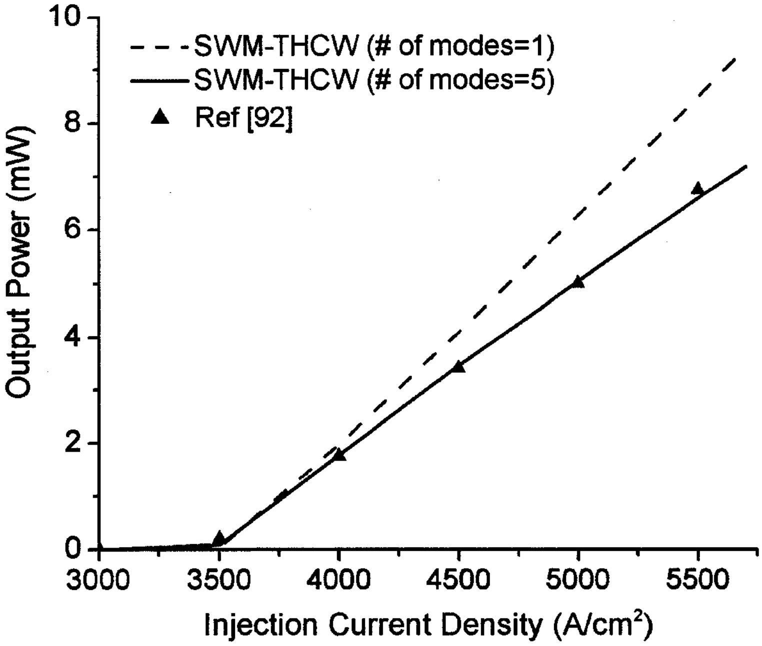

Figure 5.1 Comparison of LI characteristics of the purely gain-coupled DFB laser

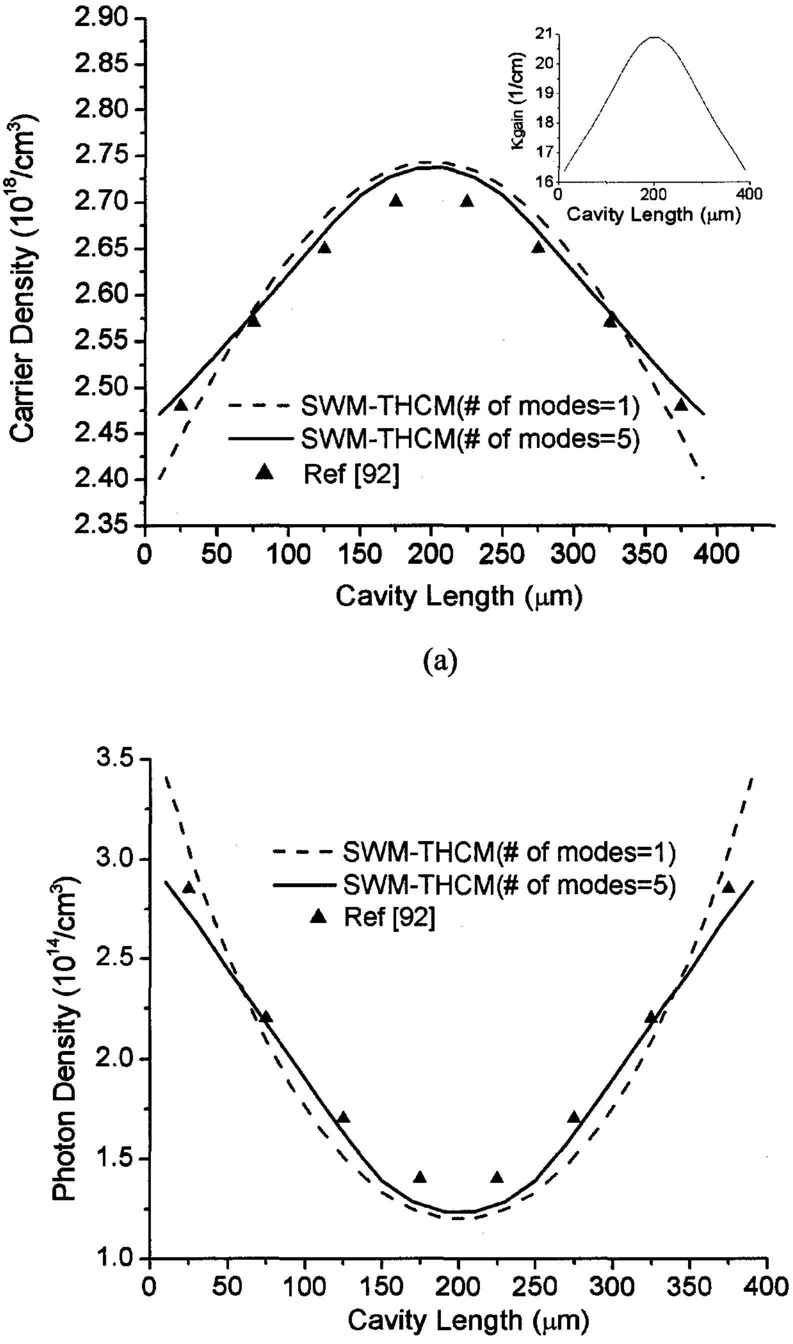

(a)

(b)

Figure 5.2 Comparison of (a) carrier density distribution (b) photon density distribution for the purely gain-coupled DFB laser

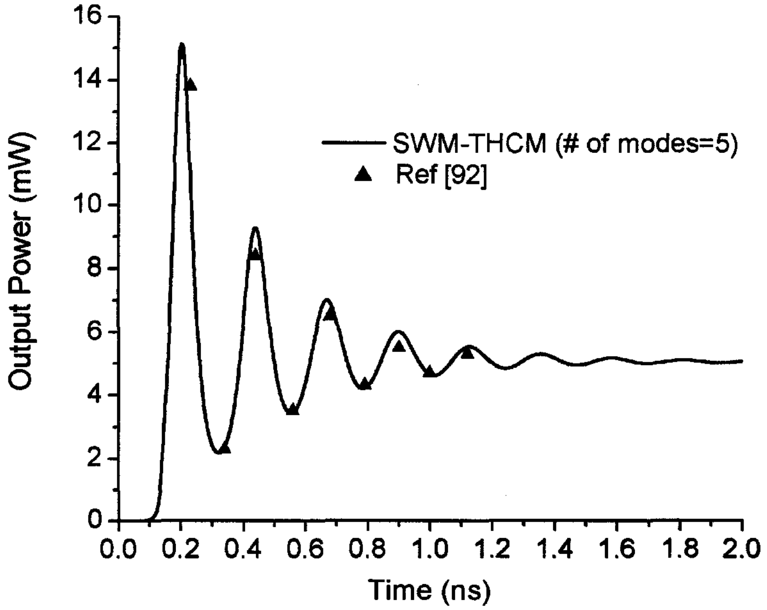

Figure 5.3 Comparison of the large signal transient response for the purely gain-coupled DFB laser

5.4.2 Partly Gain-Coupled DFB Lasers

In this section, the proposed model will be applied to simulate partly gain-coupled DFB lasers, also known as complex-coupled DFB lasers. When the gratings with periodic index and gain variations are both presented along the laser cavity, the coupling coefficient becomes a complex number, i.e. $\kappa = \kappa_{index} + j\kappa_{gain}$. The reason we consider the periodic gain variation instead of the loss variation is that such scenario is more challenging to be dealt with due to the carrier dependent gain coupling coefficient, as has been mentioned in Sec. 5.1. It is know that the change of the carrier density will induce a change of the refractive index through K-K relations, leading to the variations of both the index and gain coupling coefficients. A carrier scattering parameter Q_s is introduced as a measure of how the coupling between two contra-propagating traveling waves depends on the carrier density [93]

$$\frac{\partial \kappa}{\partial N} = Q_s \left(j - \alpha_m \right) \frac{\partial g}{\partial N} \,. \tag{5.19}$$

The value of Q_s is in the interval $\left[0,1\right]$, depending on the detailed grating structure. By the above definition, the coupling coefficient κ^{th} and κ^{a} can be written as

$$\kappa^{th} = \kappa_0 + \frac{\partial \kappa}{\partial N}\left(N_{th} - N_0\right) = \kappa_0 + Q_s \left(j - \alpha_m \right) \frac{\partial g}{\partial N}\left(N - N^{th}\right) \tag{5.20}$$

$$\kappa^{a} = \frac{\partial \kappa}{\partial N}\left(N - N_{th}\right) = Q_s \left(j - \alpha_m \right) \frac{\partial g}{\partial N}\left(N - N_{th}\right) \tag{5.21}$$

where κ_0 is the coupling coefficient at transparency.

The simulation example is an anti-phase partly gain-coupled DFB laser. Besides the single-mode operation, this type of gain-coupled DFB laser has several attracting characteristics such as large modulation bandwidth [92], [94] and reduced effective linewidth enhancement factor [95]-[97]. The device being investigated has a coupling coefficient-length product of approximately 1.4 with about 28% gain coupling ratio. The material line width enhancement factor is 3 and the carrier scattering parameter is 0.2. Other laser parameters are kept same as those listed in Table 5.1.

The similar static and dynamic characteristics as those shown in the last section are investigated and illustrated in Figure 5.4 to Figure 5.6, in comparing with the results calculated by the TWM. It is observed that those important output parameters such as the output power and relaxation oscillation frequency all agree well with the traveling wave model. It is also found that satisfying accuracy of the SWM-THCM is achieved by using only one expansion mode in the field expansion. This is attributed to two factors, namely: 1) the gain-coupled DFB laser under investigation is a well-behaved single-mode laser and 2) the threshold "hot" cavity mode very closely resembles the real mode under the given bias due to the less severe of LSHB effect.

To show the impact of the time-dependent coupling coefficient on the dynamic behavior of the gain-coupled DFB lasers, we also simulate the same device with a time-invariant coupling coefficient, i.e. the κ^a in Eq. (5.21) is set to zero and the corresponding result is also shown in Figure 5.6. From the comparison, we observed an increase of the oscillation frequency if taking the time-dependent coupling coefficient into account. The reason is explained as follows: the index and gain gratings are in anti-phase as illustrated in Figure 5.7. An increase of the carrier density increases the gain coupling strength; meanwhile it decreases the refractive index of lower index region, and hence also enhances the index coupling strength. As a result, the net differential gain with respective to the carrier density is enhanced due to the reduction of the cavity loss. The relaxation oscillation will then increase with the differential gain under certain injection level according to the analytical expression derived in [5]. This effect is further confirmed by the small signal analysis where the amplitude modulation (AM) response is shown in Figure 5.8. It is seen that a larger modulation bandwidth can be achieved by using the anti-phase gain-coupled DFB lasers. These results are consistent with what have been found in [92], [94].

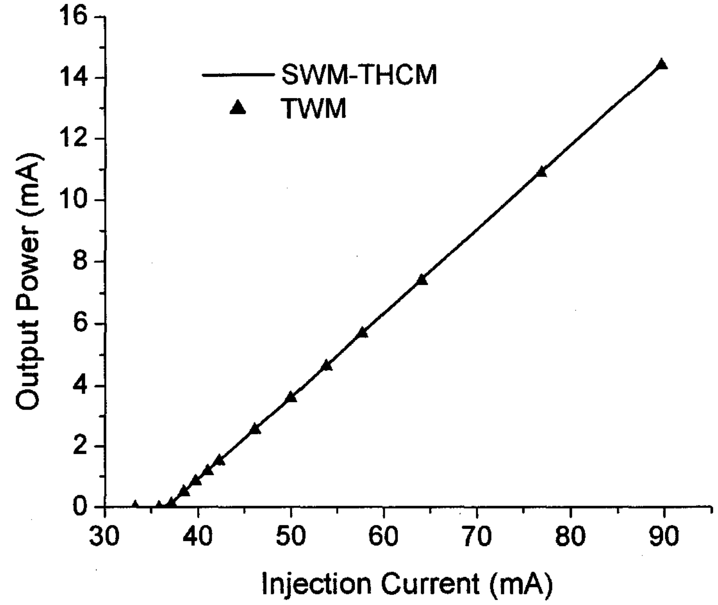

Figure 5.4 Comparison of LI characteristics for the anti-phase gain-coupled DFB laser

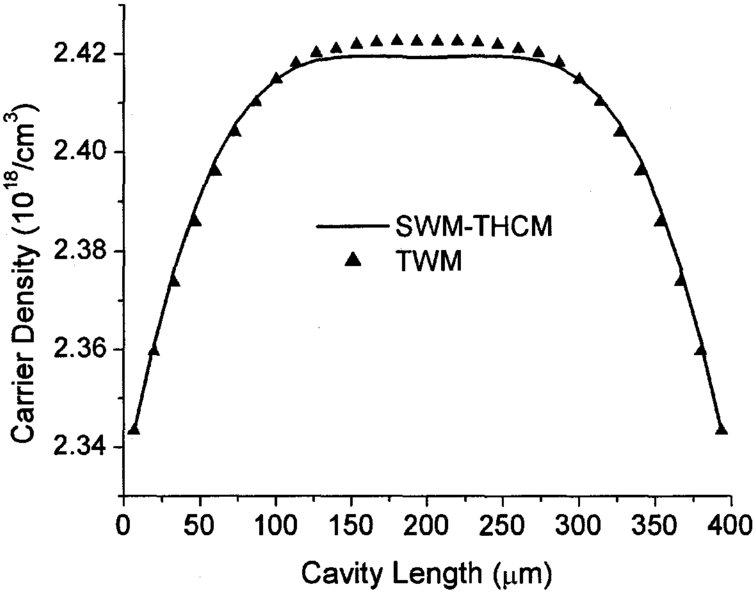

(a)

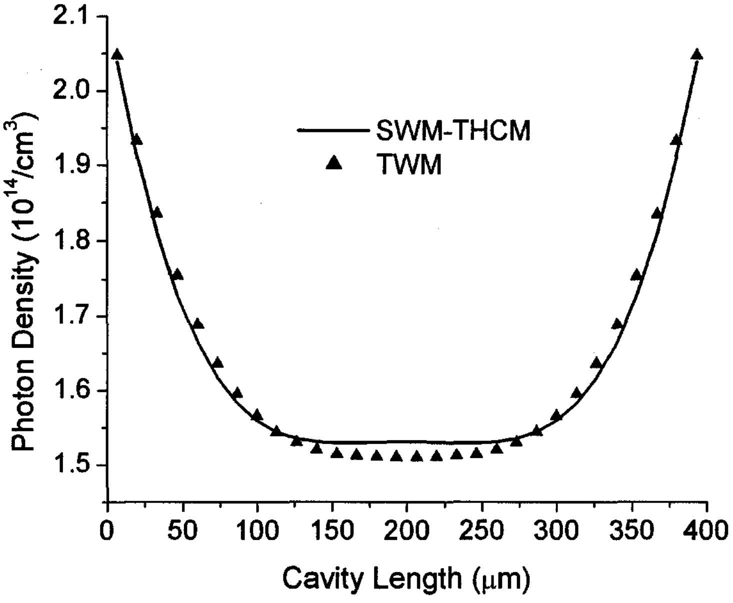

(b)

Figure 5.5 Comparison of (a) carrier density distribution (b) photon density distribution for the anti-phase gain-coupled DFB laser

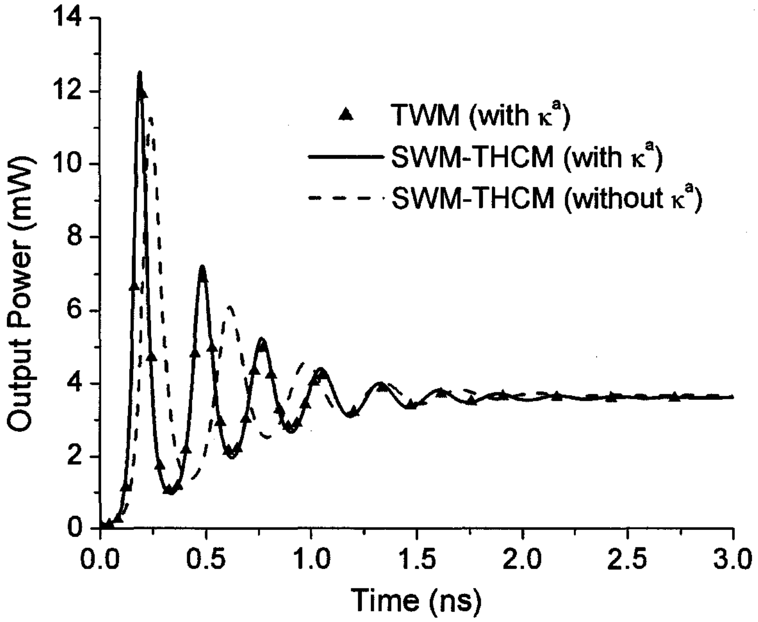

Figure 5.6 Comparison of the large signal transient response for the anti-phase gain-coupled DFB laser

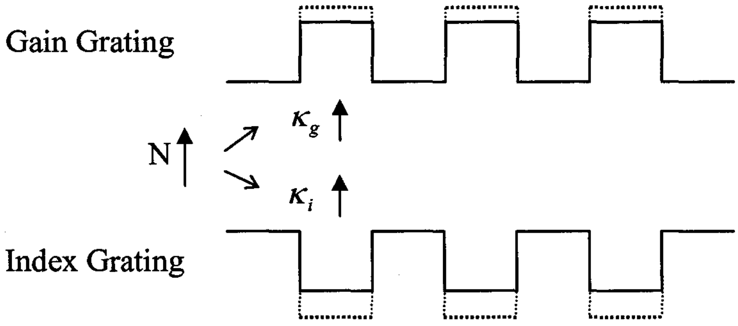

Figure 5.7 Schematic diagram of the grating structure for the anti-phase gain-coupled DFB lasers

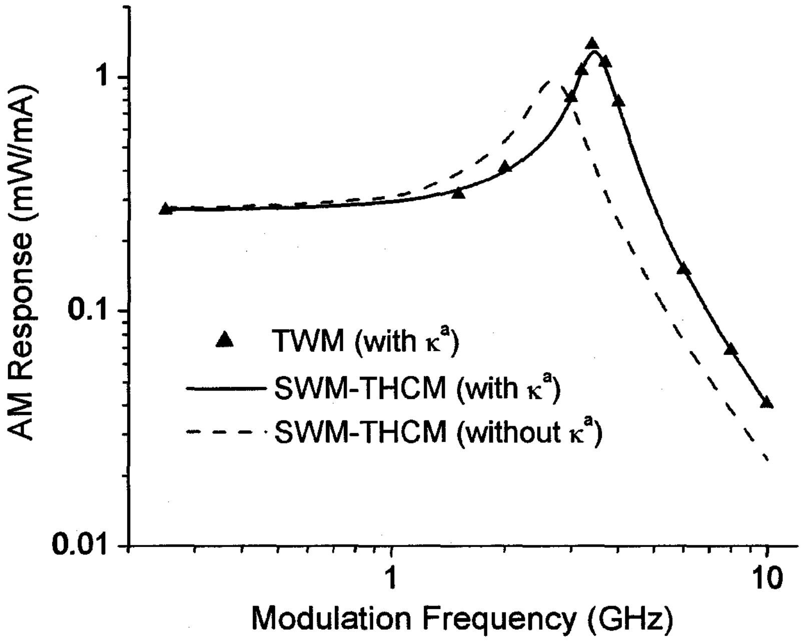

Figure 5.8 Comparison of the amplitude modulation (AM) responses for the anti-phase gain-coupled DFB laser

Compared with the SWM-CCM proposed in the last chapter, there are essentially two extra computational efforts for the SWM-THCM. One is to solve for threshold carrier density N_{th} which is a pre-processing work with little effort; the other is related to the extra off-diagonal terms of the operator $\mathbf{H}^a$ in Eq. (5.3) induced by the time-dependent coupling coefficient. This off-diagonal term will only result in one more term in the integrals of Eq. (5.12) and (5.13), which does not change the fact that the time for calculating the integral is proportional to the number of subsections being divided along the cavity. As a result, we may conclude that the proposed SWM-THCM is as efficient as the SWM-CCM.

5.5 Summary

In this chapter, we have successfully presented an alternative standing wave model based on "hot" cavity modes obtained near threshold. The complexity of the model is almost the same as that of the standing wave model based on "cold" cavity modes. However, it has the merit of being capable of simulating gain-coupled DFB lasers where the coupling coefficient is current dependent, hence time varying.

Chapter 6

Efficient Solution to the Standing Wave Model: Carrier Shape Approximation

6.1 Introduction

Due to the characteristic of distributed feedback in the laser cavity, the optical field and the carrier distributions are in general non-uniform along the cavity for a typical DFB laser under normal operation conditions. This LSHB effect depends greatly on the design parameters such as facet reflections, phase shift of the grating and the coupling coefficient-cavity length product (κL), as well as the operation parameters such as current injection levels. LSHB will have significant impact on the performance of the DFB laser, e.g., to give rise to the shift of the lasing wavelength [1], [98] and to lead to the deterioration of the side mode suppression ratio [39], [99]. For this reason, several approaches with different level of details and assumptions have been developed to incorporate the spatial dependence of the optical field and carrier distribution into the theoretical models. The work [100]-[102] are revisions to the conventional rate equations, where the discretization for both optical field and carrier distribution are not needed. Tucker [100] considers transverse SHB combined with carrier diffusion by assuming a sinusoidal carrier profiles over the cross section of the laser diodes. By applying the similar idea, Kinoshita [101] proposed a set of rate equations incorporating the longitudinal SHB effects along the waveguide axis. A more general profiles common to both photon and carrier densities are then developed to analyze the effect of SHB on the dynamic response of DFB lasers [102].

In traveling wave models, the laser cavity is divided into many segments to account for the variation of the optical field, which is obtained explicitly by solving PDEs with respective to the time and space. The carrier densities at different positions are obtained by solving a number of ODEs corresponding to the spatial segments being divided and assigned.

On the other hand, by using mode approximation techniques, the two standing wave models presented in the previous two chapters do not explicitly require the discretization of the optical field along the cavity. However, the carrier densities at different positions are still solved in the same manner to the TWM.

In this chapter, we will present a method to approximate the shape of the time-dependent carrier density distribution in recognition of the highly correlated patterns of the optical field and carrier density distributions, leading to a significant improvement of the computational efficiency of our previously proposed standing wave models. More concretely, the accuracy of the SWMs can be improved by adopting a larger number of eigenmodes in the field decomposition, which however cause the increase of the total computation time. This is due to the fact that more numerical integrations have to be carried out in Eqs. (4.24)-(4.26) or Eqs. (5.11)-(5.13) at each time step. By utilizing the fact that there is a carrier distribution pattern corresponding to the photon distribution, those integrals in the optical field equations can be obtained as a priori. Moreover, the number of carrier rate equations to be solved can be reduced greatly as well. It is worth mentioning that the presented approach in this chapter is applicable to both SWM-CCM and SWM-THCM. However the model improvement is applied to the SWM-CCM in this chapter as a demonstration. The improved SWM-THCM can also be achieved if the similar process shown in this chapter is followed.

This chapter is organized as follows. The method to extract the carrier shape function is presented in Sec. 6.2. The approximation to the carrier density distribution by using the extracted shape function is introduced in Sec. 6.3. The simplified standing wave model is derived in Sec. 6.4. Sec. 6.5 gives model validation and comparisons. The accuracy and efficiency of this model is discussed in Sec. 6.6. Finally, a summary is given in Sec. 6.7.

6.2 Longitudinal Optical Modes and Deviation Shape Function Extraction

By using Eq. (4.23), the photon density at any position z along the laser cavity can be written as

$$P(z,t)=\psi\cdot\psi^{*}=\sum_{n=1}^{K}B_n^p\Theta_n^p+\sum_{\substack{n,m=1\\(n\neq m)}}^{K}B_{nm}^{cr}\Theta_{nm}^{cr} \tag{6.1}$$

where $B_n^p=|A_n|^2$, $B_{nm}^{cr}=A_nA_m^{*}$, and

$$\Theta_n^p=\bar{\mathbf{\Phi}}_n^0\cdot\left(\bar{\mathbf{\Phi}}_n^0\right)^{*}, \tag{6.2}$$

$$\Theta_{nm}^{cr}=\bar{\mathbf{\Phi}}_n^0\cdot\left(\bar{\mathbf{\Phi}}_m^0\right)^{*}. \tag{6.3}$$

The integration of the first term in Eq. (6.1) is the sum over the "power per eigenmode" where the individual "photon density mode" Θ_n^p has been normalized to unity, i.e. $\int_0^L \Theta_n^p(z)\,dz = 1$. The integration of the second term in Eq. (6.1) describes the "cross powers" between cavity modes.

The average photon density along the laser cavity is obtain by

$$\begin{aligned} P_{av}(t) &= \frac{1}{L}\int_0^L P(z,t)\,dz \\ &= \frac{1}{L}\left(\sum_{n=1}^{K} B_n^p(t)\int_0^L \Theta_n^p(z)\,dz + \sum_{\substack{n,m=1\\ n\neq m}}^{K} B_{nm}^{cr}(t)\int_0^L \Theta_{nm}^{cr}(z)\,dz\right). \end{aligned} \tag{6.4}$$

The photon density distribution in Eq. (6.1) can then be defined as

$$P(z,t) = P_{av}(t)\left[1 + f(z,t)\right] \tag{6.5}$$

where $f(z,t)$ is denoted as the deviation shape function of the photon distribution and can be extracted out from Eq. (6.5) as

$$f(z,t) = \frac{1}{P_{av}(t)}\left(\sum_{n=1}^{K} B_n^p(t)\Theta_n^p(z) + \sum_{\substack{n,m=1\\ n\neq m}}^{K} B_{nm}^{cr}(t)\Theta_{nm}^{cr}(z)\right) - 1 \tag{6.6}$$

with $\int_0^L f(z,t)\,dz = 0$.

6.3 Longitudinal Carrier Distribution Approximation

The carrier rate equation (2.18) can be simplified as

$$\frac{dN(z,t)}{dt}=\frac{I}{eV_a}-\frac{N(z,t)}{\tau_c}-\upsilon_g g_N\left[N(z,t)-N_0\right]P(z,t) \tag{6.7}$$

where τ_c is effective carrier life time. It is observed from Eq. (6.7) that the carrier distribution takes the form

$$N(z,t)=\frac{a(z,t)}{1+b(t)P(z,t)}+c \tag{6.8}$$

where $a(z,t)=\tau_c\left[\frac{I}{eV_a}-\frac{dN(z,t)}{dt}\right]-N_0$, $b(t)=\tau_c\upsilon_g g_N$, $c=N_0$. The time-dependent $b(t)$ implies that the effective carrier life time can also vary with time. The first-order approximation for the Taylor expansion of Eq. (6.8) can be obtained as described below provided that $|b(t)P(z,t))|\ll 1$, i.e. the optical power of the laser is not very high,

$$N(z,t)\approx\left[a(t)+c\right]-a(t)b(t)P(z,t). \tag{6.9}$$

where the z-dependence of a is dropped with assumptions that the carrier density at each position z is homogeneously changing with time and the current injection is uniform along the laser cavity.

By using Eq. (6.5), the time-dependent carrier distribution Eq. (6.9) can be equivalently written as

$$N(z,t)\approx N_a(t)-D(t)f(z,t) \tag{6.10}$$

where $N_a(t)$ and $D(t)$ imply the average carrier density and the carrier deviation from its average along the laser cavity, respectively. Equation (6.10) is actually same as the one given phenomologically in [100]-[102]. The function $f(z,t)$ describes the shape of the carrier non-uniformity and is determined mainly by parameters of the laser itself such as κL and facet reflectivity. It is reasonable to take $f\left(z,t\right)$ to be slowly varying compared with $D(t)$ under the moderate power assumption. Equation (6.10) is understandable in the sense that more carriers are consumed where the light intensity is greater. The carrier density should, therefore, distribute inhomogeneously along the cavity with a pattern opposite from that of the light intensity inside the laser cavity.

6.4 Simplified Standing Wave Model

Substituting Eq. (6.10) into Eq. (4.24) and utilizing Eq. (6.6), we obtain

$$\frac{dA_m(t)}{dt} = p''_{mm}A_m(t) + \sum_{n=1(n\neq m)}^{K} p''_{mn}A_n(t) + \tilde{\eta}_m(t) \tag{6.11}$$

with

$$\begin{aligned} p''_{mm} &= \xi_m^0 + \frac{\Gamma \upsilon_g g_N}{2(1+\varepsilon P_{av})}(1+j\alpha_m)\left(N_a - N_0 - D\int_0^L f\,\mathbf{w}_m\bar{\mathbf{\Phi}}_m^0\,dz\right) \\ &= \xi_m^0 + \frac{\Gamma \upsilon_g g_N}{2(1+\varepsilon P_{av})}(1+j\alpha_m)\left[N_a - N_0 + D - \frac{D}{P_{av}}\right. \\ &\quad \left.\times\left(\sum_{s=1}^{K} B_s^p\int_0^L \Theta_s^p\mathbf{w}_m\bar{\mathbf{\Phi}}_m^0\,dz + \sum_{\substack{s,t=1\\ s\neq t}}^{K} B_{st}^{cr}\int_0^L \Theta_{st}^{cr}\mathbf{w}_m\bar{\mathbf{\Phi}}_m^0\,dz\right)\right] \end{aligned}, \tag{6.12}$$

$$\begin{aligned} p''_{mn} &= -\frac{\Gamma \upsilon_g g_N}{2(1+\varepsilon P_{av})}(1+j\alpha_m)D\int_0^L f\,\mathbf{w}_m\bar{\mathbf{\Phi}}_n^0\,dz \\ &= -\frac{\Gamma \upsilon_g g_N(1+j\alpha_m)D}{2P_{av}(1+\varepsilon P_{av})}\left(\sum_{s=1}^{K} B_s^p\int_0^L \Theta_s^p\mathbf{w}_m\bar{\mathbf{\Phi}}_n^0\,dz + \sum_{\substack{s,t=1\\ s\neq t}}^{K} B_{st}^{cr}\int_0^L \Theta_{st}^{cr}\mathbf{w}_m\bar{\mathbf{\Phi}}_n^0\,dz\right) \end{aligned}. \tag{6.13}$$

Suppose that the laser cavity is oscillating in a dominant single longitudinal mode with a large side mode suppression ratio, which is valid for most of the applications. The cross power between the eigenmodes is much smaller than the power carried by the lasing mode. Eq. (6.1) and (6.6) can then be simplified respectively as

$$P(z) = \sum_{n=1}^{K} B_n^p \Theta_n^p , \tag{6.14}$$

$$f(z,t) = L\sum_{n=1}^{K} \sigma_n(t)\Theta_n^p(z) - 1 \tag{6.15}$$

where $\sigma_n = B_n^p \Big/ \sum_{n=1}^{K} B_n^p$. As a result, the Eq. (6.12) and (6.13) can be simplified as

$$p''_{mm} = \xi_m^0 + \frac{\Gamma \upsilon_g g_N (1 + j\alpha_m)}{2(1+\varepsilon P_{av})}\left(N_a - N_0 + D - DL\sum_{s=1}^{K} \sigma_s \int_0^L \Theta_s^p \mathbf{w}_m \bar{\mathbf{\Phi}}_m^0 \, dz \right), \tag{6.16}$$

$$p''_{mn} = -\frac{\Gamma \upsilon_g g_N L (1 + j\alpha_m)}{2(1+\varepsilon P_{av})} D\sum_{s=1}^{K} \sigma_s \int_0^L \Theta_s^p \mathbf{w}_m \bar{\mathbf{\Phi}}_n^0 \, dz . \tag{6.17}$$

The analytical expressions of the integrals in Eq. (6.16) and (6.17) for a typical DFB laser with uniform-grating are derived in Appendix B. It is noted that all these integrals can be pre-determined and computed for a given DFB laser structure before the computation of the standing wave equations.

Substituting Eq. (6.5) and (6.10) into (2.18) and integrating it along the cavity length L, we obtain

$$\frac{dN_a}{dt} = \frac{I}{eV} - AN_a - B\left(N_a^2 + \theta_2 D^2\right) - C\left(N_a^3 + 3\theta_2 N_a D^2 - \theta_3 D^3\right) - \upsilon_g \frac{g_N (N_a - N_0 - D\theta_2)}{1 + \varepsilon P_{av}} P_{av} . \tag{6.18}$$

By multiplying Eq. (2.18) by $f(z,t)$ and carrying the integral along the cavity length L, we obtain

$$\frac{dD}{dt}=-AD+\left(BD^2\theta_3/\theta_2-2BDN_a\right)-CD\left(3N_a^2-3N_aD\theta_3/\theta_2+D^2\theta_4/\theta_2\right)+\upsilon_g\frac{g_NP_{av}}{1+\varepsilon P_{av}}\left(N_a-N_0-D+D\theta_3/\theta_2\right) \tag{6.19}$$

where $\theta_2=\frac{1}{L}\int_0^L f^2\,dz$, $\theta_3=\frac{1}{L}\int_0^L f^3\,dz$ and $\theta_4=\frac{1}{L}\int_0^L f^4\,dz$. In obtaining Eq. (6.19), the time derivative of the slow varying term has been neglected.

Finally, the original governing equations (4.24) and (2.18) are reduced to (6.11), (6.18) and (6.19), which are solved in a self-consistent manner.

6.5 Model Validation and Comparisons

The device being investigated is the typical uniform-grating DFB laser with $\kappa L=1.5$. The modeling parameters are same as those listed in Table 4.1. The improved model, denoted as SWM-CCM Scheme II, is validated through comparisons made on the device static and dynamic properties with the previously proposed standing wave model based on cold cavity modes, denoted as SWM-CCM Scheme I.

A. Static Characteristics

The static characteristics are achieved by allowing the laser reach its steady state. Shown in Figure 6.1 (a), (b) is the photon and carrier density distribution along the laser cavity under the bias current of 60mA, respectively. Figure 6.2 shows its LI curve. It is seen that the scheme proposed in this paper can predict the static performance of this laser very well.

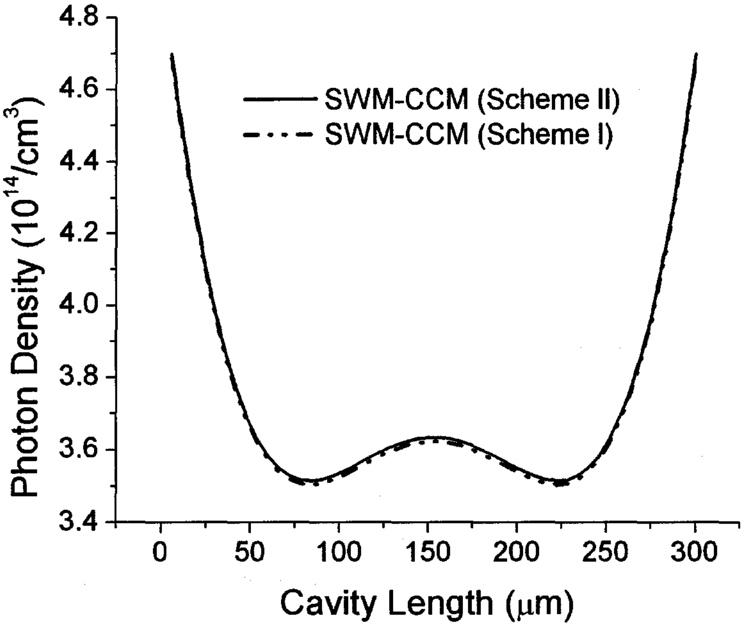

(a)

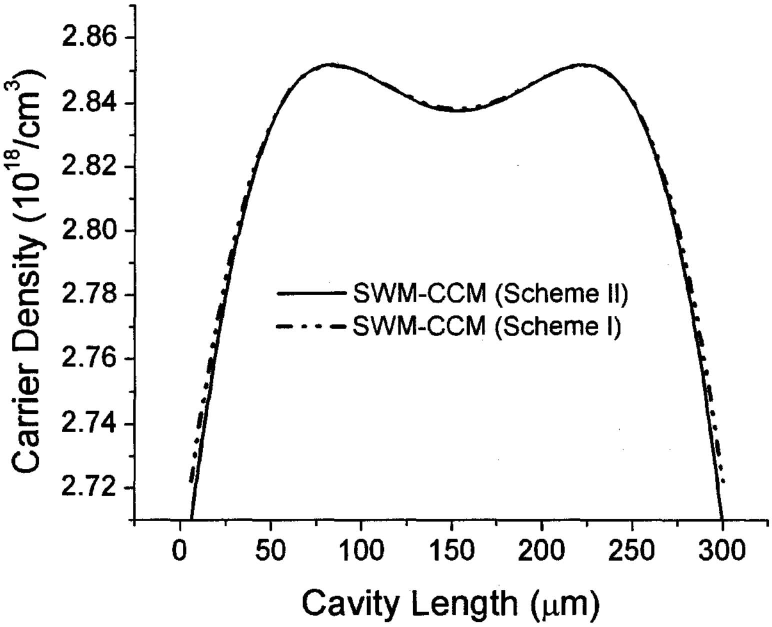

(b)

Figure 6.1 Comparison of longitudinal distribution of (a) Photon density (b) Carrier density

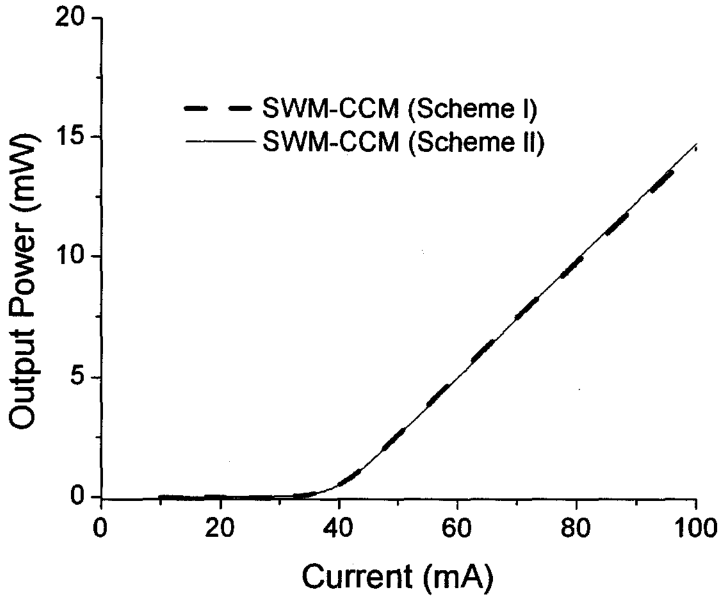

Figure 6.2 Comparison of LI curve

B. Dynamic Characteristics

Figure 6.3 shows the optical output power during the large signal modulation. The laser is initially biased at 50mA and then modulated by a 0.5GHz square wave with modulation amplitude of 20mA. It is observed that these two schemes show a small discrepancy when the output power is relatively high. This is caused by the error induced by the first-order approximation to Eq. (6.8). Shown in Figure 6.4 are the variation of the average carrier density $N_a(t)$ and the carrier inhomogeneity coefficient $D(t)$ during the modulation. From Figure 6.4, we can see that D increases with the increase of the output power, i.e. the carrier distribution becomes more deviated from its average value. As a result, the approximation in Eq. (6.10) becomes less valid. The error of output power at bit "1" in this case is approximately 2%, which is calculated by $\left|(P_{II}-P_I)/P_I\right|\times 100\%$

where P_I and P_{II} denote the output power calculated by scheme I and scheme II, respectively.

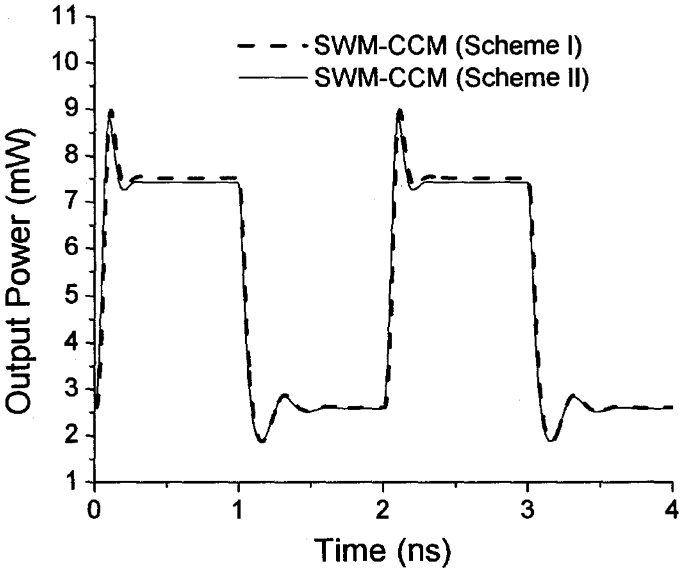

Figure 6.3 Comparison of the output power during the large signal modulation

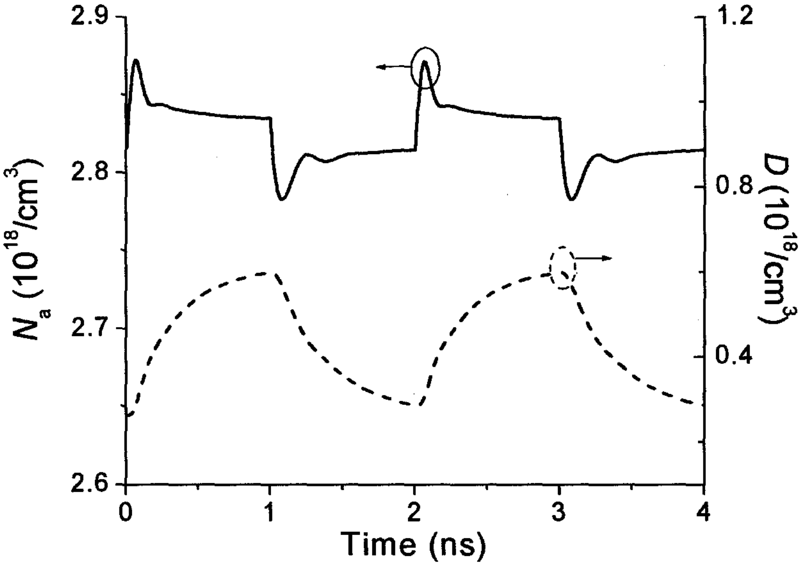

Figure 6.4 Variations of the average carrier density and carrier inhomogeneity coefficient under the large signal modulation

6.6 Discussions

Table 6.1 shows the comparison between the SWM-CCM Scheme I and SWM-CCM Scheme II.

	Optical field (forward & backward)		Carrier density		Total # of ODEs
	Discretization	# of ODEs	Discretization	# of ODEs	
SWM-CCM Scheme I	no	*K*	yes	*M*	*K*+*M*
SWM-CCM Scheme II	no	*K*	no	2	*K*+2

M: The number of subsections divided along the laser cavity
K: The number of eigenmodes used in the field expansion

Table 6.1 Comparison of the SWM-CCM Scheme I and Scheme II

In the previously proposed SWM-CCM scheme I, the carrier density evolution at different position inside the laser cavity is obtained by discretizing the cavity into a number of subsections. For lasers with cavity length of several hundred micrometers, the number of subsection *M* is expected to be in several tenths. As a result, it is apparent from the Table 6.1 that the number of equations to be solved for the scheme II is much less than that for the scheme I and independent of the cavity length as well. Furthermore, in comparison with the scheme I, the proposed scheme II is also more efficient in solving the optical field equations (4.24)-(4.26). This is due to the fact that the integrals therein can now be calculated beforehand.

Generally speaking, the device structure, material parameters and operation conditions, such as the coupling coefficient length product κL, differential gain, and the injection level, will all have impacts on the validity of the presented model. Figure 6.5 shows the variation of the percentage error of the output power with the injection level for the same DFB laser but with different κL. More eigenmodes are used in the optical field expansion for the device with a higher κL, which explains its higher accuracy in the low current range. However, with the increase of the injection current, the error of the output power of the device with $\kappa L = 2.1$ increase much faster than the one with $\kappa L = 1.5$. This is due to the fact that higher optical power resulting from a higher injection level will cause a more non-uniform carrier distribution for the device with a larger κL. Meanwhile, the structure with $\kappa L = 1.5$ is less affected by the LSHB and shows a higher accuracy in the high current range.

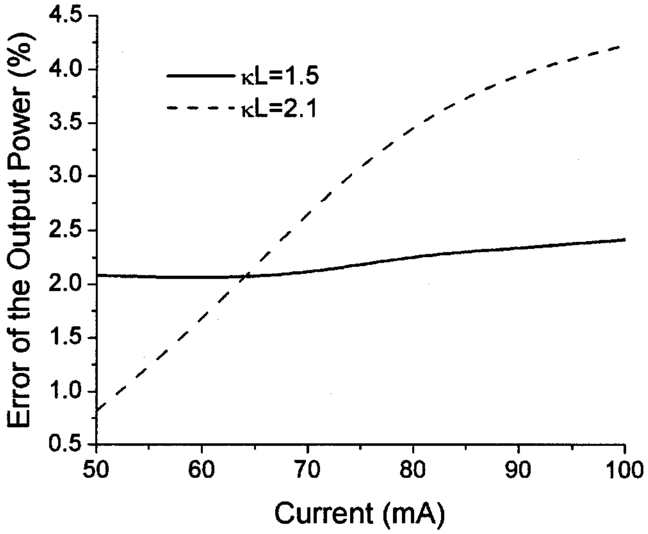

Figure 6.5 Variation of the error of the output power with the injection current for uniform-grating DFB lasers with different κL

The accuracy of this model can be further improved by incorporating higher order terms of the Taylor expansion when approximating Eq. (6.8). For example, the time-dependent carrier distribution can be approximated to the second-order accuracy as

$$N(z,t) \approx N_a(t) - D_1(t) f\left(z,t\right) + D_2^2(t) f^2\left(z,t\right). \tag{6.20}$$

Such that there will be three rate equations, associated with $\frac{dN_a}{dt}$, $\frac{dD_1}{dt}$ and $\frac{dD_2}{dt}$, governing the change of the carrier densities. For cases where the optical power is large enough to invalidate the moderate power assumption, we may have another strategy that we divide both the numerator and denominator of the Eq. (6.8) by bP as

$$N\left(z,t\right) = \frac{a(z,t)/\left[b(t)P\left(z,t\right)\right]}{1/\left[b(t)P\left(z,t\right)\right]+1} + c\,. \tag{6.21}$$

We may then carry out the Taylor expansion of Eq. (6.21) in terms of $\frac{1}{bP}$, which now satisfy $\left|\frac{1}{bP}\right| \ll 1$. After using Eq. (6.5) and retaining the first two terms in the expansion, the carrier density distribution can be derived to take the form of

$$N(z,t) = \frac{x(t)}{1+f\left(z,t\right)} - \frac{y(t)}{\left[1+f\left(z,t\right)\right]^2} + N_0\,. \tag{6.22}$$

Through a similar procedure, the rate equations for $\frac{dx}{dt}$ and $\frac{dy}{dt}$ can be obtained and used to simulate the case where the optical power is relatively high, together with mode amplitude equations.

6.7 Summary

This chapter describes an improved solution to the standing-wave models proposed in the previous two chapters for simulating DFB laser diodes. By utilizing the fact that the longitudinal carrier distribution has an opposite pattern from that of the photon distribution inside the laser cavity, an approximation to the carrier distribution is made under the moderate power assumption. This allows the integrals involved in the standing wave formulation to be performed beforehand and also leads to a great reduction to the number of carrier rate equations to be solved, consequently resulting in a more efficient solution to the previously proposed standing wave models.

Chapter 7

Rate Equations for the Photon Number and Phase

7.1 Introduction

There are normally two types of classical rate equation (0D) numerical models of DFB lasers. The first model, so-called conventional photon number rate equation [53], [80] is derived from the concept of particle balance, although well established and studied, does not include any phase information of the optical fields and neglects the variations of the fields and carriers along the laser cavity. However, for the distributed-feedback laser, the phase of the fields and non-uniformities could be very strong and therefore play a rather important role in determining the lasing frequency and predicting dynamic behaviors of the laser. As such, the conventional rate equation model may not be suitable for simulating DFB lasers. The second type of model, derived from the concepts of the classical electromagnetic-field exchange of energy, is the traveling-wave amplitude equation, from which the rate equations for the photon number and phase can be obtained [5], [47]. This improved model includes the phase change of optical waves, but still ignores the non-uniformities along the laser cavity.

This chapter derives the one-dimensional (1D) single-mode photon number and phase rate equations from the previously proposed standing wave model taking account of both phase and non-uniformities of the optical field. The presented rate equations can be written in a similar form to the conventional single-mode 0D model. The linkage between 0D and 1D model is then established and discussed.

7.2 Rate Equations of the Photon Number and Phase

Due to the good mode selectivity of the distributed feedback structure, DFB lasers can normally be well modeled by the single-mode rate equations. We will then derive the single-mode rate equations of the photon number and phase from the complex wave equations described by Eq. (4.24) or Eq. (5.11). Considering that the standing wave model based on threshold "hot" cavity modes is more general in the sense that it is able to deal with both index-coupled and gain-coupled DFB lasers, we choose the mode amplitude equation (5.11) as our starting point. By neglecting all the cross terms in Eq. (5.11) and only keeping the dominant mode amplitude $A(t)$, we arrive at

$$\frac{dA(t)}{dt} = p' A(t) + \tilde{\eta}'(t) \tag{7.1}$$

with

$$\begin{aligned} p' &= \xi^{th} + \int_0^L \mathbf{w}^{th}(z)\mathbf{H}^a \bar{\mathbf{\Phi}}^{th}(z)dz \\ &= \xi^{th} + \upsilon_g \int_0^L Q^a\left(z\right)\mathbf{w}^{th}(z)\bar{\mathbf{\Phi}}^{th}(z)dz + \upsilon_g \int_0^L \mathbf{w}^{th}(z)\begin{bmatrix} 0 & j\kappa^a \\ j\kappa^a & 0 \end{bmatrix}\bar{\mathbf{\Phi}}^{th}(z)dz\,, \\ &= \xi^{th} + \upsilon_g \int_0^L Q^a\left(z\right)\mathbf{w}^{th}(z)\bar{\mathbf{\Phi}}^{th}(z)dz + \upsilon_g \int_0^L j\kappa^a\left(z\right)\mathbf{w}^{th}(z)\bar{\mathbf{\Phi}}^{th\prime}(z)dz \end{aligned} \tag{7.2}$$

where $\bar{\mathbf{\Phi}}^{th\prime}(z)$ is obtained by swapping the two elements in $\bar{\mathbf{\Phi}}^{th}(z)$ and Eq. (5.3) is utilized.

The complex mode amplitude $A(t)$ can be written as

$$A(t)=\sqrt{S(t)}\exp\left(j\vartheta(t)\right), \tag{7.3}$$

where $S(t)$ is the photon number inside the laser cavity and $\vartheta(t)$ is the phase of the slowly varying envelope of the optical field. It is noticed that, in chapter 4 and chapter 5, $\left|A(t)\bar{\Phi}(z)\right|^2$ has the dimension of the photon density (cm^{-3}). However, in order to compare with the existing rate equation model, the dimension of $A(t)$ in this chapter is assigned such that $\left|A(t)\right|^2$ is the number of photons $S(t)$ contained in the lasing mode. This can be done by assigning the noise term to the corresponding demanded dimension which is justified by the homogeneity of Eq. (5.11). As a result, the noise term $\tilde{\eta}'$ is now replaced by $\tilde{\eta}''$ which can also be approximated as a zero mean value Gaussian process with the correlation function

$$\left\langle\tilde{\eta}''(t)\cdot\tilde{\eta}''^{*}(t')\right\rangle=\frac{V_p}{L}\left\langle\tilde{\eta}'(t)\tilde{\eta}'^{*}(t')\right\rangle\equiv R^s\delta(t-t') \tag{7.4}$$

with $R^s=\Gamma\beta K_{tr}K_zR_{sp}V_p=\beta K_{tr}K_zR_{sp}V_a$.

From the complex mode amplitude equation (7.1), the photon number and phase rate equations are readily derived as

$$\frac{dS}{dt}=2\,\mathrm{Re}\left(A^{*}\cdot\frac{dA}{dt}\right)=2\,\mathrm{Re}(p')\cdot S+2\,\mathrm{Re}\left(\tilde{\eta}''\cdot A^{*}\right), \tag{7.5}$$

$$\frac{d\vartheta}{dt}=\mathrm{Im}\left(A^{*}\cdot\frac{dA}{dt}\right)\Big/S=\mathrm{Im}(p')+\mathrm{Im}\left(\tilde{\eta}''\cdot A^{*}\right)/S. \tag{7.6}$$

The mode amplitude $A(t)$ is obtained through the amplification of the spontaneous emission, so that it is not independent from $\tilde{\eta}''(t)$, yielding the ensemble average [47]

$$\left\langle \tilde{\eta}''(t) \cdot A^*(t) \right\rangle = R^s / 2 \tag{7.7}$$

As such, Eq. (7.5) and Eq. (7.6) become

$$\frac{dS}{dt} = 2\operatorname{Re}(p')S + R^s + \tilde{\gamma}^s \ , \tag{7.8}$$

$$\frac{d\vartheta}{dt} = \operatorname{Im}(p') + \tilde{\gamma}^\theta \ , \tag{7.9}$$

where $\tilde{\gamma}^s, \tilde{\gamma}^\theta$ represent the Langevin noise sources, which, under the Markovian assumption, have zero means and satisfy following correlation functions, respectively [103], [104]

$$\left\langle \tilde{\gamma}^s(t) \cdot \tilde{\gamma}^s(t') \right\rangle = 2R^s S(t) \delta(t - t'), \tag{7.10}$$

$$\left\langle \tilde{\gamma}^\theta(t) \cdot \tilde{\gamma}^\theta(t') \right\rangle = \frac{R^s}{2S(t)} \delta(t - t'). \tag{7.11}$$

By utilizing Eq. (5.5), the rate equations of the photon number and phase can be finally derived as

$$\begin{aligned}\frac{dS}{dt} = &\left\{ 2\operatorname{Re}(\xi^{th}) + \upsilon_g \operatorname{Re}\left[\int_0^L \left(\Delta g(z)(1 + j\alpha_m) \mathbf{w}^{th}(z) \bar{\mathbf{\Phi}}^{th}(z) + j\kappa^a(z) \mathbf{w}^{th}(z) \bar{\mathbf{\Phi}}^{th\prime}(z) \right) dz \right] \right\} S \\ &+ R^s + \tilde{\gamma}^s\end{aligned} \tag{7.12}$$

$$\frac{d\vartheta}{dt} = \operatorname{Im}(\xi^{th}) + \frac{1}{2}\upsilon_g \operatorname{Im}\left[\int_0^L \left(\Delta g(z)(1 + j\alpha_m) \mathbf{w}^{th}(z) \bar{\mathbf{\Phi}}^{th}(z) + j\kappa^a(z) \mathbf{w}^{th}(z) \bar{\mathbf{\Phi}}^{th\prime}(z) \right) dz \right] + \tilde{\gamma}^\theta \tag{7.13}$$

with $\Delta g(z)$ denoting the increase of the material power gain from threshold condition.

It is seen that Eqs. (7.12) and (7.13) resemble the form of conventional 0D models, yet taking account of longitudinal variations of the field, gain as well as the coupling strength. The detailed linkage between 0D and 1D model will be discussed in the next section.

7.3 Linkage between 0D and 1D Models

To compare with 0D models, we introduce two effective parameters, namely effective modal gain $\Delta\bar{g}$ and effective modal coupling strength $\bar{k}^a$ of the lasing mode defined as follows

$$\Delta\bar{g} = \Gamma\int_0^L \Delta g(z)\mathbf{w}^{th}(z)\bar{\mathbf{\Phi}}^{th}(z)dz, \tag{7.14}$$

$$\bar{k}^a = \int_0^L j\kappa^a(z)\mathbf{w}^{th}(z)\bar{\mathbf{\Phi}}^{th\prime}(z)dz. \tag{7.15}$$

By this definition, Eqs. (7.12) and (7.13) can be converted into the following form

$$\frac{dS}{dt} = (G-\gamma)\cdot S + R^s + \tilde{\gamma}^s, \tag{7.16}$$

$$\frac{d\vartheta}{dt} = \Delta\omega^1 + \Delta\omega^2 + \tilde{\gamma}^\theta, \tag{7.17}$$

with

G: Effective net rate of stimulated emission of the lasing mode given by

$$G = \upsilon_g\left[\mathrm{Re}(\Delta\bar{g}) - \alpha_m \mathrm{Im}(\Delta\bar{g}) + \mathrm{Re}(\bar{\kappa}^a)\right] \tag{7.18}$$

γ: Effective photon decay rate of the lasing mode given by

$$\gamma = -2\,\mathrm{Re}\left(\xi^{th}\right) \tag{7.19}$$

$\Delta\omega^1$: The change of the lasing frequency at the threshold with respective to the reference frequency ω_0, given by

$$\Delta\omega^1 = \omega^{th} - \omega_0 \tag{7.20}$$

$\Delta\omega^2$: The change of the lasing frequency above threshold given by

$$\Delta\omega^2 = \frac{1}{2}\upsilon_g\left[\mathrm{Im}\left(\Delta\overline{g}\right) + \alpha_m\,\mathrm{Re}\left(\Delta\overline{g}\right) + \mathrm{Im}\left(\overline{\kappa}^a\right)\right] \tag{7.21}$$

For the 0D model, all the longitudinal variations are ignored. If we also make this assumption to our 1D model and neglect the carrier-dependent coupling coefficient, i.e. Δg is assumed to be constant along the laser cavity and $\kappa^a = 0$, the parameters in Eqs. (7.18) and (7.21) then become

$$G = \upsilon_g\,\mathrm{Re}\left(\Delta\overline{g}\right) = \upsilon_g \Delta g\,, \tag{7.22}$$

$$\Delta\omega^2 = \frac{1}{2}\upsilon_g \alpha_m\,\mathrm{Re}\left(\Delta\overline{g}\right) = \frac{1}{2}\upsilon_g \alpha_m \Delta g\,. \tag{7.23}$$

As such, the 1D model will fully reduce to the 0D models shown in [5], [47].

In system level modeling, 0D models are widely used. They have been implemented as equivalent circuits to be numerically solved by SPICE or in hardware description languages in electro-optical system design [105], [106]. Another application example of 0D models is based on the input/output buffer information specification (IBIS) where the dynamic behaviors are described by means of tabulated parameters [9],

[107]. In all of these applications, the parameter extractions are rather important as they dictate the accuracy of the model. Once the linkage of these parameters between 0D and 1D models is built, we may gain an insight as to how those phenomenologically induced parameters are dependent on the material, structural and operational parameters. Moreover, those analytical expressions of important laser characteristics, such as relaxation oscillation frequency, damping rate, etc., can also be derived in equivalent forms with the longitudinal non-uniformities included. This should be practically meaningful, especially to system designers.

7.4 Summary

In this chapter, single-mode rate equations for the photon number and phase are derived from the photon wave rate equations previously proposed. The resulting equations are presented in a similar form to the 0D behavior model, with considering any longitudinal non-uniformity of the parameters. The linkage between 0D and 1D model, i.e. the system level modeling and device level modeling, is built to gain a deeper insight into the parameter dependence of the device.

Chapter 8

Single-Mode Dispersive Grating DFB Lasers

8.1 Introductions

"Spectral purity" of the semiconductor laser, e.g. single-longitudinal-mode operation, is often required to reduce effects of fiber group-velocity dispersion [18] and hence allow longer reach with low error rate in fiber-optic communications. A narrow spectral width for a laser diode is also desired to enhance the transmission capacity of the networks where wavelength-division-multiplexing (WDM) systems [108] are applied. One of the dominant structures being widely used is the DFB laser. The uniform index-coupled DFB lasers with perfectly AR coated facets have the intrinsic drawback of the two degenerate modes spectrally symmetric with respect to the Bragg frequency [19]. Although, this degeneracy may be lifted by introducing facet asymmetry, the yield is hard to control due to the random facet phases [109]. A $\lambda/4$-shifted grating can break this degeneracy, leading to the single-mode operation at the Bragg wavelength [20]. However, with the increase of κL, quantum efficiency decreases and also the photon/carrier distributions become highly non-uniform along the laser cavity, known as the spatial hole burning effects, causing a reduced side-mode suppression [39]. Another solution is the introduction of the complex coupling, i.e., the gain (or loss)-coupled DFB laser. Various degrees of gain (or loss) coupling have been investigated [19], [21], [110]. It was shown that there will not be any degeneracy problem for purely gain-coupled DFB lasers and the lasing mode is locating exactly at the Bragg wavelength for devices with AR coated facets. The complex-coupled DFB laser will also introduce a large enough threshold gain difference to two otherwise degenerate modes, leading to the single-mode operation (either at longer wavelength mode or shorter wavelength mode). However, saturation instabilities may occur for loss gratings [111] and the gain coupling is highly dependent on the carrier density which varies greatly with current injection level for gain gratings [93]. Complex dynamics for this type of lasers needs careful modeling.

For a normal index-coupled grating, we found that if the dispersion curves of the materials constituting the high and low index region are different, the coupling strength between two counter propagating waves becomes wavelength dependent. We call such gratings “dispersive gratings”. It is found that, for the conventional uniform-grating DFB laser, the degeneracy of the two modes symmetric to the Bragg wavelength will be lifted due to this new wavelength selection mechanism. This design idea is first proposed in [P.7]. In this chapter, this novel DFB laser design is introduced and analyzed by using the previously proposed modeling technique.

8.2 Theoretical Framework for Existing Gratings

For conventional uniform-grating DFB laser with both facets AR-coated, we can obtain the threshold gain constant α and the detuning δ of the corresponding propagation constant through the following transcendental equation [19]

$$\alpha - j\delta = \gamma \cosh\gamma L / \sinh\gamma L \tag{8.1}$$

with the complex propagation constant γ obeying

$$\gamma^2 = \left(\alpha - j\delta\right)^2 + \kappa^2 \tag{8.2}$$

For the index-coupled DFB lasers, κ is a real number, i.e. $\kappa = \kappa^*$. Taking complex conjugate on both sides of Eq. (8.1) and Eq. (8.2), we obtain

$$\alpha + j\delta = \gamma^* \left(\cosh\gamma^* L / \sinh\gamma^* L\right) \tag{8.3}$$

with

$$\left(\gamma^*\right)^2 = \left(\left(\alpha - j\delta\right)^2\right)^* + \left(\kappa^2\right)^* = \left(\alpha + j\delta\right)^2 + \kappa^2 . \tag{8.4}$$

It is seen that if (α, δ) is a solution set, $(\alpha, -\delta)$ is also a solution set, which means that for any lasing wavelength we obtain with detuning δ and threshold gain α, there is always an accompanying lasing wavelength at detuning $-\delta$ with the identical threshold gain. From Eq. (8.1) and Eq. (8.2), we have

$$\sqrt{\gamma^2 - \kappa^2} = \gamma \cosh\gamma L / \sinh\gamma L . \tag{8.5}$$

We further notice that $\delta = 0$ cannot be a solution of the above lasing condition since a real γ (due to $\delta = 0$ in Eq. (8.2)) makes the left hand side of Eq. (8.5) smaller than γ whereas the right hand side larger than γ. As a result, the conventional DFB laser with uniform index-coupled grating can never achieve single mode operation at Bragg wavelength and has dual-mode operation due to the threshold gain degeneracy at two different lasing wavelengths symmetrically located at two sides of the Bragg wavelength.

Based on such understandings, we further deduce that, for complex-coupled DFB lasers in which κ becomes a complex number, i.e. $\kappa \neq \kappa^*$, the fact (α, δ) is a solution set does not necessarily lead to the conclusion that $(\alpha, -\delta)$ is also a solution set of Eq. (8.1) since Eq. (8.4) is no longer valid. Consequently, the original degeneracy is broken for complex coupling coefficients. For purely gain (or loss)-coupled DFB lasers, κ is an imaginary number. $\delta = 0$ can thus be a solution since both sides of Eq. (8.5) are larger than the real γ now. As such, single-mode operation is achieved at the Bragg wavelength. Another widely employed method for forcing the DFB laser to lase at the Bragg wavelength is to add an extra section of quarter wavelength in between two uniform-grating sections, i.e., $\lambda/4$-shifted DFB lasers, where the solution set is however not obtained through searching the roots of Eq. (8.1) directly.

8.3 Dispersive Gratings

The uniform index-coupled DFB laser using a dispersive grating is introduced in this section as an alternative method to break the inherent degeneracy as follows

$$\kappa = \kappa_0 + \eta\delta \tag{8.6}$$

where κ_0 is the "background" coupling strength and η the detuning coefficient. Assume the grating is formed through periodic change between the index n_1 of the high index region and n_2 of the low index region, and

$$n_{1(2)} = n_{10(20)} + \frac{dn_{1(2)}}{d\lambda}(\lambda - \lambda_0), \tag{8.7}$$

with n_{10}, n_{20} denoting the effective index of high and low index region at Bragg wavelength respectively, and $dn_1/d\lambda \neq dn_2/d\lambda$. An illustration of such an arrangement is shown in Figure 8.1.

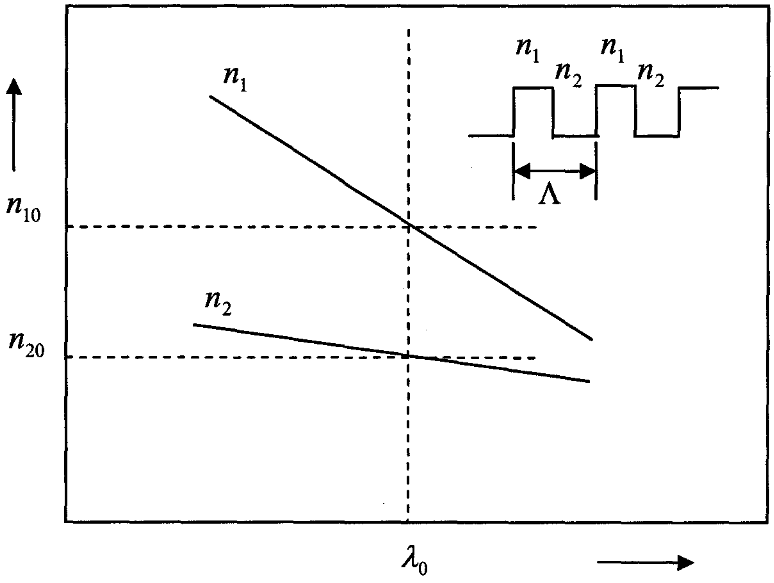

Figure 8.1 Illustration of a dispersive grating with $n_{10} \neq n_{20}$, $dn_1/d\lambda \neq dn_2/d\lambda$

The coupling coefficient [19] of this dispersive grating can be calculated by

$$\kappa = (\frac{\pi}{\lambda})(n_1 - n_2). \tag{8.8}$$

By using Eqs. (8.6) to (8.8) and utilizing $\delta = 2\pi n_{eff}/\lambda - \pi/\Lambda$ and $\lambda_0 = 2n_{eff}\Lambda$, we obtained

$$\kappa_0 \equiv (\frac{\pi}{\lambda})(n_{10} - n_{20}), \tag{8.9}$$

$$\eta \equiv -[d(n_1 - n_2)/d\lambda]\Lambda. \tag{8.10}$$

It is seen from Eq. (8.10) that η in quantity is the effective index dispersion difference within one grating period. By the definition of Eq. (8.6), κ remains real, however it changes with δ as illustrated in Figure 8.2. A different threshold gain α is obtained for the two otherwise degenerate modes due to the selectivity of the coupling coefficient with respective to the wavelength, leading to single mode operation.

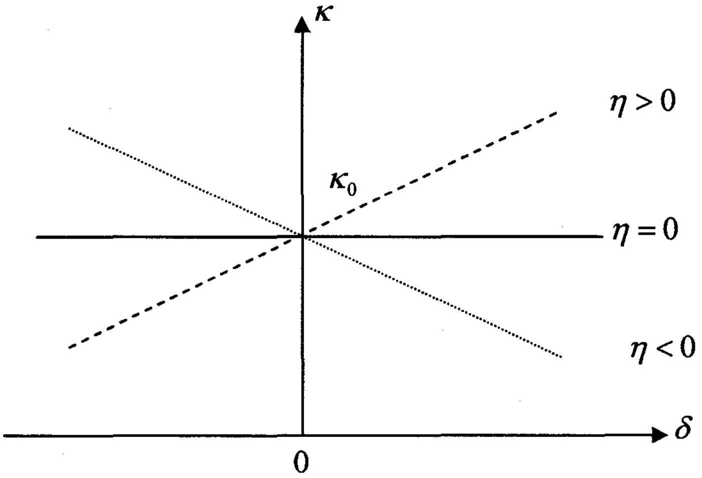

Figure 8.2 Illustration of the dispersive coupling coefficient with $\eta > 0$ (dashed line) or $\eta < 0$ (dotted line) and the conventional wavelength independent coupling coefficient with $\eta = 0$ (solid line)

The grating dispersion is generated by introducing non-equal effective index dispersions in the two different sections of every grating period. Basically, there are two ways to realize the dispersive effective indices. One is through waveguide dispersion; the other is through material dispersion. One possible realization method is to apply the electromagnetically induced transparency (EIT) [112], [113], where the index corrugation is not formed by the periodic variation of semiconductor materials with different effective indexes. Rather, they are generated by the coherent processes associated with the interaction of an intense IR laser beam with a corrugated quantum well (QW) structure.

The structure view is shown in Figure 8.3 (a) and one simulation example is shown in Figure 8.3 (b), which indicates a detuning coefficient of $\sim -12\%$ with an incident beam of $0.7\,\mathrm{mW/cm^2}$. However, we may notice from Figure 8.3 that the related wavelength in this example is not in the telecom wavelength band. If semiconductor materials with significant conduction band offsets are used, such as InGaAs/AlAsSn, the wavelength region may be extended to $1.5\,\mu\mathrm{m}$. But this still is an open research topic.

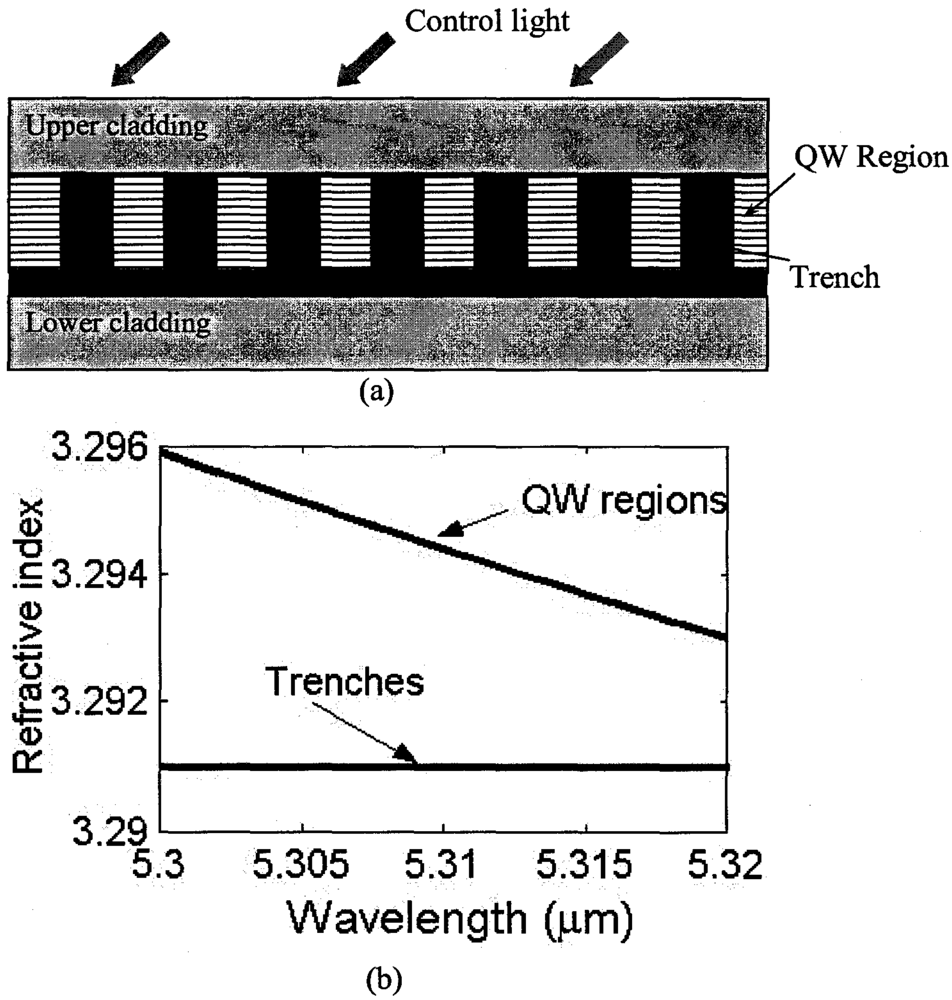

Figure 8.3 (a) Schematic view of Electromagnetically Induced Transparency;
(b) Variations of refractive indices of QW regions and trenches with wavelength

* Figure 8.3 is calculated by Dr. Seyed M. Sadeghi

8.4 Simulation Results

1) Threshold Analysis

The devices under investigation in this section are the dispersive grating DFB lasers with $\kappa_0 \neq 0$. Figure 8.4 (a), (b) show the threshold condition (α,δ) of two dispersive grating designs with $\kappa L = 2$ and $\kappa L = 4$, respectively. Cases with different detuning coefficient are investigated, i.e. $\eta = 5\%, 10\%$ (square, star) and $\eta = -5\%, -10\%$ (circle, triangle). Threshold conditions of conventional DFB lasers $(\eta = 0)$ with the same normalized coupling strengths are also plotted (cross) for the purpose of comparison. It is observed from Figure 8.4 that there is only one mode at one side of the stopband edge that takes the lowest threshold gain with either positive η or negative η. If $\eta > 0$, the coupling strength for the (+1) mode at the right hand side of the centre frequency increases, leading to a lower threshold gain; while that for the (-1) modes decreases, causing a higher threshold gain due to a negative δ. Also, we noticed from Figure 8.4 that both a larger η and a smaller $\kappa_0 L$ will help to increase the gain margin between (+1) and (-1) modes.

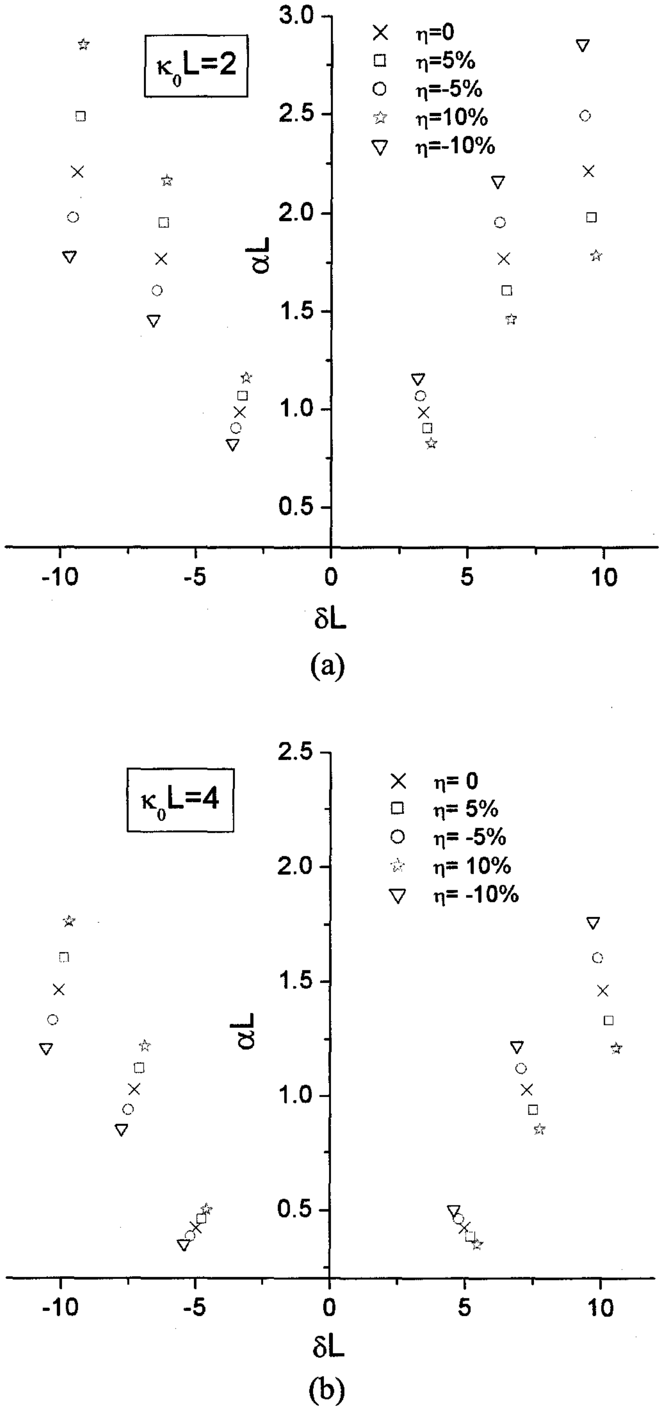

Figure 8.4 Threshold condition of dispersive grating DFB lasers with different η under normalized background coupling strength (a) $\kappa_0 L = 2$ and (b) $\kappa_0 L = 4$

To further examine the impact of η and $\kappa_0 L$ on the gain margin which normally is an indication of the single-mode operation, we define the relative change of the coupling strength as

$$\xi = \frac{\eta\delta}{\kappa_0}. \tag{8.11}$$

Figure 8.5 shows the change of the magnitude of the normalized gain margin with the magnitude of ξ for the different detuning coefficients. According to T. L. Koch et al. [114] a normalized gain/loss margin in excess of $|\Delta\alpha L| \sim 0.015$ is necessary to achieve a 25dB side mode suppression ratio (SMSR) for typical laser parameters under CW operation. While for dynamic single mode operation of intensity modulated lasers, the typical normalized gain/loss margin of 0.15 is desired to achieve a SMSR of ~25dB. We here take $|\Delta\alpha L| = 0.2$ as our single mode operation criterion. It is observed from Figure 8.5 that $\xi > 0.1$ is required for $|\eta| = 5\%$. This actually corresponds to $\kappa_0 L \leq 2$ from Eq. (8.11). If a larger $|\eta|$ is applied, the constraint on $\kappa_0 L$ will be greatly relaxed. Figure 8.6 shows the transmission spectrum of a typical dispersive grating DFB laser design with $\kappa_0 L = 2$, $\eta = \pm 5\%$. It is clearly shown that the (+1) mode is favored if $\eta = +5\%$, while the (-1) mode is selected if $\eta = -5\%$. This is obviously attributed to the threshold gain discrimination brought by the grating coupling strength dependence on the detuning, as we previously analyzed.

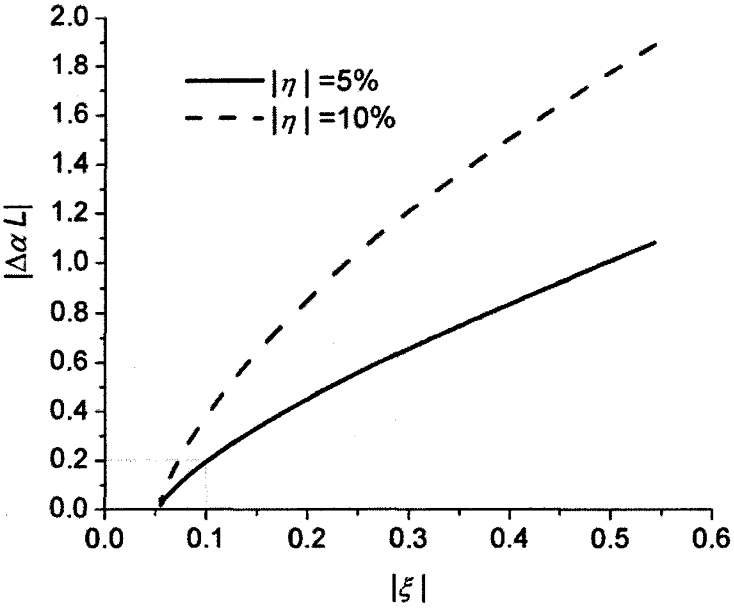

Figure 8.5 Change of the magnitude of the normalized gain margin with that of the relative change of the coupling strength for different detuning coefficients

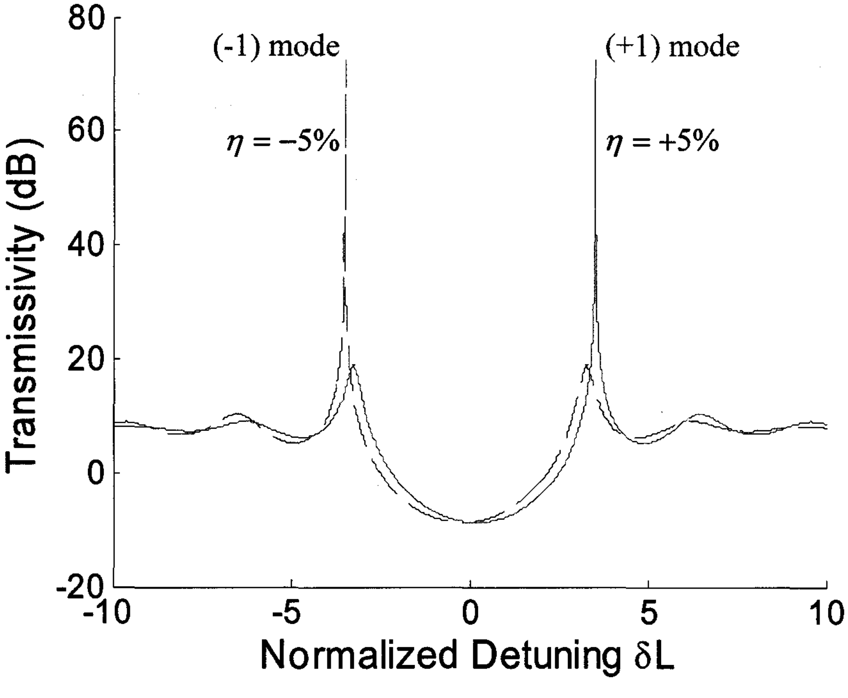

Figure 8.6 Transmission spectrum of the dispersive grating DFB laser with $\eta = 5\%$ (solid line) and $\eta = -5\%$ (dashed line)

2) Above Threshold Analysis by Using the SWM-CCM

With the eigen-solutions obtained through the threshold analysis, the above threshold performances of the dispersive grating DFB lasers can be investigated by the standing wave model based on "cold" cavity modes proposed in chapter 4. The device being simulated has the normalized background coupling coefficient of $\kappa_0 L = 2$ and the detuning coefficient of $\eta = +5\%, -5\%$ or 0, corresponding to cases where the dispersive κ with positive slope, negative slop or non-dispersive κ (see illustration in Figure 8.2). The injection current of the laser is 50mA and the two facets of the laser are AR-coated. Other laser parameters are listed in Table 4.1.

The CW optical spectrum is obtained by Fourier transforming the optical field samples produced by the SWM-CCM time-domain model after the transient has settled down. The results are shown in Figure 8.7 (a), (b) and (c) for three different detuning coefficients, respectively. The corresponding output power evolutions of (+1) and (-1) modes are also depicted in the insets of the Figure 8.7. It is observed that the conventional uniform-grating DFB laser suffer the intrinsic demerit of the dual-mode lasing. The dispersive grating DFB laser with positive detuning coefficient will lead to the lasing of (+1) mode with (-1) mode being greatly suppressed. The situation for negative detuning coefficient reverses.

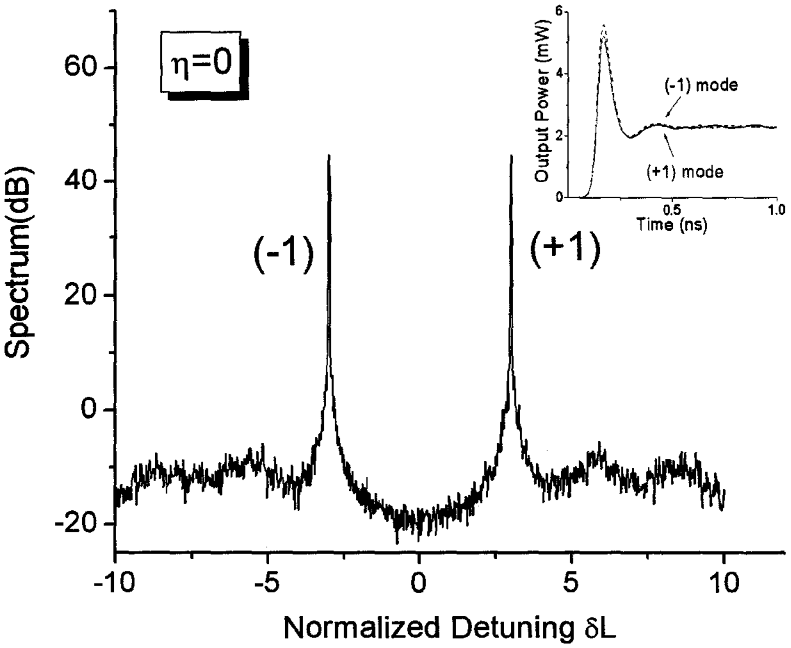
η=0
Spectrum(dB)
60
40
20
0
-20
(-1)
(+1)
-10
-5
0
5
10
Normalized Detuning δL
Output Power (mW)
0
2
4
6
(-1) mode
(+1) mode
0.5
1.0
Time (ns)

(a)

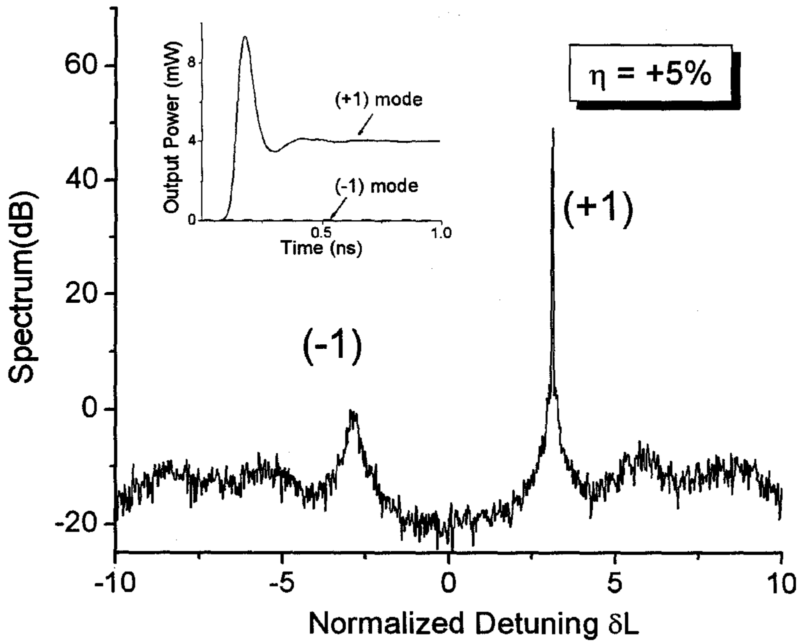
η = +5%
Spectrum(dB)
60
40
20
0
-20
(-1)
(+1)
-10
-5
0
5
10
Normalized Detuning δL
Output Power (mW)
0
4
8
(+1) mode
(-1) mode
0.5
1.0
Time (ns)

(b)

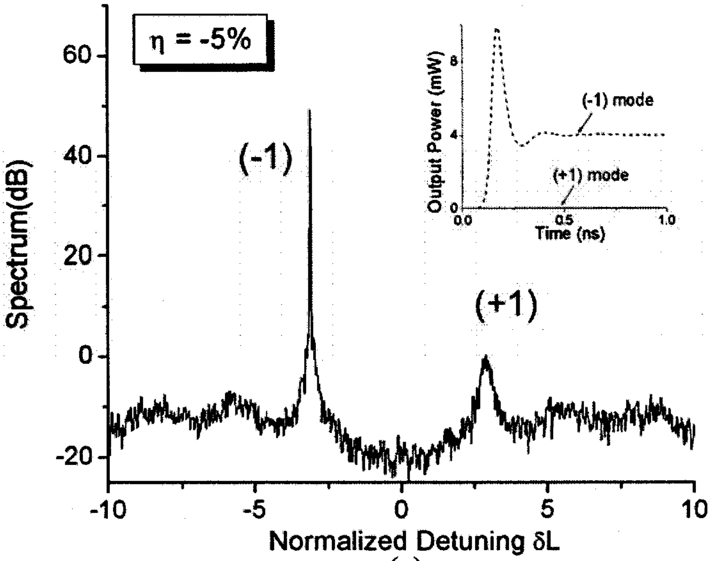

(c)

Figure 8.7 Optical spectrum of (a) the conventional uniform-grating DFB laser ($\eta = 0$) (b) the dispersive grating DFB laser with $\eta = +5\%$ and (c) the dispersive grating DFB laser with $\eta = -5\%$; The insets show the evolutions of the output power for (+1) and (-1) modes for three cases respectively.

8.5 Discussions

In the last section, we consider the dispersive grating structure with the background coupling strength $\kappa_0 \neq 0$ and both facets AR-coated. It is naturally interesting to explore what performances the structure will have if $\kappa_0 = 0$ at the Bragg wavelength λ_0. Both facets are as cleaved in this case. As such, the propagating waves see no reflections from the grating at λ_0 except for the reflection from the facets. An illustration of this structure is shown in Figure 8.8. To include the effects of reflections from two facets, the transcendental equation (4.12) is used. The corresponding threshold conditions for the cases of $\eta > 0$ and $\eta < 0$ are calculated and shown in Figure 8.9. The results for $\eta = 0$ are also added for comparison, which actually indicate the conventional FP cavity modes since reflections only come from two facets for the whole wavelength range. Also, for all cases of the different values of η, the modes at the Bragg wavelength are overlapped due to $\delta = 0$. It is observed in Figure 8.9 that if $\eta > 0$, the central mode (at Bragg wavelength) bears the highest threshold gain, while the threshold gains of other modes are almost indistinguishable, which is absolutely not a candidate for single-mode lasers. However, if $\eta > 0$, the central mode has the lowest threshold gain which indicates the possible realization of a single-mode laser. It is also shown that a detuning coefficient of -30% is required to achieve a gain margin of~ 0.2 in this case. Figure 8.10 shows the transmission spectrum for this structure. We observe from Figure 8.9 that the performance of this structure is quite sensitive to the phase of the detuning coefficient η. This may be a problem for utilizing this structure for practical applications and therefore warrants further investigations. One possible solution is to add an adjustable phase section to compensate for the phase variation.

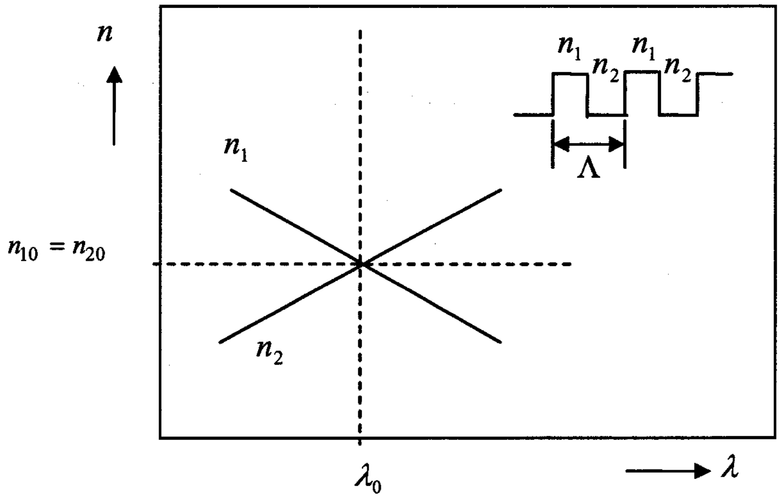

Figure 8.8 Illustration of a dispersive grating with $n_{10} = n_{20}$, $dn_1 / d\lambda \neq dn_2 / d\lambda$

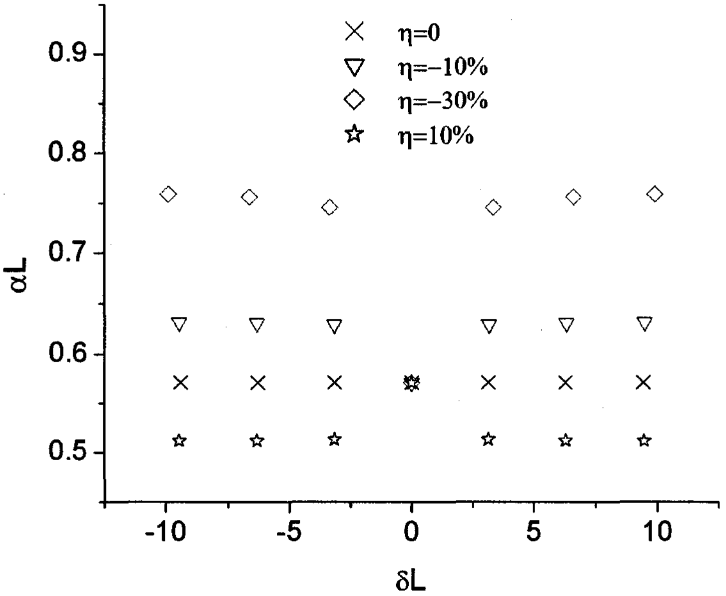

Figure 8.9 Threshold condition of dispersive grating DFB lasers with different η under $\kappa_0 L = 0$

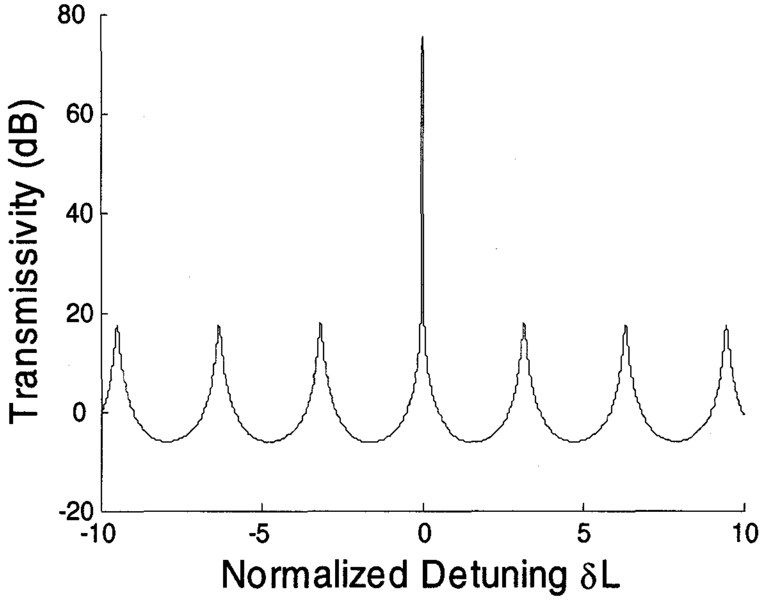

Figure 8.10 Transmission spectrum of the dispersive grating DFB laser with $\eta = -10\%$ under $\kappa_0 L = 0$

8.6 Conclusions

This chapter presents a novel DFB laser by incorporating a dispersive grating, whose coupling strength is dependent on the operating wavelength. Analysis of the laser threshold conditions shows that the proposed structure guarantees single-mode operation due to the inherent threshold gain discrimination on the two otherwise degenerate lasing modes. The design concept is then successfully verified by the simulation example using the standing wave model developed in chapter 4. We therefore concluded that the dual-mode operation problem in the conventional uniform-grating DFB laser can be cured by the dispersive grating without resorting to the existing methods such as quarter-wave-shifted or complex-coupled gratings.

Chapter 9

Conclusions and Future Work

9.1 Summary of Contributions

This thesis has mainly focused and contributed on the development and demonstration for a set of new standing-wave laser diode numerical models and associated simulation methods and the analysis of a novel laser diode design based on the dispersive grating. We have systematically investigated and advanced the state-of-the-art for one-dimensional (1D) models of DFB lasers. By expanding the laser field in terms of modes of "cold" cavity and threshold "hot" cavity respectively, we have established two new standing-wave formulations for which the more efficient time-domain simulation can be implemented. The common merit of them is that the eigenmodes are obtained at the fixed reference point and only need to be searched once as a priori knowledge. The accuracy and efficiency of the model and simulation methods are demonstrated and validated by simulation of typical DFB lasers with index or gain couplings. These models will find their promising applications in the device design and optimizations where the computation time is of concern. It is worth mentioning that the proposed numerical models are aiming at simulating DFB lasers, however they are not only limited to this type of laser.

Further, the new standing-wave formulation resembles the form of the conventional zero-dimensional (0D) rate equation models that are widely used for design and simulation of optical systems. Derived from a more rigorous one-dimensional model, the resulting rate equations account for longitudinal optical and carrier non-uniformity and lend to more intuitive and revealing linkage to the structural, material, as well as operational parameters of the laser diode. As such, this rate equation model is expected to provide system designers with an accurate simulation tool to understand and predict the laser performances.

Finally, a novel design of dispersive grating DFB laser has been analyzed by using the modeling techniques developed in this thesis. The new design is expected to greatly increase the yield of the conventional uniform-grating DFB laser.

The major contributions of this thesis are summarized as follows and corresponding publications can be found in Appendix C.

1. Based on the Suzuki's fractal decomposition approach, a high-order split-step traveling wave model has been developed and it is shown to be more efficient than the conventional split-step method [P.5].
2. An efficient standing wave model based on "cold" cavity modes expansion has been developed for simulating index-coupled DFB lasers [P.3]. The single-section DFB structure, e.g. the uniform-grating DFB laser [P.8] and the multi-section structure, e.g. the $\lambda/4$-shifted DFB laser [P.6] have been investigated. The scope of validity has been discussed and the efficiency of the model has been demonstrated through comparing with the traveling wave model.

3. An efficient standing wave model based on threshold "hot" cavity modes expansion has been developed for simulating gain-coupled DFB lasers [P.1]. The current-dependent coupling strength is taken into account in this model. The complexity and efficiency of this model are shown to be almost at the same level with the standing wave model based on "cold" cavity modes.
4. A more efficient solution scheme to the previously proposed standing wave models has been presented where an approximation is made on the time-dependent carrier density distribution [P.2]. The complexity of the standing wave models previously proposed are greatly reduced in cases where the assumption is valid.
5. Photon number and phase rate equations are derived from the proposed standing wave model with the attemption to establish the linkage between 0D model and 1D model of DFB lasers and provide system designers an accurate simulation tool.
6. A single-longitudinal-mode DFB laser is firstly designed and analyzed based on a dispersive-grating DFB structure proposed in [P.7]. The previously proposed standing wave model is applied as an evaluation tool. Simulation results show that the threshold gain difference is introduced to the two otherwise degenerate modes of the uniform-grating DFB laser, leading to the single mode operation [P.4].

9.2 Suggestions for Future Research

Based on the research work done in this thesis, following topics are worth further study:

1. In chapter 6, the approximation to the carrier density distribution is valid if the optical power is moderate. Other approximation strategies exist when the optical power is relatively large, which has been briefly discussed at the end of chapter 6. However, further careful investigation on this topic is still necessary such that a more efficient solution to the standing wave model will be also available for the large optical power case.

2. To establish the relation of parameters between 0D and 1D model of DFB lasers is of practical significance to system designers. Chapter 7 makes an attempt to build such linkage through theoretical derivation. More detailed research work on this topic can be explored. For example, with the help of such linkage, the dependence of those phenomelogically induced parameters in 0D model on the structure, material parameters and operation conditions can be studied in detail.

Bibliography

[1] T. Yamanaka, S. Seki, and K. Yokoyama, "Numerical analysis of static wavelength shift for DFB lasers with longitudinal mode spatial hole burning," *IEEE Photon. Technol. Lett.*, vol. 7, pp. 610–612, 1991.

[2] H. J. Wunsche, U. Bandelow, and H. Wenzel, "Calculation of combined lateral and longitudinal spatial hole burning in $\lambda/4$ shifted DFB lasers," *IEEE J. Quantum Electron.*, vol. 29, no. 6, pp. 1754–1760, 1993.

[3] X. Li, A. D. Sadovnikov, W.-P. Huang, and T. Makino, "A physics based three-dimensional model for distributed feedback laser diodes," *IEEE J. Quantum Electron.*, vol. 34, no. 9, pp. 1545–1553, 1998.

[4] A. Champagne, R. Maciejko, D. M. Adams, G. Pakulski, B. Takasaki, and T. Makino, "Global and local effects in gain-coupled multiple-quantum-well DFB lasers," *IEEE J. Quantum Electron.*, vol. 35, no. 10, pp. 1390–1401, 1999.

[5] G. P. Agrawal and N. K. Dutta, *Semiconductor Lasers.* New York, U.S.A.: Van Nostrand Reinhold, 1993.

[6] D. Marcuse, and T.-P. Lee, "On approximate analytical solutions of rate equations for studing transient spectra of injection lasers," *IEEE J. Quantum Electron.*, vol. 19, no. 9, pp. 1397–1406, 1983.

[7] D. Welford, "A rate equation analysis for the frequency chirp to modulated power ratio of a semiconductor diode laser," *IEEE J. Quantum Electron.*, vol. 21, pp. 1749–1751, 1985.

[8] C.-H. Lee, and S.-Y. Shin, “Transformation of rate equations and approximate transient solutions for semiconductor lasers,” *IEEE J. Quantum Electron.*, vol. 25, no. 5, pp. 878–881, 1989.

[9] G. Clarici, and E. Griese, “Analytical laser model for system-level simulation”, *IEEE/OSA J. Lightwave Tech.*, vol. 25, no.4, pp. 1070-1076, 2007.

[10] P. Vankwikelberge, G. Morthier, and R. Baets, “CLADISS—A longitudinal multimode model for the analysis of the static, dynamic, and stochastic behaviour of diode lasers with distributed feedback,” *IEEE J. Quantum Electron.*, vol. 26, no. 10, pp. 1728–1741, 1990.

[11] B. Tromborg, H. Olesen, and X. Pan, “Theory of linewidth for multielectrode laser diodes with spatially distributed noise sources,” *IEEE J. Quantum Electron.*, vol. 27, no. 2, pp. 178–192, 1991.

[12] L. M. Zhang and J. E. Carroll, “Large-signal dynamic model of the DFB laser,” *IEEE J. Quantum Electron.*, vol. 28, no. 3, pp. 604–611, 1992.

[13] A. J. Lowery, A. Keating, and C. N. Murtonen, “Modeling the static and dynamic behavior of quarter-wave-shifted DFB lasers,” *IEEE J. Quantum Electron.*, vol. 28, no. 9, pp. 1874–1883, 1992.

[14] T. Makino, H. Lu, and G. P. Li, “Transfer-matrix dynamic model of partly gain-coupled 1.55 μm DFB lasers with a strained-layer MQW active grating,” *IEEE J. Quantum Electron.*, vol. 30, no. 11, pp. 2443–2448, 1994.

[15] R. Nagarajan, M. Ishikawa, T. Fudushima, R. S. Geels, and J. E. Bowers, "High speed quantum-well lasers and carrier transport effects," *IEEE J. Quantum Electron.*, vol. 28, pp. 1990–2007, 1992.

[16] S. F. Yu, R. G. S. Plumb, L. M. Zhang, M. C. Nowell, and J. E. Carroll, " Large-signal dynamic behavior of distributed feedback lasers including lateral effects," *IEEE J. Quantum Electron.*, vol. 30, pp. 1740–1750, 1994.

[17] L. V. T. Nguyen, A. J. Lowery, P. C. R. Gurney, and D. Novak, "A time-domain model for high-speed quantum well lasers including carrier transport effects," *IEEE J. Sel. Top. Quantum Electron.*, vol. 1, no. 2 pp. 494-504, 1995.

[18] W. A. Gambling, H. Matsumura, and C. M. Ragdale, "Total dispersion in graded index single-mode fibers," *Electron. Lett.*, vol. 15, pp. 474-476, 1979.

[19] H. Kogelnik and C. V. Shank, "Coupled-wave theory of distributed feedback lasers," *J. Appl. Phys.*, vol. 43, no. 5, pp. 2327-2335, May 1972.

[20] H. A. Haus and C. V. Shank, "Antisymmetric taper of distributed feedback lasers," *IEEE J. Quantum Electron.*, vol. 12, pp. 532-539, 1976.

[21] E. Kapon, A. Hardy, and A. Katzir, "The effects of complex coupling coefficients on distributed feedback lasers," *IEEE J. Quantum Electron.*, vol. 18, pp. 66-71, 1982.

[22] R. N. Hall, G. E. Fenner, J. D. Kingsley, T. J. Soltys, and R. O. Carlson, "Coherent light emission from GaAs junctions," *Phys. Rev. Lett.*, vol.9, no. 9, pp.366-368, 1962.

[23] M. I. Nathan, W. P. Dumke, G. burns, F. H. Dill, Jr., and G. Lasher, "Stimulated emission of radiation from GaAs p-n junctions," *Appl. Phys. Lett.*, vol.1, no. 3, pp.62-64, 1962.

[24] T. M. Quist, R. H. Rediker, R. J. Keyes, W. E. Krag, B. Lax A. L. McWhorter, and H. J. Zeiger, "Semiconductor maser of GaAs," *Appl. Phys. Lett.*, vol.1, no. 4, pp.91-92, 1962.

[25] N. Holonyak, Jr., and S. F. Bevacqua, "Coherent (visible) light emission from $Ga(As_{1-x}P_x)$ junctions," *Appl. Phys. Lett.*, vol.1, no. 4, pp.82-83, 1962.

[26] I. Hayashi, M. B. Panish, P. W. Foy, and S. Sumski, "Junction lasers which operate continuously at room temperature," *Appl. Phys. Lett.*, vol.17, no. 3, pp.109-111, 1970.

[27] Zh. I. Alferov, V. M. Andreev, D. Z. Garbuzov, Yu. V. Zhilyaev, E. P. Morozov, E. L. Portnoi, and V. G. Trofim, "Investigation of the influence of heterostructure parameters on the threshold current of lasers and obtaining a cw lasing regime at room temerature," *Fiz. Tekh. Poluprovodn.* vol. 4, pp.1826-1830, 1970.

[28] Zh. I. Alferov, V. M. Andreev, E. L. Portnoi, and M. K. Trukan, "AlAs-GaAs heterojunction injection lasers with a low room temperature threshold," *Sov. Phys. Semicond.*, vol. 3, pp.1107-1110, 1970.

[29] J. C. Cartledge, and R. C. Srinivasan, "Extraction of DFB laser rate equation parameters for system simulation purposes," *IEEE/OSA J. Lightwave Tech.*, vol. 15, no.5, pp. 852-860, 1997.

[30] J. Gao, X. Li, J. Flucke, and G. Boeck, "Direct parameter-extraction method for laser diode rate-equation model," *IEEE/OSA J. Lightwave Tech.*, vol. 22, no. 6, pp. 1604-1609, 2004.

[31] T. Ohtoshi, K. Yamaguchi, C. Nagaoka, T. Uda, Y. Murayama, and N. Chinone, "A two-dimensional device simulator of semiconductor lasers," *Solid State Electron.*, vol. 30, pp. 627-638, 1987.

[32] G.-L. Tan, N. Bewtra, K. Lee, and J. M. Xu, "A two-dimensional nonisothermal finite element simulation of laser diodes," *IEEE J. Quantum Electron.*, vol. 29, no. 3, pp. 822–835, 1993.

[33] M. Grupen and K. Hess, "Simulation of carrier transport and nonlinearities in quantum well laser diodes," *IEEE J. Quantum Electron.*, vol. 34, no. 1, pp. 120-140, 1998.

[34] H.-J. Wunsche, H. Wenzel, U. Bandelow, J. Piprek, H. Gajewski and J. Rehberg, "2D modeling of distributed feedback semiconductor lasers," *Simulation of Semiconductor Devices and Processes*, W. Fichtner, Ed. Zurich: D. Aemmer, vol. 4, pp. 65-70, 1991.

[35] K. Yokoyama, T. Yamanada, and S. Seki, "Two-dimensional numerical simulator for multielectrode distributed feedback laser diodes," *IEEE J. Quantum Electron.*, vol. 29, pp. 856-863, 1993.

[36] A. D. Sadovnikov, X. Li, and W.-P. Huang, "A two-dimensional DFB laser model accounting for carrier transport effects," *IEEE J. Quantum Electron.*, vol. 31, no. 10, pp. 1856-1862, 1995.

[37] A. M. Sarangan, W.-P. Huang, G. P. Li, and T. Makino, "A ridge waveguide DFB laser model including transverse carrier and optical effects," *IEEE J. Quantum Electron.*, vol. 32, no. 3, pp. 408–416, 1996.

[38] G. P. Agrawal, *Fiber-optic Communication Systems*, 2nd Edition, New York: John Wiley & Sons, 1997.

[39] H. Soda, Y. Kotaki, H. Ishikawa, S. Yamma-koshi, and H. Imai, "Stability in single longitudinal mode operation in GaInAs/InP phase-adjusted DFB lasers," *IEEE J. Quantum Electron.*, vol. 23, no. 6, pp. 804–814, 1987.

[40] J. E. A. Whiteaway, B. Garrett, G. H. B. Thompson, A. J. Collar, C. J. Armistead, and M. J. Fice, "The static and dynamic characteristics of single and multiple phase-shifted DFB laser structures", *IEEE J. Quantum Electron.*, vol. 28, no. 5, pp. 1272–1293, 1992.

[41] X. Li and W.-P. Huang, "Simulation of DFB semiconductor lasers incorporating thermal effects," *IEEE J. Quantum Electron.*, vol. 31, no. 10, pp. 1848–1855, 1995.

[42] W. Li, X. Li and W.-P. Huang, "A traveling-wave model of laser diodes with consideration for thermal effects," *Optical and Quantum Electronics*, vol. 36, pp. 709-724, 2004.

[43] J. Carroll, J. Whiteaway, and D. Plumb, *Distributed Feedback Semiconductor Lasers*. London, U.K.: IEE Press, 1998.

[44] R. Bonello and I. Montrosset, “Analysis of multisection and multielectrode semiconductor lasers,” *IEEE/OSA J. Lightwave Tech.*, vol. 10, no. 12, pp. 1890-1900, 1992.

[45] A. M. Shams-Zadeh-Amiri, W. Li and X. Li, “Above-threshold spectrum of the radiation field in surface-emitting DFB lasers,” *IEEE J. Quantum Electron.*, vol. 43, no. 1, pp. 31-41, 2007.

[46] K. David, G. Morthier, P. Vankwikelberge, R. G. Baets, T. Wolf and B. Borchert, “Gain-coupled DFB lasers versus index-coupled and phase-shifted DFB lasers: a comparison based on spatial hole burning corrected yield,” *IEEE J. Quantum Electron.*, vol. 27, no. 6, pp. 1714-1719, 1991.

[47] K. Pertermann, *Laser Diode Modulation and Noise*, Dordrecht, Netherlands, Kluwer Academic Publishers, 1991.

[48] C. H. Henry, R. A. Logan, and F. R. Merritt, “Measurement of gain and absorption spectra in AlGaAs buried heterostructure lasers,” *J. Appl. Phys.*, vol. 51, pp. 3042, 1980.

[49] M. Asada, and Y. Suematsu, “The effects of loss and nonradiative recombination on the temperature dependence of threshold current in 1.5-1.6 μm GalnAsP/InP lasers,” *IEEE J. Quantum Electron.*, vol. 19, no. 6, pp. 917-923, 1983.

[50] T. A. Detemple and C. M. Herzinger, “On the semiconductor laser logarithmic gain-current density relation,” *IEEE J. Quantum Electron.*, vol. 29, no. 5, pp. 1246-1252, 1993.

[51] V. Lucarini, J. J. Saarinen, K.-E. Peiponen, and E. M. Vartiainen, *Kramers-Kronig Relations in Optical Materials Research*, Heidelberg: Springer, 2005.

[52] H. Ghafouri-Shiraz and B. S. K. Lo, *Distributed Feedback Laser Diodes*, New York: John Wiley & Sons, 1996.

[53] L. A. Coldren and S. W. Corzine, *Diode Lasers and Photonic Integrated Circuits*, New York: John Wiley & Sons, 1995.

[54] S. L. Chuang, *Physics of Optoelectronic Devices*, New York: John Wiley & Sons, 1995.

[55] L. M. Zhang, S. F. Yu, M. Nowell, D. D. Marcenac, and J. E. Carroll, "Dynamic analysis of radiation and side mode suppression in second order DFB lasers using time-domain large signal traveling wave model," *IEEE J. Quantum Electron.*, vol. 30, no. 6, pp. 1389-1395, 1994.

[56] C. K. Gardiner, P. G. S. Plumb, P. J. Williams and T. J. Reid, "Three-section sampled-grating DBR lasers: modeling and measurements," *IEE Proc.-Optoelectron.*, vol. 143, no. 1, pp. 24-30, 1996.

[57] W. Li, W. –P. Huang, X. Li, and J. Hong, "Multiwavelength gain-coupled DFB laser cascade: design modeling and simulation," *IEEE J. Quantum Electron.*, vol. 36, no. 10, pp. 1110-1116, 2000.

[58] J. Shibayama, M. Muraki, J. Yamauchi and H. Nakano, "Numerial analysis of DFB lasers with uniform longitudinal-intensity distributions using the modified time-domain traveling-wave algorithm," *Microwave Opt. Technol. Lett.*, vol. 44, no. 1, pp. 56-58, 2005.

[59] C. F. Tsang, D. D. Marcenac, . E. Carroll and L. M. Zhang, "Comparison between 'power matrix model (PMM)' and 'time domain model (TDM)' in modeling large signal responses of DFB lasers," *IEE Proc. -J*, vol. 141, no.2, pp. 89-96, 1994.

[60] B. –S. Kim, Y. Chung, "Numerical solution of time-domain coupled-wave equations using split-step algorithm", *Electron. Lett.*, vol. 35, no. 1, pp. 84-85, 1999.

[61] B. -S. Kim, Y. Chung, and J. –S. Lee, "An efficient split-step time-domain dynamic modeling of DFB/DBR laser diodes," *IEEE J. Quantum Electron.*, vol. 36, no. 7, pp. 787-794, 2000.

[62] J. C. Strikwerda, *Finite Difference Schemes and Partial Differential Equations*, Pacific Grove: Wadsworth, 1989.

[63] X. Li, *Optoelectronic Devices: Design, Modeling and Simulation*, Cambridge: Cambridge Uinv. Press, 2009.

[64] A. J. Lowery, "A new dynamic model for multimode chirp in DFB semiconductor laser," *IEE Proc. -J*, vol. 137, pp. 293-300, 1990.

[65] A. J. Lowery, "Comparison between two recent large-signal dynamic DFB laser models," *IEE Proc. -J*, vol. 139, no. 6, pp. 402-406, 1992.

[66] H. Wenzel, U. Bandelow, H. -J. Wünsche, and J. Rehberg, "Mechanisms of fast self pulsations in two-section DFB lasers," *IEEE J. Quantum Electron.*, vol. 32, no. 1, pp.69-78, 1996.

[67] W. -P. Huang, X. Li and T. Makino, "Analytical formulas for modulation responses of semiconductor DFB lasers," *IEEE J. Quantum Electron.*, vol. 31, no. 5, pp.842-851, 1995.

[68] X. Li, A. D. Sadovnikov, W. -P. Huang and T. Makino, "A physics-based three-dimensional model for distributed feedback laser diodes," *IEEE J. Quantum Electron.*, vol. 34, no.9, pp.1545-1553, 1998.

[69] M. Suzuki, S. Miyashita and A. Kuroda "Monte Carlo simulation of quantum spin systems. I," *Prog. Theor. Phys.*, Vol. 58, pp.1377-1387, 1977.

[70] M. Suzuki, "Decomposition formulas of exponential operators and Lie exponentials with some applications to quantum mechanics and statistical physics," *J. Math. Phys.*, vol. 26, no. 4, pp. 601-612, 1985.

[71] Haruo Yoshida, "Construction of higher order symplectic integrators," *Phys. Lett. A*, vol. 150, no. 5, 6, 7, pp. 262-268, 1990.

[72] M. Suzuki, "General theory of fractal path integrals with applications to many-body theories and statistical physics," *J. Math. Phys.*, vol. 32, no. 2, pp. 400-407, 1991.

[73] M. Suzuki, "General nonsymmetric high-order decomposition of exponential operators and symplectic integrators," *J. Phys. Soc. Japan*, vol. 61, pp. 3015-3019, 1992.

[74] A. D. Bandrauk and H. Shen, "Exponential split operator methods for solving coupled time-dependent Schorödinger equations," *J. Chem. Phys.*, vol. 99, no. 2, pp. 1185-1193, 1993.

[75] A. D. Bandrauk and H. Shen, “High-order split-step exponential methods for solving coupled nonlinear Schorödinger equations,” *J. Phys. A: Math. Gen. 27*, pp. 7147-7155, 1994.

[76] J. Lee and B. Fomberg, “A split step approach for the 3-D Maxwell’s equations,” *J. Comput. Appl. Math.*, vol. 158, pp. 485-505, 2003.

[77] P. B. Harboe and J. R. Souza, “Assessment of higher-order exponential operators for the simulation of high-capacity optical communication systems by the split-step Fourier method,” *J. of Microwaves and Optoelelctronics*, vol. 3, no.2, pp.9-22, 2003.

[78] A. D. Bandrauk and H. Shen, “Improved exponential split operator method for solving the time-dependent Schrödinger equation,” *Chem. Phy. Lett.*, vol. 176, no. 5, pp. 428-432, 1991.

[79] T. Prosen and I. Pizorn, “High order non-unitary split-step decomosition of unitary operators,” *J. Phys. A: Math. Gen. 39*, pp. 5957-5964, 2006.

[80] A. Yariv, *Optical Electronics in Modern Communications*, New York, U.S.A.: Oxford University Press, pp. 512, 1997.

[81] J. Chilwell and I. Hodgkinson, “Thin-films field-transfer matrix theory of planar multilayer waveguides and reflection from prism-loaded waveguides,” *J. Opt. Soc. Am. A*, vol. 1, no. 7, pp.742-753, 1984.

[82] M. Yamada and K. Sakuda, “Analysis of almost-periodic distributed feedback slab waveguides via a fundamental matrix approach,” *Appl. Optics*, vol. 26, no. 16, pp. 3474-3478, 1987.

[83] W. Streifer, R. D. Burnham, and D. R. Scifres, “Effect of external reflectors on longitudinal modes of distributed feedback lasers,” *IEEE J. Quantum Electron.*, vol. 11, pp.154-161, 1975.

[84] S. R. Chinn, “Effiects of a mirror reflectivity in a distributed feed-back laser”, *IEEE J. Quantum Electron.*,, vol. 9, no. 6, pp. 574-580, 1973.

[85] A. E. Siegman, “Excess spontaneous emission in non-Hermitian optical systems. II. Laser oscillators,” *Phys. Rev. A*, vol. 39, no.3, pp. 1264-1268, Feb. 1989.

[86] W.A. Hamel and J. P. Woerdman, “Nonorthogonality of the longitudinal eigenmodes of a laser,” *Phys. Rev. A*, vol. 40, no. 5, pp. 2785-2787, Sep. 1989.

[87] P. M. Morse and H. Feshbach, *Methods of Theoretical Physics*, New York: McGraw-Hill, 1953.

[88] COST 240 Group, “Comparison of different DFB laser models within the European COST 240 collaboration,” *IEE Proc. -Optoelectron.* Vol.141, no. 2, pp. 82-88, 1994.

[89] R. Schatz, “Longitudinal spatial instability in symmetric semiconductor lasers due to spatial hole burning,” *IEEE J. Quantum Electron.*, vol. 28, no. 6, pp. 1443-1449, 1992.

[90] Y. Nakano, Y. Luo and K. Tada, “Facet reflection independent single longitudinal mode oscillation in a GaAlAs/GaAs distributed feedback laser equipped with a gain-coupling mechanism,” *Appl. Phys. Lett.*, vol. 55, no. 16, pp. 1606-1608, 1989.

[91] K. David, J. Buus, G. Mothier and R. Baets, "Coupling coefficients in gain-coupled DFB lasers: inherent compromise between coupling strength and loss," *IEEE Photon. Technol. Lett.*, vol. 4, no. 5, pp. 439-441, 1991.

[92] L. M. Zhang, J. E. Carroll and C. Tsang, "Dynamic response of the gain-coupled DFB laser," *IEEE J. Quantum Electron.*, vol. 29, no. 6, pp. 1722-1727, 1993.

[93] L. Olofsson and T. G. Brown, "The influence of resonator structure on the linewidth enhancement factor of semiconductor lasers", *IEEE J. Quantum Electron.*, vol. 28, no. 6, pp. 1450-1458, 1992.

[94] A. J. Lowery and D. Novak, "Enhanced maximum intrinsic modulation bandwidth of complex-coupled DFB semiconductor lasers", *Electron. Lett.*, vol. 29, pp. 461-463, 1993.

[95] K. Kudo, J. I. Shim, K. Komori and S. Arai, "Reduction of effective linewidth enhancement factor α_{eff} of DFB lasers with complex coupling coefficients," *IEEE Photon. Technol. Lett.*, vol. 4, no. 6, pp. 531-534, 1992.

[96] X. Pan, B. Tromborg, H. Olesen and H. E. Lassen, "Efective linewidth enhancement factor and spntaneous emission rate of DFB lasers with gain coupling," *IEEE Photon. Technol. Lett.*, vol. 4, no. 11, pp. 1213-1215, 1992.

[97] A. J. Lowery, "Large-signal effective α factor of complex-coupled DFB semiconductor lasers," *Electron. Lett.*, vol. 28, pp. 2295-2297, 1993.

[98] C. Y. Kuo, M. S. Lin, S. J. Wang, D. A. Ackerman, and L. J. P. Ketelsen, "Static and dynamic characteristics of DFB lasers with longitudinal non-uniformity," *IEEE Photon. Technol. Lett.*, vol. 2, pp. 461-463, 1990.

[99] J. E. A. Whiteaway, G. H. B. Thompson, A. J. Collar, and C. J. Armistead, "The design and assessment of $\lambda/4$ phase-shift DFB laser structure," *IEEE J. Quantum Electron.*, vol. 25, pp. 1761-1779, 1989.

[100] R. S. Tucker and D. J. Pope, "Circuit modeling of the effect of diffusion on damping in a narrow-stripe semiconductor laser," *IEEE J. Quantum Electron.*, vol. 19, no. 7, pp. 1179-1183, 1983.

[101] J. Kinoshita and K. Matsumoto, "Transient chirping in distributed feedback lasers: effect of spatial hole-burning along the laser axis," *IEEE J. Quantum Electron.*, vol. 24, no.11, pp. 2160-2169, 1988.

[102] J. Kinoshita, "Modeling of high-speed DFB lasers considering the spatial holeburning effect using three rate equations," *IEEE J. Quantum Electron.*, vol. 30, no. 4, pp. 929-938, 1994.

[103] M. Lax, "Classical noise IV: Langevin methods," *Rev. Mod. Phys.*, vol.38, no. 3, pp. 541-566, 1966.

[104] C. H. Henry, "Theory of spontaneous emission noise in open resonators and its application to lasers and optical amplifiers," *IEEE J. Lightwave Tech.*, vol. 4, no. 3, pp. 288-297, 1986.

[105] J. Morikuni, P. Mena, A. Harton, and K. Wyatt, "The mixed-technology modeling and simulation of opto-electronic microsystems," *J. Model. Simul. Microsyst.*, vol. 1, no. 1, pp. 9-18, 1999.

[106] M. De Wilde, O. Rits, R. Bockstaele, J. V. Campenhout, and R. Baets, "A circuit-level simulation approach to analyse system level behaviour of VCSEL-based

optical interconnects," in *Photonics Fabrication Europe*, vol. 4942, Brugge, Belgium: SPIE, Oct. 2002.

[107] S. B. Huq, "Ease system simulation with IBIS device models," *Electron. Des.*, vol. 44, no. 26, pp. 6, Dec. 1996.

[108] J. P. Laude, *Wavelength Division Multiplexing*, New York: Prentice Hall, 1993.

[109] J. Buus, "Mode selectivity in DFB lasers with cleaved facets," *Electron. Lett.*, vol. 21, pp. 179-180, 1985.

[110] K. David, G. Morthier, P. Vankwikelberge, and R. Baets, "Yield analysis of non-AR-coated DFB lasers with combined index and gain coupling," *Electron. Lett.*, vol. 26, pp. 238-239, 1990.

[111] J. Zoz and B. Borchert, "Dynamic behavior of complex-coupled DFB lasers with in-phase absorptive grating," *Electron. Lett.*, vol. 30, pp. 39-40, 1994.

[112] S. M. Sadeghi and W. Li, "Electromagnetically induced distributed feedback intersubband lasers," *IEEE J. Quantum Electron.*, vol. 41, pp. 1227-1234, 2005.

[113] S. M. Sadeghi, W. Li, X. Li and W.-P. Huang, "Tunable infrared semiconductor lasers based on electromagnetically induced optical defects," *IEEE Sel. Topic Quantum Electron.*, vol. 13, pp. 1046-1053, 2007.

[114] T. L. Koch and U. Koren, "Semiconductor lasers for coherent optical fiber communications," *IEEE J. Lightwave Technol.*, vol. 8, pp. 274-292, 1990.

Appendix A

Consistency and Stability of the FTBS FD Scheme

A. Consistency of the FTBS FD Scheme:

Define the operator P as $\frac{1}{\upsilon_g}\frac{\partial}{\partial t} \pm \frac{\partial}{\partial z}$ so that

$$\mathrm{P}\begin{bmatrix} F \\ R \end{bmatrix} = \begin{bmatrix} \frac{1}{\upsilon_g}\frac{\partial F}{\partial t} + \frac{\partial F}{\partial z} \\ \frac{1}{\upsilon_g}\frac{\partial R}{\partial t} - \frac{\partial R}{\partial z} \end{bmatrix}. \tag{A.1}$$

For the FTBS scheme (2.24), the difference operator is given by

$$\mathrm{P}_d\begin{bmatrix} F \\ R \end{bmatrix} = \begin{bmatrix} \frac{F_{n+1}^{k+1} - F_{n+1}^{k}}{v_g \Delta t} + \frac{F_{n+1}^{k} - F_{n}^{k}}{\Delta z} \\ \frac{R_{n-1}^{k+1} - R_{n-1}^{k}}{v_g \Delta t} - \frac{R_{n}^{k} - R_{n-1}^{k}}{\Delta z} \end{bmatrix}. \tag{A.2}$$

From the Taylor expansions evaluated at $(n\Delta z, k\Delta t)$ that

$$F_{n+1}^{k+1} = F_n^k + \frac{\partial F}{\partial t}\Delta t + \frac{\partial F}{\partial z}\Delta z + \frac{1}{2}\frac{\partial^2 F}{\partial t^2}\Delta t^2 + \frac{1}{2}\frac{\partial^2 F}{\partial z^2}\Delta z^2 + O(\Delta t^3) + O(\Delta z^3)$$

$$F_{n+1}^{k} = F_n^k + \frac{\partial F}{\partial z}\Delta z + \frac{1}{2}\frac{\partial^2 F}{\partial z^2}\Delta z^2 + O(\Delta z^3)$$

$$R_{n-1}^{k+1} = R_n^k + \frac{\partial R}{\partial t}\Delta t - \frac{\partial R}{\partial z}\Delta z + \frac{1}{2}\frac{\partial^2 R}{\partial t^2}\Delta t^2 + \frac{1}{2}\frac{\partial^2 R}{\partial z^2}\Delta z^2 + O(\Delta t^3) + O(\Delta z^3)$$

$$R_{n-1}^{k} = R_n^k - \frac{\partial R}{\partial z}\Delta z + \frac{1}{2}\frac{\partial^2 R}{\partial z^2}\Delta z^2 + O(\Delta z^3)$$

We may obtain

$$\mathrm{P}_d\begin{bmatrix}F\\R\end{bmatrix}=\begin{bmatrix}\dfrac{1}{v_g}\dfrac{\partial F}{\partial t}+\dfrac{\partial F}{\partial z}+\dfrac{1}{2v_g}\dfrac{\partial^2 F}{\partial t^2}\Delta t+\dfrac{1}{2}\dfrac{\partial^2 F}{\partial z^2}\Delta z+O(\Delta t^2)+O(\Delta z^2)\\ \dfrac{1}{v_g}\dfrac{\partial R}{\partial t}-\dfrac{\partial R}{\partial z}+\dfrac{1}{2v_g}\dfrac{\partial^2 R}{\partial t^2}\Delta t+\dfrac{1}{2}\dfrac{\partial^2 R}{\partial z^2}\Delta z+O(\Delta t^2)+O(\Delta z^2)\end{bmatrix}. \tag{A.3}$$

Thus

$$\left(\mathrm{P}-\mathrm{P}_d\right)\begin{bmatrix}F\\R\end{bmatrix}=\begin{bmatrix}\dfrac{1}{2v_g}\dfrac{\partial^2 F}{\partial t^2}\Delta t+\dfrac{1}{2}\dfrac{\partial^2 F}{\partial z^2}\Delta z+O(\Delta t^2)+O(\Delta z^2)\\ \dfrac{1}{2v_g}\dfrac{\partial^2 R}{\partial t^2}\Delta t+\dfrac{1}{2}\dfrac{\partial^2 R}{\partial z^2}\Delta z+O(\Delta t^2)+O(\Delta z^2)\end{bmatrix}\to 0 \quad \text{as} \quad \left(\Delta z\,,\Delta t\right)\to 0$$

Therefore, this scheme is consistent [62].

B. Stability Study of the FTBS FD Scheme by Von Neumann Analysis:

It was also proved in [62] that the homogeneous version of Eq. (2.21) is stable if $\mathrm{P}\psi=0$ is stable under a consistent one-step scheme. By taking the complex field of the forward propagation wave as an example, we may obtain from $\mathrm{P}_d F=0$ that

$$F_{n+1}^{k+1}=\left(1-\eta_r\right)F_{n+1}^{k}+\eta_r F_n^k. \tag{A.4}$$

We may define the Fourier transform to the grid function F_n as

$$\hat{F}(\zeta)=\frac{1}{2\pi}\sum_{n=-\infty}^{\infty}e^{-jn\Delta z\zeta}F_n\Delta z \qquad \text{for } \zeta\in\left[-\pi/\Delta z,\pi/\Delta z\right] \tag{A.5}$$

As a result, the Fourier inversion transform may read

$$F_n^k=\frac{1}{\sqrt{2\pi}}\int_{-\pi/\Delta z}^{\pi/\Delta z}e^{jn\Delta z\zeta}\hat{F}^k\left(\zeta\right)d\zeta\ . \tag{A.6}$$

Substituting Eq. (A.6) into Eq. (A.4) for F_{n+1}^{k} and F_{n}^{k}, we have

$$F_{n+1}^{k+1}=\frac{1}{\sqrt{2\pi}}\int_{-\pi/\Delta z}^{\pi/\Delta z}e^{j(n+1)\Delta z\zeta}\left[1-\eta_r+\eta_r e^{-j\Delta z\zeta}\right]\hat{F}^{k}(\zeta)d\zeta. \tag{A.7}$$

On the other hand, we may also obtain from Eq. (A.6)

$$F_{n+1}^{k+1}=\frac{1}{\sqrt{2\pi}}\int_{-\pi/\Delta z}^{\pi/\Delta z}e^{j(n+1)\Delta z\zeta}\hat{F}^{k+1}(\zeta)d\zeta. \tag{A.8}$$

Comparing Eq. (A.7) with Eq. (A.8), it is deduced that

$$\hat{F}^{n}(\zeta)=(\rho)^{n}\hat{F}^{0}(\zeta) \tag{A.9}$$

with

$$\rho=1-\eta_r+\eta_r e^{-j\Delta z\zeta} \tag{A.10}$$

It is found that the FD scheme is stable if $|\rho|\leq 1$ [62] which is valid if $\eta_r\leq 1$. The same condition can be found for the complex field of the backward propagation by using the similar procedure.

We may conclude that the criterion of the stability of the FTBS scheme is $\eta_r\leq 1$.

Appendix B

Analytical Solutions of Integrals in Photon Wave Equations with Carrier Shape Approximation

By using Eq. (6.2), the analytical expressions of the integral in Eq. (6.16) and Eq. (6.17) for the uniform-grating DFB laser are derived as follows

$$\begin{aligned}\int_0^L \Theta_s^p \mathbf{w}_m \bar{\boldsymbol{\Phi}}_n^0 \, dz = c_{lmn} \Big\{ & 2\big\{(X_1X_2 + Y_1Y_2)\sinh(\gamma_A L) + (X_1Y_2 + X_2Y_1)\left[\cosh(\gamma_A L) - 1\right]\big\}/\gamma_A \\ & + 2\big\{(X_1X_2 - Y_1Y_2)\sinh(\gamma_B L) + (X_1Y_2 - X_2Y_1)\left[\cosh(\gamma_B L) - 1\right]\big\}/\gamma_B \\ & + 2\big\{(X_2X_3 + Y_2Y_3)\sinh(\gamma_C L) + (X_2Y_3 + X_3Y_2)\left[\cosh(\gamma_C L) - 1\right]\big\}/\gamma_C \\ & + 2\big\{(X_2X_3 - Y_2Y_3)\sinh(\gamma_D L) - (X_2Y_3 - X_3Y_2)\left[\cosh(\gamma_D L) - 1\right]\big\}/\gamma_D \\ & + 2\big\{(X_1X_4 + Y_1Y_4)\sinh(\gamma_E L) - (X_1Y_4 + X_4Y_1)\left[\cosh(\gamma_E L) - 1\right]\big\}/\gamma_E \\ & + 2\big\{(X_1X_4 - Y_1Y_4)\sinh(\gamma_F L) - (X_1Y_4 - X_4Y_1)\left[\cosh(\gamma_F L) - 1\right]\big\}/\gamma_F \\ & + 2\big\{(X_3X_4 + Y_3Y_4)\sinh(\gamma_G L) - (X_3Y_4 + X_4Y_3)\left[\cosh(\gamma_G L) - 1\right]\big\}/\gamma_G \\ & + 2\big\{(X_3X_4 - Y_3Y_4)\sinh(\gamma_H L) - (X_3Y_4 - X_4Y_3)\left[\cosh(\gamma_H L) - 1\right]\big\}/\gamma_H \Big\}\end{aligned} \tag{B.1}$$

where

$$c_{lmn} = |c_l|^2 c'_m c_n,$$

$$X_1 = 2r_1 + \frac{2r_1\left(\kappa^2 - \xi_m^0\xi_n^0/\upsilon_g^2\right) + j\kappa\left(\xi_m^0 + \xi_n^0\right)\left(r_1^2 + 1\right)/\upsilon_g}{\gamma_m\gamma_n},$$

$$X_2 = \frac{\left(r_1^2 + 1\right)\left(|\gamma_l|^2 + \left|\xi_l^0/\upsilon_g\right|^2 + \kappa^2\right) + 4r_1\kappa\,\mathrm{Im}(\xi_l^0)/\upsilon_g}{|\gamma_l|^2},$$

$$X_3 = 4r_1 - X_1 = 2r_1 - \frac{2r_1\left(\kappa^2 - \xi_m^0\xi_n^0/\upsilon_g^2\right) + j\kappa\left(\xi_m^0 + \xi_n^0\right)\left(r_1^2 + 1\right)/\upsilon_g}{\gamma_m\gamma_n}, \quad X_4 = 2\left(r_1^2 + 1\right) - X_2$$

$$Y_1 = j\kappa\left(1-r_1^2\right)\frac{\gamma_m+\gamma_n}{\gamma_m\gamma_n},\ Y_2 = 2\left(1-r_1^2\right)\frac{\mathrm{Re}(\gamma_l)\,\mathrm{Re}(\xi_l^0)+\mathrm{Im}(\gamma_l)\,\mathrm{Im}(\xi_l^0)}{\upsilon_g\left|\gamma_l\right|^2},$$

$$Y_3 = j\kappa\left(1-r_1^2\right)\frac{\gamma_n-\gamma_m}{\gamma_m\gamma_n},\ Y_4 = j2\left(1-r_1^2\right)\frac{\mathrm{Im}(\gamma_l)\,\mathrm{Re}(\xi_l^0)-\mathrm{Re}(\gamma_l)\,\mathrm{Im}(\xi_l^0)}{\upsilon_g\left|\gamma_l\right|^2},$$

$\gamma_A=\gamma_m+\gamma_n+2\,\mathrm{Re}(\gamma_l)$, $\gamma_B=-\gamma_m-\gamma_n+2\,\mathrm{Re}(\gamma_l)$, $\gamma_C=\gamma_m-\gamma_n+2\,\mathrm{Re}(\gamma_l)$, $\gamma_D=-\gamma_m+\gamma_n+2\,\mathrm{Re}(\gamma_l)$,

$\gamma_E=-\gamma_m-\gamma_n+2j\,\mathrm{Im}(\gamma_l)$, $\gamma_F=\gamma_m+\gamma_n+2j\,\mathrm{Im}(\gamma_l)$, $\gamma_G=-\gamma_m+\gamma_n+2j\,\mathrm{Im}(\gamma_l)$, $\gamma_H=\gamma_m-\gamma_n+2j\,\mathrm{Im}(\gamma_l)$.

Equation (B1) is valid for $\gamma_X \neq 0, X=A,\cdots,H$, otherwise the corresponding integral is replaced by the coefficient in front of the term "$\sinh\left(\gamma_X L\right)$".

Appendix C

List of Publications Related to the Thesis Work

C.1 International Journals

P.1. **Y. Xi**, W. -P. Huang and X. Li, "Standing Wave Model Based on Threshold Hot Cavity Modes for Simulation of Gain-Coupled DFB Lasers," submitted to *IEEE/OSA J. of Lightwave Tech.*

P.2. **Y. Xi**, W. -P. Huang and X. Li, "An Efficient Solution to the Standing-Wave Model based on cold cavity modes for simulation of DFB lasers," *IEEE/OSA J. of Lightwave Tech.*, In press.

P.3. **Y. Xi**, X. Li and W. -P. Huang, "Time-Domain Standing-Wave Approach Based on Cold Cavity Modes for Simulation of DFB Lasers," *J. of IEEE Quantum Electronics,* vol. 44, no. 10, pp. 931-937, 2008.

P.4. **Y. Xi**, X. Li, S. Sadeghi, W. -P. Huang, "Dispersive-Grating Distributed Feedback Lasers," *Optics Express,* vol. 16, no.14, July 2008, pp. 16809-16814.

P.5. **Y. Xi**, W. -P. Huang and X. Li, "High-Order Split-Step Schemes for Time-Dependent Coupled-Wave Equations", *J. of IEEE Quantum Electronics*, vol. 43,no. 5, May 2007, pp. 419-425.

C.2 International Conference Papers

P.6. **Y. Xi**, X. Li and W. -P. Huang, "An Efficient Standing-Wave Model for Simulation of $\lambda/4$ – Shifted DFB Lasers," Asia Optical Fiber Communication & Optoelectronic Exposition & Conference, 2008.

P.7. X. Li, **Y. Xi** and W. -P. Huang, "Threshold Analysis of a Novel Dispersive Grating Distributed Feedback Laser Diode," Asia Optical Fiber Communication & Optoelectronic Exposition & Conference, 2007. **(Invited paper)**

P.8. **Y. Xi**, X. Li and W. -P. Huang, "Standing-Wave Model Based on Modes of Cold Cavity for Simulation of Laser Diodes", in *Integrated Photonics and Nanophotonics Research and Applications 2007 Technical Digest* (The Optical Society of America, Washington, DC, 2007)